SANDIA REPORT
SAND2006-6225
Unlimited Release
Printed November 2006

On-Line Coating of Glass with Tin Oxide by Atmospheric Pressure Chemical Vapor Deposition

Mark Allendorf, W.G. Houf, A.H. McDaniel, and Y. Chae

M. Li, J.F. Sopko and J.W. McCamy*

Prepared by
Sandia National Laboratories
Albuquerque, New Mexico 87185 and Livermore, California 94550

Sandia is a multiprogram laboratory operated by Sandia Corporation,
a Lockheed Martin Company, for the United States Department of Energy's
National Nuclear Security Administration under Contract DE-AC04-94AL85000.

Sandia National Laboratories

* Glass Technology Center, PPG Industries, P.O. Box 11472, Pittsburg, PA 15238

Issued by Sandia National Laboratories, operated for the United States Department of Energy by Sandia Corporation.

Available to DOE and DOE contractors from
U.S. Department of Energy
Office of Scientific and Technical Information
P.O. Box 62
Oak Ridge, TN 37831

Telephone: (865) 576-8401
Facsimile: (865) 576-5728
E-Mail: reports@adonis.osti.gov
Online ordering: http://www.doe.gov/bridge

Available to the public from
U.S. Department of Commerce
National Technical Information Service
5285 Port Royal Rd
Springfield, VA 22161

Telephone: (800) 553-6847
Facsimile: (703) 605-6900
E-Mail: orders@ntis.fedworld.gov
Online order: http://www.ntis.gov/help/ordermethods.asp?loc=7-4-0#online

SAND2006-6225
Unlimited Release
Printed November 2006

On-Line Coating of Glass with Tin Oxide by Atmospheric Pressure Chemical Vapor Deposition

Mark Allendorf, W.G., Houf, A. H. McDaniel, and Y. Chae
Sandia National Laboratories
P.O. Box 969
Livermore, CA 94551

M. Li, J.F. Sopko and J.W. McCamy
Glass Technology Center - PPF Industries
P. O. Box 11472
Pittsburgh, PA 15238

Abstract

Atmospheric pressure chemical vapor deposition (APCVD) of tin oxide is a very important manufacturing technique used in the production of low-emissivity glass. It is also the primary method used to provide wear-resistant coatings on glass containers. The complexity of these systems, which involve chemical reactions in both the gas phase and on the deposition surface, as well as complex fluid dynamics, makes process optimization and design of new coating reactors a very difficult task.

In 2001 the U.S. Dept. of Energy Industrial Technologies Program Glass Industry of the Future Team funded a project to address the need for more accurate data concerning the tin oxide APCVD process. This report presents a case study of on-line APCVD using organometallic precursors, which are the primary reactants used in industrial coating processes. Research staff at Sandia National Laboratories in Livermore, CA, and the PPG Industries Glass Technology Center in Pittsburgh, PA collaborated to produce this work.

In this report, we describe a detailed investigation of the factors controlling the growth of tin oxide films. The report begins with a discussion of the basic elements of the deposition chemistry, including gas-phase thermochemistry of tin species and mechanisms of chemical reactions involved in the decomposition of tin precursors. These results provide the basis for experimental investigations in which tin oxide growth rates were measured as a function of all major process variables. The experiments focused on growth from monobutyltintrichloride (MBTC) since this is one of the two primary precursors used industrially. There are almost no reliable growth-rate data available for this precursor. Robust models describing the growth rate as a function of these variables are derived from modeling of these data. Finally, the results are used to conduct computational fluid dynamic simulations of both pilot- and full-scale coating reactors. As a result, general conclusions are reached concerning the factors affecting the growth rate in on-line APCVD reactors. In addition, a substantial body of data was generated that can be used to model many different industrial tin oxide coating processes. These data include the most extensive compilation of thermochemistry for gas-phase tin-containing species as well as kinetic expressions describing tin oxide growth rates over a wide range of temperatures, pressures, and reactant concentrations.

Acknowledgements

The authors express their gratitude to their colleagues Ida Nielsen and Carl Melius for their assistance in with thermochemistry aspects of this report; Dr. Greg Evans (Sandia) and Prof. William Greif (University of California, Berkeley) for technical discussions concerning mass transport in the SFR; and Dr. A. M. B. van Mol (TNO, Eindhoven, The Netherlands) for his contributions to the measurement of the kinetics of MBTC decomposition and tin oxide deposition. Technical discussions with Mehran Arbab, Robert Greiner, Guosheng Kang, Thomas Sailock, William Siskos, John Sopko, Jill Troup, and Kwang Won at PPG Glass Technology Center are also gratefully acknowledged. The authors thank Dr. David Russo of Atofina for providing MBTC and Prof. David Goodwin at the California Institute of Technology for generously sharing his design of the stagnation-flow reactor (SFR). The results presented in this report were funded in part by the U.S. Dept. of Energy Office of Industrial Technologies Glass Industry of the Future Team, in collaboration with PPG Industries, Inc. (Pittsburgh, PA).

Contents

Figures

Tables

Chapter 1 Introduction

On-line CVD coating over large area substrates is routinely performed on float-glass production lines using both inorganic and organometallic tin precursors[1-6]. For on-line CVD coating, the process is difficult to optimize and control because of high line speeds that limit growth times to 1–3 s, leading to a requirement for fast growth rates and high volumetric gas flows[6]. This limitation produces a thin thermal boundary layer over the substrate, and consequently, low reactant conversion efficiencies (as low as 10%). Stringent requirements for optical uniformity demand uniform growth rates across very large substrates (as much as 4 m wide). Although the deposition temperature and the reactant concentration have significant effects on the growth rate, the need to minimize haze and to control coating color limits the ability to use these variables to enhance coating efficiency[4]. Because of the difficulty and cost of making changes in a full-scale manufacturing process, there is a clear need for kinetic models that account for the effects of process variables on deposition rate and reactant conversion efficiency to guide optimization efforts.

One of the most important industrial CVD precursors is monobutyltintrichloride (MBTC). Development of a process model for SnO_2 deposition from MBTC requires extensive knowledge of chemical reaction rates, including the kinetics of MBTC thermal decomposition, oxidation, and hydrolysis, as well as SnO_2 growth rates. However, only a few studies of SnO_2 deposition using MBTC have been reported.[4, 7] Lee et al. published the effect of H_2O on deposition behavior and electrical properties using a horizontal tube reactor operated at atmospheric pressure[7], finding that deposition rates increase with the addition of H_2O. They concluded that this effect is due to hydrolytic decomposition of the Sn–Cl bond during CVD. However, they did not publish a detailed deposition mechanism. In addition, the reactor used in their experiments makes mechanism development difficult, since its geometry is at least two-dimensional. Computations with detailed mechanisms become very time-consuming in such situations and can quickly become impractical when complex chemistry is involved. Thus, experimental data are needed to probe these various mechanisms, preferably obtained in a reactor whose fluid dynamics and heat transfer are relatively simple to model.

The potential for multiple reaction pathways to contribute to SnO_2 growth complicates understanding of this system. Chapter 3 describes a thermodynamic analysis of potential reaction pathways for the gas-phase pyrolysis, oxidation, and hydrolysis of MBTC, using thermochemistry predicted by ab initio calculations (Chapter 2)[8, 9]. The results suggest that gas-phase chemistry could be important under atmospheric-pressure CVD conditions and that tin-containing species other than MBTC may contribute to film growth[8]. In particular, the calculations suggest that tin hydroxides are thermodynamically stable and that formation of complexes between H_2O and either MBTC [9] or its decomposition products[8] is exothermic; none of these pathways have been previously considered. This analysis is supported by experiments in a continuously stirred-tank reactor, which indicate that MBTC is completely decomposed within 2 s at 873 K and 1 atm[10]. An important role for gas-phase reactions in this system would also be consistent with investigations of the SnO_2 precursors $Sn(CH_3)_4$ and $SnCl_2(CH_3)_2$ by Gordon et al.[11, 12]

Deposition of thin films from metalorganic precursors using chemical vapor deposition techniques (MOCVD) represents a very important class of industrial materials synthesis processes. In particular, the glass industry uses atmospheric pressure chemical vapor deposition (APCVD) processes to produce thin films on float glass. Tin oxide-coated glass products have a wide range of applications due to a number of useful properties, including high transparency, low electrical resistivity, high reflectivity for infrared light, high mechanical hardness, tight adhesion to the substrate, and good environmental stability. Some common SnO_2 applications include the following:

- Low-E coating on glass windows[1-8]
- Solar cells[9-15]
- Gas sensors[16-19]
- Heating elements in aircraft windows[20, 21]
- Antistatic coatings on instrument panels[22, 23]
- Transparent electrodes in electroluminescent lamps and displays[24-26]
- Protective and wear-resistant coatings on glass containers[27]

The highest-volume product is glass coated with tin oxide (SnO_2), with North American production estimated at 110 million ft^2/year. In addition, literally billions of glass containers are coated annually with SnO_2 to improve wear resistance and strength. Recently, "self-cleaning" glass coated with TiO_2 has been marketed by several companies.

The basic steps that can occur during a chemical vapor deposition (CVD) process are illustrated in Figure 1-1[28]:

1. Mass transport of the gaseous reactants from the reactor inlet to the deposition zone
2. Chemical reactions in the gas phase leading to new reactive species and byproducts
3. Mass transport of the initial reactants and reaction products to the substrate surface
4. Adsorption of these species onto the substrate surface
5. Surface diffusion of adsorbed species over the surface to the growth center
6. Surface reactions at the growth center
7. Desorption of byproducts
8. Diffusive mass transport of the byproducts away from the surface
9. Mass transport of the byproducts to the outlet of the reactor

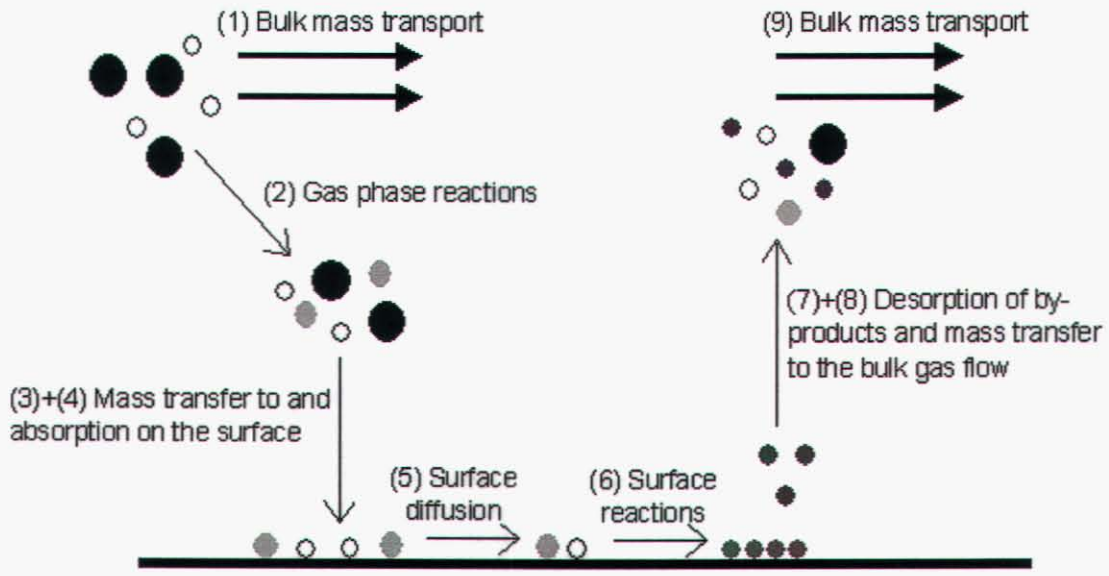

Figure 1-1. Schematic representation of the basic steps in a CVD process (adapted from reference [28]).

As is clear from the figure, CVD is a complex process, potentially involving both gas-phase and surface chemistry, as well as the hydrodynamics of the reactor system. The design of CVD processes in industry is therefore rarely based on a scientific approach, but rather on empirical results and experience. Optimal conditions do not always result. For example, low process yields and high product rejection rates (usually due to optical nonuniformities) are common. The lack of a more fundamental understanding of the coating process was identified as one of the major problems in the glass industry at a recent roadmapping exercise for the development of coatings [29].

The need for substantial improvements in industrial glass coating processes is illustrated by two examples:

- In the deposition of coatings, such as tin oxide on flat glass, a best-case yield of around 70% is achieved using CVD, but this can be as low as 50%. If a coating is not applied, the yield is typically 75–80%. This means that coating methods substantially reduce the overall productivity of the glass manufacturing process, resulting in large amounts of rejected glass that must be ground and remelted. Such high reject rates represent an enormous cost in energy. On average, roughly 4×10^{10} kJ/year must be expended to remelt this glass.

- The efficiency of reactant utilization in CVD on float glass can be as low as 10%, necessitating the installation of expensive chemical scrubbing units or incinerators and producing more than one million kg/year of landfill waste.

Because of the high cost of experimentally determining the effects of process variables on deposition rates, detailed process models are seen as the only economical method of making significant improvements in existing industrial deposition methods. Fundamental knowledge concerning the reaction chemistry is necessary to develop models that can effectively predict deposition rates across a broad range of potential process variables.

In 2001, the U.S. Department of Energy's Office of Industrial Technologies Glass Industry of the Future Team initiated an effort to address the need for more accurate data concerning the SnO_2 APCVD process and improved simulation tools to predict the outcome of these coating processes. A project entitled "Development of Process Optimization Strategies, Models, and Chemical Databases for On-Line Coating of Float Glass," involving a collaboration between Sandia National Laboratories (Livermore, CA) and PPG Industries (Pittsburgh, PA) was funded by the U.S. Department of Energy Industrial Technologies Program to address the need to improve the efficiency of on-line APCVD processes used primarily to deposit coatings on float glass, but also on glass containers. APCVD processes in the flat-glass industry currently have rather low efficiencies; as mentioned above, as little as 10% of the incoming precursor chemicals are converted to coating in some cases, resulting in annual production and waste-treatment disposal costs to the industry of nearly $23 million. In addition, remelting of glass due to defects in the coatings results in over 1.1×10^{11} Btu/year of unproductive energy usage.

The objectives of the project were as follows:

1. Identify modifications to existing APCVD coater designs and/or new coater designs that will double the efficiency of reactant utilization, thereby substantially reducing waste emissions and purchases of raw materials.
2. Develop validated computational models to predict defects due to thickness nonuniformity and haze; use these to reduce defect frequency and improve the overall energy efficiency of the process by reducing the amount of rejected glass that must be remelted.
3. Generate a database of fundamental thermodynamic and kinetic information for APCVD.
4. Provide enhanced understanding of the underlying chemical reactions that control APCVD, which will enable the development of improved process models and control strategies for float-glass coating and other types of glass, such as containers, that use APCVD coatings.

Prior to the start of the project, research at PPG resulted in methods to control haze, aspects of which were published [30]. Consequently, the project focused its efforts primarily on three goals, leading to validated process models that can be used to reduce or eliminate the defects caused by thickness nonuniformities.

To reach these goals, a comprehensive approach was adopted that included the following elements:

1. Employ computational methods to predict thermochemistry and kinetics for gas-phase precursor chemistry (Chapters 2 and 3).
2. Perform measurements and modeling of SnO_2 growth rates under highly controlled experimental conditions to generate data for model development and validation (Chapters 4 and 5).
3. Conduct computational fluid dynamics simulations to predict growth rates under realistic processing conditions (Chapter 6).

To make the outcomes of this work readily available, the following steps were taken:

1. Thermodynamic data relevant to the process were made available at no charge to the user at the web address: www.ca.sandia.gov/HiTempThermo.
2. Fifteen articles were published in trade publications, newsletters, proceedings of glass-related conferences, and peer-reviewed scientific journals.
3. Twenty presentations were given to audiences in a variety of technical and industry-related venues.

This document is a case study of the APCVD SnO_2 process and is intended to provide a summary and access to data, models, and conclusions reached during this project. It also provides an illustration of a successful approach to the optimization of industrial CVD coating processes in general; thus, this report should be of value to the wider glass community as a resource for understanding these processes.

1.1 References

1. R. N. Ghoshtagore, *J. Electrochem. Soc.*, 125, 110 (1978).
2. C. J. Giunta, D. A. Strickler, and R. G. Gordon, *J. Phys. Chem.*, 97, 2275 (1993).
3. Y. P. Yadava, G. Denicolo, A. C. Arias, L. S. Roman, and I. A. Hummelgen, *Mat. Chem. Phys.*, 48, 263 (1997).
4. J. L. Buchanan and C. McKown, *J. Non-Cryst. Sol.*, 218, 179 (1997).
5. R. Gordon, *J. Non-Cryst. Sol.*, 281, 81 (1997).
6. R. J. McCurdy, *Thin Sol. Films,* 351, 66 (1999).
7. S.-M. Lee, D.-L. Kim, H.-J. Youn, and K. S. Hong, *Jpn. J. Appl. Phys.*, 39, 407 (2000).
8. M. D. Allendorf, I. M. B. Nielsen, C. F. Melius, and A. M. B.Van Mol, in *6th Int. Symp. Chem. Vapor Dep./EUROCVD-14,* M. D. Allendorf, F. Maury, and F. Teyssandier, Editors, PV 2003-8, p. 55, *The Electrochemical Society Proceedings Series*, Pennington, NJ (2003).
9. M. D. Allendorf, A. M. B. van Mol, "Gas-Phase Thermochemistry and Mechanism of Organometallic Tin Oxide Precursors," invited book chapter, *Topics in Organometallic Chem.*, Springer (Berlin) vol. 9, p. 1, 2005.
10. C. G. Borman and R. G. Gordon, *J. Electrochem. Soc.*, 136, 3820 (1989).
11. A. G. Zawadzki, C. J. Giuna, R. G. Gordon, *J. Phys. Chem.*, 96, 5364 (1992).
12. G. H. Lindner (1988), U.S. Patent 4737388
13. P. F. Gerhardinger, McCurdy RJ (1996) *Mat. Res. Soc. Symp. Proc.,* vol 426 p 399
14. G. A. Neumann, R. L. Stewart-Davis (1996), U.S. Patent 5395698
15. M. J. Soubeyrand, A. C. Halliwell (1997), U. S. Patent 5698262
16. P. R. Athey, D. S. Dauson, D. E. Lecocq, G. A. Neuman, J. F. Sopko, R. L. Stewart-Davie (1997), U. S. Patent 5464657
17. R. D. Goodman, W. M. Greenberg, P. J. Tausch (1989), U. S. Patent 4847157
18. V. A. Henry (1989), U. S. Patent 4853257
19. D. J. Middleton, J. I. Grenier (1985), U. S. Patent 4548836

20. R. G. Gordon, J. Proscia, F. B. Ellis Jr., A. E. Delahoy (1989) *Sol. Energy Mater.* 18: 263

21. R. Plattner, W. Stetter, P. Kohler (1988) Simens Forsch.- u. Entwick. -Ber. 17(3): 138

22. B.T. Boiko, G. I. Kopach, N. P. Klochko, V. R. Kopach, G. S. Khripunov, A. I. Chernikov (1990) *Appl. Solar Energy.* 26: 40

23. A. Greenwald, J. Bragagnolo, M. Leonard (1987) *19th IEEE Photovoltaic Spec. Conf.* p 621

24. A. K. Saxena, S. P. Singh, O. P. Agnihotri (1986) *Sol. Cells.* 19: 163

25. K . Sato, Y. Gotoh, Y. Hayashi, K. Adachi, H. Nishimura (1990) *Reports Res. Lab. Asahi Glass Co., Ltd.* 40(2): 233

26. K. Singh, R. Y. Tamakloe (1996) *Sol. Energy.* 56: 343

27. F. Berger, E. Beche, R. Berjoan, D. Klein, A. Chambaudet (1996) *Appl. Surf. Sci.* 93: 9

28. J. R. Brown, M. T. Cheney, P. W. Haycock, D. J. Houlton, A. C. Jones, E.W. Williams (1997) J. *Electrochem. Soc.* 144: 295

29. F. Dimeo Jr., S. Semancik, R. E. Cavicchi, J. S. Suehle, P. Chaparala, N. H. Tea (1996) *Mater. Res. Soc. Symp. Proc.* 415: 231

30. K. H. Kim, C. G. Park (1991) *J. Electrochem. Soc.* 138: 2408

31. T. J. Clough, V. L. Grosvenor, N. Pinsky (1994), U. S. Patent 5317132

32. A. Mukherjee (1990), U. S. Patent 4959257

33. H. Tong, C. Hu, M. Hsu (1997), U. S. Patent 5652477

34. J. W. Cahill (1994), U. S. Patent 5284705

35. K. H. Houng (1982) *Bull. Inst. Chem. Acad. Sin.* 29: 19

36. R. Gazdag, E. Seyfried, Z. Ligeti (1981) Liq. Cryst. Res. Appl., Proc. 3rd Liq. Cryst. Conf. Soc. Countries. 2: 1137

37. J. Kane, M. Ling (1988), U. S. Patent 4728581

38. M. Nakagawa, T. Amano, S. Yokokura (1997) *J. Non-Cryst. Sol.* 218: 100

39. M. L. Hitchman, K. F. Jensen (eds) (1993) *Chemical Vapor Deposition. Academic*, London

40. M. D. Allendorf (2001) *Thin Sol. Films.* 392: 155

41. J. Szanyi, *Applied Surface Science*, Vol 185, p. 161 (2002)

Chapter 2 Gas-Phase Thermochemistry*

2.1 Quantum Chemistry Methods for the Prediction of Molecular Thermochemistry

Accurate thermochemical data is needed to model gas-phase reactions occurring during tin oxide APCVD. For the purposes of this work, "accurate" generally means knowing heats of formation to ±2–3 kcal/mol. It is evident that much of the speculation in the literature concerning tin oxide mechanisms could be put on a firmer footing if such data were available for all of the species of interest.

From a computational point of view, the heat of formation, which is derived from the electronic energy of the molecule $E_{molecule}$, is the most difficult thermochemical quantity to predict accurately. Entropies and heat capacities are derived from vibration and rotational constants, all of which can be predicted with considerable accuracy using relatively low levels of theory. Thus, the development of ab initio methods appropriate for a new class of compounds focuses primarily on identifying a level of theory and the basis set(s) needed to achieve sufficient accuracy in the electronic energy [1, 2].

Once the electronic energy has been calculated, the molecular heat of formation $\Delta H°_f$ is calculated as follows:

$$\Delta H°_{atomization}(0\ K) = \Sigma E_{atom} - E_{molecule} + E(\text{zero-point}) \quad (2\text{-}1)$$

$$\Delta H°_f(0\ K) = \Sigma \Delta H°_{f,\,atom}(0\ K) - \Delta H°_{atomization}(0\ K) \quad (2\text{-}2)$$

where E represents electronic energy (in hartrees) and the summations are over all atoms in the molecule. For most molecules, very high levels of theory and/or large basis sets are required to achieve the accuracy required for thermochemistry. Composite approaches, such as G2 [3], G3 [4], and the Complete Basis Set (CBS) method [5], can simulate higher levels of theory by combining multiple calculations and empirical corrections to achieve the required accuracy. These methods have been applied to relatively large molecules (as many as 14 non-hydrogen atoms [5]), but such methods can become very time-consuming or limited by available memory space. In the case of individual high-level methods, such as coupled cluster theory, the method may be limited to species with no more than 4–5 non-hydrogen atoms. Thus, there is a need for theoretical approaches that can produce sufficient accuracy with minimal computational time for a broad spectrum of molecules, including ones with realistic numbers of atoms. In the case of tin oxide CVD, the common precursor MBTC has 8 non-hydrogen atoms and a total of 17 atoms.

A theoretical approach that we find predicts main-group thermochemistry quite successfully is the bond additivity correction (BAC) method [1, 6–8]. To date, BAC methods have been applied to and thermochemistry reported for compounds of boron [9, 10], carbon [7, 11], nitrogen [7], aluminum [10, 12], silicon [6, 13–20], and gallium [10]. The BAC methodology recognizes that errors in electronic energies are due to the use of finite basis set sizes and limited ability to model electron correlation. These errors are systematic and can be correlated with the number and type of bonds present in the molecule.

---

* This chapter includes text originally published as Section 4 of M. D. Allendorf, A. M. B. van Mol, "Gas-Phase Thermochemistry and Mechanism of Organometallic Tin Oxide Precursors," invited book chapter, *Topics in Organometallic Chem.*, Springer (Berlin) vol. 9, p. 1, 2005.

Thus, one can calibrate a theoretical method by applying corrections to the energy that scale with bond type and length, given an accurate heat of formation for a molecule containing at least one of the bond type of interest. While there are now several BAC methods based on different levels of theory, the original approach calculated the electronic energy using fourth-order Møller-Plesset perturbation theory (BAC-MP4) [1, 6, 7]. A modified version developed to predict thermochemistry for tin compounds is discussed below. At the time the BAC methodology was developed, the MP4(SDTQ) level of theory represented a compromise between accuracy and practical limits on computational time. With today's considerably faster machines, higher levels of theory are feasible. For example, thermochemistry obtained from BAC-G2 predictions have also been published [8, 10, 12]. However, as will be seen from the results presented below, in many cases this is not necessary.

There are two important limitations to this method. First, reference compounds are needed to establish the BAC parameters for each bond type. Although in general only one compound is needed (two or more may be required if multiple bonding is possible, as in the case of hydrocarbons), for many CVD precursors this proves to be an impediment. One can sometimes work around the problem, however, by using very high levels of theory to predict the heat of formation for a small molecule containing the bond type of interest.

A second limitation is that perturbation theory may not yield accurate results for molecules with "multireference" ground states, that is, compounds in which multiple electronic configurations mix in the ground state. In these cases, higher levels of theory are required. For tin compounds, we find that compounds containing unsaturated oxygen atoms are particularly problematic, and for these cases we developed approaches using coupled-cluster (CC) theory to predict the electronic energy. Although CC theory is not a true multireference approach, using high levels of this theory—including at least a perturbative correction for connected triples (the CCSD(T) method)—can successfully correct for the effects of a multireference wave function in weak to moderately multireference systems [21]. Both the BAC-MP4 method and the CC theory applied to tin compounds are described in more detail below.

2.2 Introduction to the BAC-MP4 Method

The basic aspects of the BAC-MP4 method used to predict thermochemistry for main-group molecules have been previously described [6], and a detailed description of its extension to compounds containing tin is published [22]. However, a brief summary is presented here to orient the reader. Electronic structure calculations are performed using Gaussian 98 [23]. Since the element tin is not included in the standard split-valence basis sets basis used by the BAC-MP4 method (6-31G(d) for equilibrium geometries and frequencies; 6-31G(d,p) for the electronic energy), the CRENBL relativistic effective core potential (ECP) of LaJohn et al. was incorporated in the method [24].† In this ECP, the core consists of the 1s–4p electrons, and the valence 4d105s25p2 electrons are modeled with an uncontracted Gaussian basis set containing 3s, 3p, and 4d functions. Restricted Hartree-Fock theory (RHF) is used to obtain geometries and frequencies for closed-shell molecules and unrestricted Hartree-Fock theory (UHF) for the open-shell molecules. It is well known that vibrational frequencies calculated at this level of theory are systematically larger than experimental values. Thus, each calculated frequency is scaled by dividing it by the established scaling factor of 1.12 [25].

† Basis sets were obtained from the Extensible Computational Chemistry Environment Basis Set Database, Version 12/03/03, as developed and distributed by the Molecular Science Computing Facility, Environmental and Molecular Sciences Laboratory which is part of the Pacific Northwest Laboratory, P.O. Box 999, Richland, Washington 99352, USA, and funded by the U.S. Department of Energy. The Pacific Northwest Laboratory is a multiprogram laboratory operated by Battelle Memorial Institute for the U.S. Department of Energy under contract DE-AC06-76RLO 1830. Contact David Feller or Karen Schuchardt for further information.

To determine atomization enthalpies and thus heats of formation, the effects of electron correlation are included by performing single-point calculations, using Møller-Plesset perturbation theory and the HF/6-31G(d) geometries. MP4(SDTQ) calculations (fourth-order perturbation theory using the 6-31G(d,p) basis set with single, double, triple and quadruple substitutions) are performed to obtain electronic energies. Systematic errors in the electronic energies obtained from these calculations are corrected using the BAC formalism:

$$E_{\mathrm{BAC}}(X_i\text{–}X_j) = f_{ij}g_{kij} \tag{2-3}$$

where

$$f_{ij} = A_{ij}\exp(-\alpha_{ij}R_{ij}) \tag{2-4}$$

$$g_{kij} = (1. - h_{ik}h_{ij}) \tag{2-5}$$

$$h_{ik} = B_k\exp\{-\alpha_{ik}(R_{ik} - 1.4\ \text{Å})\} \tag{2-6}$$

A_{ij} and α_{ij} are empirically derived parameters that depend on the X_i–X_j bond type, and R_{ij} is the bond distance (Å). The factor B_k in eq 2-6 is used to derive a correction for the effects of neighboring atoms on the X_i–X_j bond (eq 2-5) and depends on the identity of atom k. Corrections for UHF instability and non-zero ground state spin are also applied; the form of these is described elsewhere.[6]

There are two major sources of uncertainty in the BAC-MP4 heats of formation. First, there are uncertainties resulting from incomplete knowledge of the appropriateness of the chosen theoretical methods for a given molecule. Second, systematic uncertainties exist that result from the lack of good reference compounds needed to establish the bond additivity corrections. The magnitude of the first is estimated using an ad hoc method developed previously that uses the results from lower-level calculations (Table 2-1).

$$\begin{aligned}(\text{BAC-MP4}) = \{&1.0\ \text{kcal/mol} + (\Delta H_{\text{BAC-MP4}} - \Delta H_{\text{BAC-MP3}})^2 + \\ &(\Delta H_{\text{BAC-MP4}} - \Delta H_{\text{BAC-MP4SDQ}})^2 + 0.25(E_{\text{BAC}}(\text{spin}_S{}^2) \text{ or } E_{\text{BAC}}(\text{spin}_{\text{UHF-I}}))^2\}^{1/2}\end{aligned} \tag{2-7}$$

The second and third terms on the right-hand side provide a measure of the convergence from lower to higher levels of theory, while the last term accounts for errors associated with spin contamination of the ground state or UHF instability (see [6] for additional details).

Table 2-1. BAC parameters for the BAC-MP4 (SDTQ) level of theory.

Bond	A_{ij} (MP4)[a]	α_{ij}(MP4)[b]
Sn-H	147.39	2.0
Sn-C	472.71	2.0
Sn-Cl	951.85	2.0
C-H	38.61	2.0
C-C	1444.09	3.8
Atom	**B_k(MP4)**	**E[c]**
Sn	0.30	-68.2232532
H	0.00	-0.4982320
C	0.31	-37.7508008
Cl	0.42	-459.5702737

[a] in kcal mol^{-1}
[b] in $Å^{-1}$
[c] (hartree)

The second source of uncertainty can add a few kcal/mol to the uncertainty estimates and scales with the number of bonds in the molecule. The use of different reference values would shift our calculated heats of formation as a group, with the consequence that calculated bond dissociation enthalpies and reaction enthalpies are affected less than the heats of formation. Overall, we believe that the uncertainties in the BAC-MP4 heats of formation lie in the ±2–7 kcal/mol range.

The BAC-MP4 method requires the user to select reference compounds whose heats of formation are well known so that the BAC parameters can be established. When such compounds do not exist, we resort to values predicted by high-level calculations, which naturally may introduce some error. In the case of tin compounds, the Sn–H, Sn–C, and Sn–Cl corrections were established using the heats of formation for SnH_4 [27], $Sn(CH_3)_4$ [27], and $SnCl_4$ [28] as references. No data for Sn–O compounds could be found, other than for SnO and SnO_2 [28]. Such small molecules, which are highly unsaturated and have multireference ground states, are not accurately modeled by perturbation theory. Instead, the correction for Sn–OH species is based on the CC prediction (see above) for H_3SnOH. These corrections and the MP4 level of theory yield results that are both in reasonable agreement with the limited available data for compounds with Sn–Cl and Sn–CH_3 ligands, but also give well-behaved trends in heats of formation for ligand substitution.

2.3 Coupled Cluster Method for Unsaturated Oxygen-Containing Compounds

Details of the computational procedure used to calculate thermodynamic data for tin compounds with unsaturated oxygen ligands are presented elsewhere [26]. Briefly, electronic energies are obtained using the coupled-cluster singles and doubles method with a perturbative correction for connected triple substitutions (CCSD(T)) and the Brueckner doubles method with analogous corrections for triple and quadruple substitutions (BD(TQ)). Correlation-consistent triple- and quadruple-zeta basis sets in conjunction with the large-core Stuttgart-Dresden-Bonn relativistic effective core potential and a core

polarization potential for tin are used to describe the molecular electronic structure. A correction for basis set incompleteness, computed from extrapolations to the infinite basis set limit, is also included. Heats of formation are determined from isogyric reactions, in which the number of electron pairs is conserved, rather than atomization reactions, since we believe the former to be more accurate for computing heats of formation. At this time we have not formulated a method for estimating the error in these calculations, so this is not given in Table 2-1 for the values determined by this method.

2.4 Heats of Formation for Tin-Containing Compounds

Representative heats of formation predicted by the ECP/BAC-MP4 method are given in Table 2-1 (the complete thermodynamic data set used in the analyses below were published separately and are available on the Internet [29]). Data are shown for a range of compounds, including tetravalent, trivalent, and divalent coordination at tin. Values for the reference compounds $SnCl_4$, SnH_4, and $Sn(CH_3)_4$ are also given. Finally, heats of formation for atoms and groups needed to calculate reaction enthalpies are given. These results are used in the analysis below to identify potential reaction pathways for MBTC and its decomposition products.

Note that the error estimates obtained from eq 2-7 are, in the majority of cases, less than ±2 kcal/mol. This indicates that the computational method is converging well from the lowest level of perturbation theory through to the highest. The only exceptions to this are the divalent singlet radicals (compounds of the form XSnY), in which there is a nonzero correction for UHF instability. In these cases, the ad hoc error estimation method indicates a higher level of uncertainty because the presence of UHF instability is an indication that the MP4(SDTQ) level of theory is not fully adequate to describe the electronic ground state of the molecule (the same is true of a nonzero spin contamination correction).

Trends in heats of formation can be used to build confidence in the theoretical model as well as to make inferences concerning the nature of the chemical bonding. In particular, a now well-established method for evaluating the regularity of thermochemical data in a homologous series of compounds plots the heat of formation versus the number of ligands of a given type. This method has been used extensively for hydrocarbons and has been applied to organometallic compounds as well [27, 30]. In general, experimental investigations show that a plot of this type is usually quite linear. Such behavior is often rationalized as an indication that the bonding between the central metal atom and the ligand is localized, such that substitution of additional ligands does not affect the bonding of the others of that type. In past investigations we found that the BAC-MP4 method reproduces these trends for a wide range of closed-shell main-group compounds, which we take as a strong indication that the method is working correctly. This is particularly helpful in cases where the series of compounds is poorly characterized.

In the case of the various tin compounds examined here, several series display near-linear behavior, including H/Cl and CH_3/H. Data for $Sn(CH_3)_nH_{4-n}$ are shown in Figure 2-1. The change in the heat of formation as CH_3 is substituted for H is –11 kcal/mol. The near-perfect linearity of this plot is typical of substitutions for a number of ligand pairs in all of the main-group compounds we have examined to date, including those of C, Si, B, Al, and In. We are thus confident that the values given here are sufficiently accurate to be used for the qualitative analysis below and that the low uncertainties reported are a reflection of the high degree of convergence in the calculations.

In contrast, methyl-for-chlorine substitution is decidedly nonlinear, a feature also displayed by the lighter Group 14 compounds. This curvature is not an artifact of the BAC-MP4 predictions, since it is observable in the (admittedly limited) experimental data for these compounds (Figure 2-2). In fact, the deviations from linearity are even greater in the experimental data. Such behavior is also observed in the analogous Si compounds and is related to the negative hyperconjugation (anomeric) effect, in which electron

density from the CH_3 (a π donor) is transferred to the σ system of the Cl (a σ acceptor). These effects are well-documented for geminal ligands (e.g., YMH_2X) in compounds in which the central atom is either silicon or carbon (see Hehre et al. [5] and references therein).

Although experimental data available for comparison with these results are very limited, they indicate that the ECP/BAC-MP4 method performs well for classes of tin compounds containing H, OH, Cl, and organic ligands. In the case of tetravalent compounds, the predicted heats of formation are in good agreement with reported values for the series $Sn(CH_3)_{4-n}H_n$ (Table 2-1). Similarly, the agreement with experiment for the series $Sn(CH_3)_nCl_{4-n}$ is also good. Maximum deviations from experiment in this case are less than 3 kcal/mol. Unfortunately, there are almost no data for trivalent and divalent species, but the available values agree with the predicted ones within the error bars. Note that the large error estimate for $SnCl_3$ derives from the fact that this heat of formation is based the thermochemistry of analogous compounds. In this case, we think it likely that the BAC-MP4 is more accurate than the experimental value.

Results of applying the CCSD(T) method to selected tin compounds are also given in Table 2-1. Again, there are almost no data available in the literature for comparison. However, the predicted heat of formation for SnO is in reasonable agreement with experiment. Since data for Sn–O species are so limited, it is difficult to fully validate this model chemistry. Thus, we placed relatively high uncertainties on the calculated values. Nevertheless, we are sufficiently confident of the results to use them to establish BAC parameters for Sn–OH bonds. The resulting BAC-MP4 predictions as well as the CCSD(T) results should be sufficiently accurate to allow qualitative evaluation of reaction pathways involving them.

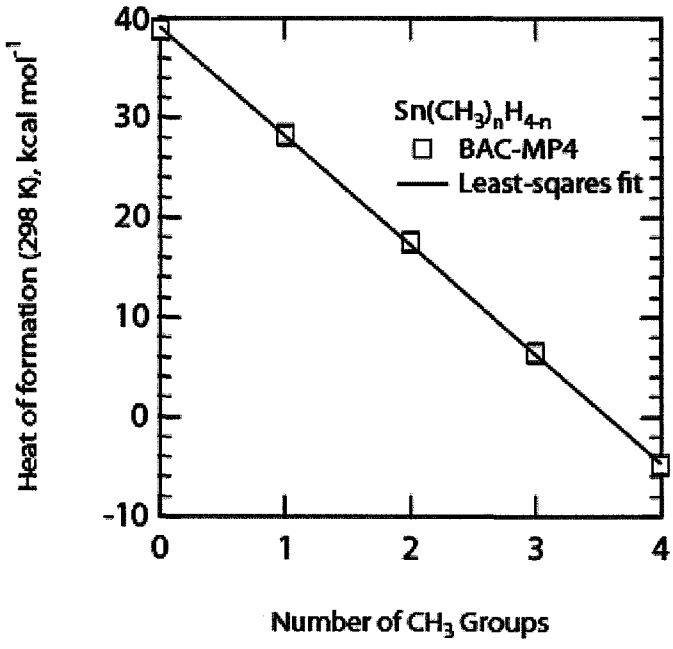

Figure 2-1. Heats of formation predicted for the series $Sn(CH_3)_{4-n}H_n$ by the BAC-MP4 method. The error bars shown correspond to the error obtained from the ad hoc method given in Equation 2-7.

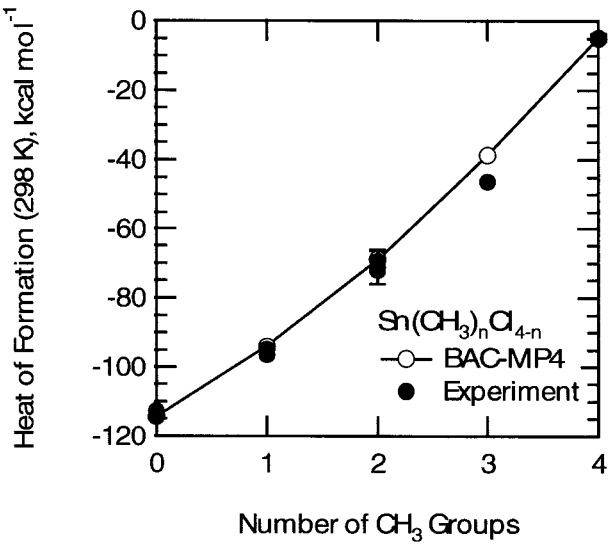

Figure 2-2. Heats of formation predicted for the series $Sn(CH_3)_{4-n}Cl_n$ by the BAC-MP4 method. The error bars shown correspond to the error reported for the experimental values, where available.

2.5 Bond Dissociation Energies in Tin Compounds

The availability of heats of formation allows one to calculate reaction enthalpies; such knowledge provides useful insight into the thermal stability and reactivity of a molecule. Bond dissociation enthalpies (BDEs) in particular, are quite valuable, since the breaking of the weakest bond in a molecule is typically the first step in the initiation of gas-phase chemistry during CVD. Thus, from a qualitative point of view, calculated BDEs allow the thermal stability of precursors to be compared. They are also critical to the calculation of unimolecular reaction rates using RRKM or other transition-state theories. The ab initio heats of formation reported here for tin compounds thus represent a starting point for understanding gas-phase chemistry occurring during CVD. Since comparable data also exist for compounds of carbon, silicon, and to a lesser extent, germanium, it is also possible to compare bonds between tin and typical ligands (e.g., H, CH_3, OH, and Cl), as well as evaluate trends as the central atom is changed.

In general, tin compounds extend and mirror the trends exhibited by their analogues higher in the periodic table, as seen in Figure 2-3. In particular, the strength of the Sn–ligand bond varies according to Sn–OH > Sn–Cl > Sn–H ~ Sn–alkyl. In all cases, these bonds are weaker than those of the analogous C, Si, or Ge compounds.[‡] Note that although the Sn–OH BDE is significantly stronger than the Sn–Cl bond, there is reason to believe that tin hydroxides will be less thermally stable than chlorinated organometallics, since the possibility for elimination of H_2O from the molecule opens a potential low-energy channel.

More important from the point of view of developing new CVD precursors is the lack of a strong variation in the Sn–C BDE as the organic group varies from CH_3 to C_4H_9 (Figure 2-4). These values vary by only ±2 kcal/mol for straight-chain alkyl groups (interestingly, there is a slight dip in the BDE for R = C_2H_5, regardless of the identity of the central atom). Significant weakening of the Sn–C bond strength can be achieved by using branched alkyl groups. For example, the Sn–$CH(CH_3)_2$ BDE is 61.3 kcal/mol, while

[‡] Note that although the calculated value of the Ge–Cl bond in $GeCl_4$ is comparable to that in $SnCl_4$, the uncertainty in this value is quite high due to the estimated heat of formation of $GeCl_3$.

the Sn–$CH_2CH_2CH_3$ BDE is 66.0 kcal/mol. This trend is not surprising and is mirrored by other Group 14 compounds [27, 31].

In the literature, there are two widely cited reports of Sn–CH_3 bond energies by Price et al., one for TMT [32] and one for DMTC [33]. These publications have been influential; for example, Giunta et al. [34] and Zawadzki et al. [35] used the results of Price et al. in their gas-phase oxidation mechanisms for TMT [32] and DMTC [33] oxidation, and Nash et al. [36] accepted the Price et al. [33] value for the first Sn–C dissociation in DMTC to calculate subsequent bond energies [36]. Both bond energies reported by Price et al. are significantly lower than the BAC-MP4 predictions: 64.5 kcal/molfor TMT versus 71 kcal/mol predicted by BAC-MP4, and 56.1 kcal/mol for DMTC versus 70 kcal/mol from BAC-MP4. These differences may result from several factors: (1) inaccuracy in the theoretical predictions, (2) pressure falloff in the gas-phase reaction rate, (3) radical reactions in the gas phase, and (4) wall reactions. While all may contribute to some degree, we feel it likely that the last two are the greatest contributors. The predicted errors in the BAC-MP4 calculations are small; the estimated error for the bond-dissociation reaction is only ±3 kcal/mol in both cases. Pressure falloff effects should also be minimal, since unimolecular reactions such as bond fission for molecules with large numbers of vibrational frequencies should be near their high-pressure limit, leading to an activation energy close to the bond dissociation energy [37]. As a result, we suspect that the onset of gas-phase reaction predicted by mechanisms using these bond energies will occur at somewhat lower temperatures than is actually the case.

Previous attempts to calculate bond energies in tin compounds employed levels of theory that were inadequate to provide accurate results. As discussed above, accurate bond energies require the use of either composite ab initio methods or methods employing a high level of electron correlation coupled with isogyric reactions to minimize basis set truncation and other systematic errors. Consequently, the results reported by Basch [38, 39], which use a number of uncorrected ab initio methods or with very simple corrections (i.e., across-the-board energy corrections by finite amounts), are unlikely to be particularly accurate.

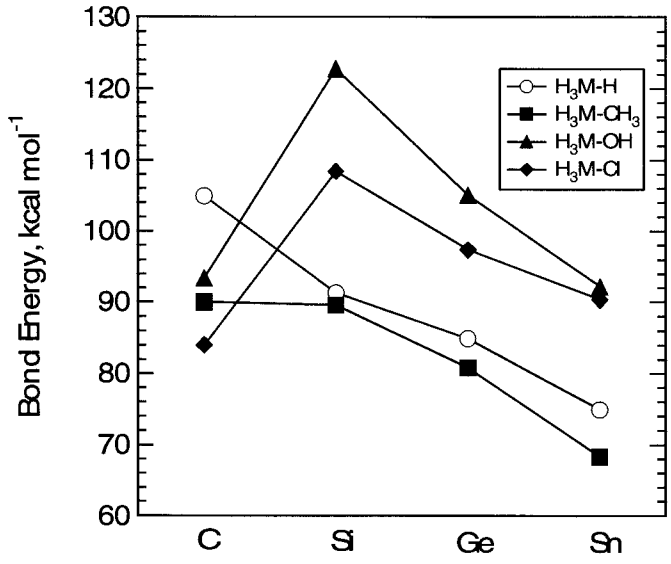

Figure 2-3. Bond dissociation energies (298 K) for compounds of the form H_3MR, where M = C, Si, Ge, or Sn and R = H, CH_3, OH, or Cl. Data obtained from BAC-MP4 calculations, except for M = Ge, where the data are obtained from G2 calculations.

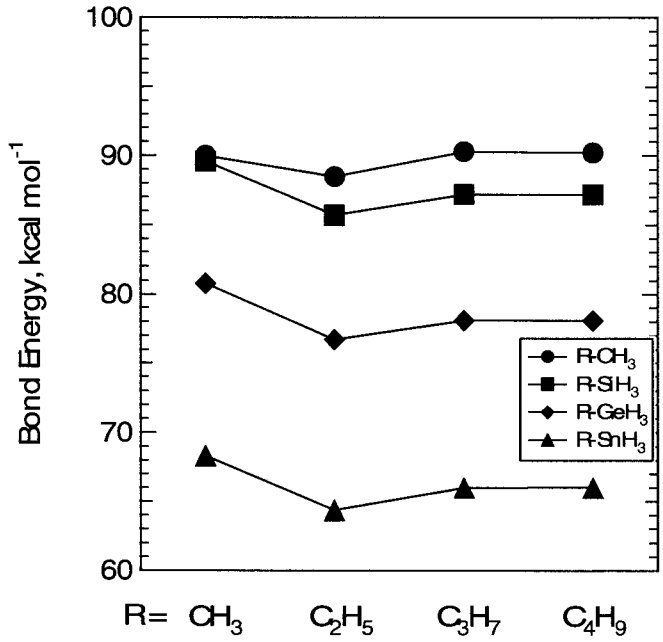

Figure 2-4. Bond dissociation energies (298 K) for compounds of the form H_3MR, where M = C, Si, Ge, or Sn and R = CH_3,C_2H_5, C_3H_7, C_4H_9. Data obtained from BAC-MP4 calculations, except for M = Ge, where the data are obtained from G2 calculations.

2.6 Complexes with Water

In addition to providing thermodynamic data for known species, ab initio methods can be part of the discovery process by predicting the stability of postulated, but unknown compounds. An important example of this arises in the development of mechanisms for tin oxide CVD involving water as a reactant. It is well known that the addition of water increases tin oxide deposition rates, but the mechanism for this effect is not clear. It might be expected that tetravalent tin halides could react with gas-phase water to produce five- or six-coordinate compounds, given the known behavior of these molecules (and other Group 14 halides in general) toward water: all Group 14 compounds of the form MCl_4 fume in air and some, such as $SiCl_4$, react violently with liquid water. Somewhat surprisingly, however, ab initio calculations indicate that no stable gas-phase complexes of $SiCl_4$ with either one or two water molecules exist, although other halides are predicted to do so [40]. Anecdotal evidence from glass manufacturers who use organometallics to deposit tin oxide as well as a patent concerning deposition from $SnCl_4$ and H_2O [41] suggest that if temperatures are maintained above 180°C, condensation can be avoided. Using the BAC-MP4 method, however, stable geometries for complexes of both tetravalent tin compounds and intermediate subchlorides with water were identified, suggesting that gas-phase reactions involving water vapor might contribute to the enhancement of deposition rates caused by the addition of water.

Figure 2-5 shows the calculated structure for a complex representative of those that could form between tin oxide MOCVD precursors and water. This compound, $Cl_3Sn(CH_3)(H_2O)_2$, contains two water molecules bound in axial positions through oxygen in an approximately octahedral geometry. The Sn-O bond lengths, which have inequivalent lengths, are considerably longer than Sn-OH bonds (predicted to be ~1.91 Å), suggesting that these molecules are relatively weakly bonded Lewis acid-base complexes. The BAC-MP4 heat of reaction for $Cl_3Sn(CH_3)(H_2O)_2$ supports this:

$$Cl_3SnCH_3 + 2H_2O \leftrightarrow Cl_3Sn(CH_3)(H_2O)_2 \qquad \Delta H°_R(298\ K) = -15.3\ kcal/mol \qquad (2\text{-}8)$$

Tin compounds with coordination numbers greater than 4 are well known [42]. Reactive groups such as OH must be shielded to isolate them, however, suggesting that the water complexes predicted by theory may be susceptible to internal reaction, such as loss of HCl. The reaction analogous to R2-1 involving $SnCl_4$ is even more exothermic (–23 kcal/mol). It is therefore conceivable that tin oxide precursors such as DMTC react to form complexes in the gas phase at temperatures below those required for pyrolysis (≥450 °C for MBTC; see below). However, the stabilization resulting from increasing numbers of electronegative ligands suggests that complexes between tin oxide precursors such as $Sn(CH_3)_4$ and water may not be thermodynamically favored.

Reactions such as 2-8 could be followed by elimination of two HCl molecules to yield a dihydroxide:

$$Cl_3Sn(CH_3)(H_2O)_2 \leftrightarrow SnCl(CH_3)(OH)_2 + 2HCl \qquad \Delta H°_R(298\ K) = 30.5\ kcal/mol \qquad (2\text{-}9)$$

$$Cl_3Sn(CH_3)(H_2O)_2 + 2Cl \leftrightarrow SnCl(CH_3)(OH)_2 + 2HCl \qquad \Delta H°_R(298\ K) = -27.5\ kcal/mol \qquad (2\text{-}10)$$

which is equivalent to an average reaction energy of ~15 kcal/mol for each HCl molecule generated. Alternatively, the complex generated by 2-8 could react exothermically with two gas-phase Cl atoms (2-10) to produce the dihydroxide. However, because the subsequent unimolecular decomposition steps are endothermic (e.g., 2-9), the complexes may fall apart before they reach the regions where sufficient thermal energy is available for them to either decompose unimolecularly or undergo H-atom abstraction.

When MBTC and DMTC undergo pyrolysis, tin subchlorides form complexes that can also react with water to form complexes that BAC-MP4 calculations suggest are stable. When MBTC decomposes, $SnCl_3$ (2-1) is formed, while DMTC initially reacts to form $SnCl_2CH_3$. Decomposition of these two

species leads to formation of $SnCl_2$. Calculated heats of formation for complexes between these tin subchlorides and one or two water molecules suggest that the reaction is exothermic (e.g., R2-11 and R2-12). In all cases, the water molecules are bound to the tin atom through their oxygen atom. As an example, the complex $Cl_2(CH_3)SnOH_2$ is shown in Figure 2-6. This four-coordinate molecule has a very long Sn–OH_2 bond distance of 2.897 Å, unlike the much shorter Sn–O bond in the six-coordinate complexes described above.

$$SnCl_3 + H_2O \leftrightarrow Cl_3SnOH_2 \qquad \Delta H°_{react}(298\ K) = -12.7\ kcal/mol \qquad (2\text{-}11)$$

$$SnCl_2(CH_3) + H_2O \leftrightarrow Cl_2(CH_3)SnOH_2 \qquad \Delta H°_{react}(298\ K) = -9.1\ kcal/mol \qquad (2\text{-}12)$$

The coordination number can be increased further by the addition of a second water molecule, for example:

$$Cl_3SnOH_2 + H_2O \leftrightarrow Cl_3Sn(OH_2)_2 \qquad \Delta H°_{react}(298\ K) = -11.4\ kcal/mol \qquad (2\text{-}13)$$

The O–H bond in these complexes is relatively weak, suggesting that formation of the hydroxide should occur at temperatures below those required to crack the initial precursor.

$$Cl_3SnOH_2 \leftrightarrow Cl_3SnOH + H \qquad \Delta H°_{react}(298\ K) = 36.6\ kcal/mol \qquad (2\text{-}14)$$

By comparison, all bonds other than Sn–C in the tin hydroxides are quite strong. In Cl_3SnOH, the bond energies are 125 kcal/mol, 95 kcal/mol, and 87 kcal/mol for the O–H, Sn–O, and Sn–Cl bonds, respectively. Thus, it appears likely that the hydroxide ligand is quite stable and could survive transit through the thermal boundary layer in a CVD reactor and form tin oxide. We conclude from this analysis that reactions between both tin-containing MOCVD precursors and their decomposition products may be important pathways leading to the formation of thermodynamically stable hydroxides. These qualitative results are supported by equilibrium calculations described in Chapter 3. Additional theory directed toward determining transition states for possible HCl elimination reactions and experiments to measure rate constants of reactions with water are needed, however, to provide a quantitative assessment of the importance of this chemistry.

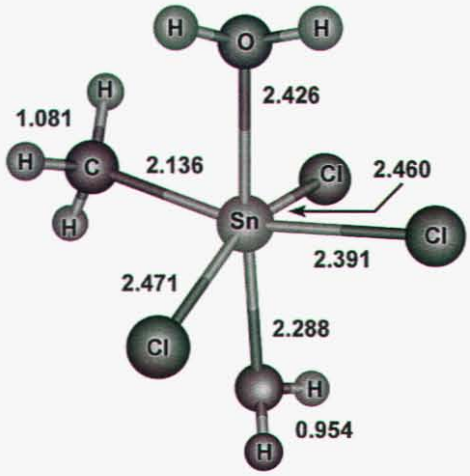

Figure 2-5. Structure of the $Cl_3Sn(CH_3)(H_2O)_2$ complex at the MP2/6-31G(d,p) level resulting from the BAC-MP4 calculation for this molecule. Distances are in Å.

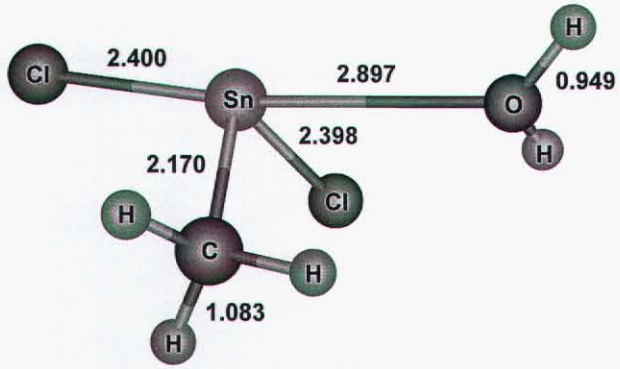

Figure 2-6. Structure of the complex $Cl_2(CH_3)SnOH_2$ at the MP2/6-31G(d,p) level resulting from the BAC-MP4 calculation for this molecule. Distances are in Å.

2.7 References

1. C. F. Melius, M. D. Allendorf, M. E. Colvin (1997) In: C. Bernard, M. D. Allendorf (eds) Fourteenth *Int. Symp. Chem. Vapor Deposition*, vol 97–25. The Electrochemical Society Proceedings Series, Pennington p 1
2. W. J. Hehre, L. Radom, P. R. Schleyer, J. A. Pople (1986) *Ab Initio Molecular Orbital Theory*. Wiley, New York
3. L. A. Curtiss, K. Raghavachari, G. W. Trucks, J. A. Pople (1991) *J. Chem. Phys.* 94: 7221
4. L. A. Curtiss, K. Raghavachari, P. C. Redfern, V. Rassolov, J. A. Pople (1998) *J. Chem. Phys.* 109: 7764
5. J. W. Ochterski, G. A. Petersson, J. A. Montgomery (1996) *J. Chem. Phys.* 104: 2598
6. P. Ho, C. F. Melius (1990) *J. Phys. Chem.* 94: 5120
7. C. F. Melius (1990) In: S. N. Bulusu (ed) Chemistry and Physics of Energetic Materials (NATO ASI Series), vol 309. Kluwer Academic Publishers, Dorderecht p 21
8. C. F. Melius, M. D. Allendorf (2000) *J. Phys. Chem.* 104: 2168
9. M. D. Allendorf, C. F. Melius (1997) *J. Phys. Chem.* A 101: 2670
10. M. D. Allendorf, C. F. Melius, C. Bauschlicher Jr. (1999) *J. Phys. Fr.* IV 9: 23
11. M. R. Zachariah, P. R. Westmoreland, D. R. Burgess, W. Tsang (1996) *J. Phys. Chem.* 100: 8737
12. M. D. Allendorf, C. F. Melius, B. Cosic, A. Fontijn (2001) *J. Phys. Chem.* A 106: 2629
13. M. D. Allendorf, C. F. Melius (1992) *J. Phys. Chem.* 96: 428
14. M. D. Allendorf, C. F. Melius (1993) *J. Phys. Chem.* 97: 720
15. M. .D Allendorf, C. F. Melius, P. Ho, M. R. Zachariah (1995) *J. Phys. Chem.* 99: 15285
16. P. Ho, M. E. Coltrin, J. S. Binkley, C. F. Melius (1985) *J. Phys. Chem.* 89: 4647
17. P. Ho, M. E. Coltrin, J. S. Binkley, C. F. Melius (1986) *J. Phys. Chem.* 90: 3399
18. P. Ho, W. G. Breiland, R. W. Carr (1986) *Chem. Phys.* Lett. 132: 422
19. P. Ho, C. F. Melius (1995) *J. Phys. Chem.* 99: 2166

20. C. F. Melius, P. Ho (1991) *J. Phys. Chem.* 95: 1410

21. C. J. Cramer (2003) *Essentials of Computational Chemistry.* Wiley, Chichester

22. M. D. Allendorf, C. F. Melius (2005) *J. Phys. Chem.* 109, 4939

23. M. J. Frisch, G. W. Trucks, H. B. Schlegel, P. M. W. Gill, B. G. Johnson, M. A. Robb, J. R. Cheeseman, T. Keith, G. A. Petersson, J. A. Montgomery, K. Raghavachari, M. A. Al-Laham, V. G. Zakrzewski, J. V. Ortiz, J. B. Foresman, J. Cioslowski, B. B. Stefanov, A. Nanayakkara, M. Challacombe, C. Y. Peng, P. Y. Ayala, W. Chen, M. W. Wong, J. L. Andres, E. S. Replogle, R. Gomperts, R. L. Martin, D. J. Fox, J. S. Binkley, D. J. Defrees, J. Baker, J. P. Stewart, M. Head-Gordon, C. Gonzalez, J. A. Pople (1998) *Gaussian 98.* Gaussian, Inc., Pittsburgh

24. L. A. LaJohn, P. A. Christiansen, R. B. Ross, T. Atashroo, W. C. Ermler (1987) *J. Chem. Phys.* 87: 2812

25. A. P. Scott, L. Radom (1996) *J. Phys. Chem.* 100: 16502

26. I. M. B. Nielsen, C. L. Janssen, M. D. Allendorf (2002) *J. Phys. Chem.* A 107: 5122

27. J. A. M. Simoes, J. F. Liebman, S. W. Slayden (1995) In: S. Patai (ed) *The Chemistry of Organic Germanium, Tin, and Lead Compounds.* Wiley, New York p 245

28. L. V. Gurvich, I. V. Veyts, C. B. Alcock (1994) *Thermodynamic Properties of Individual Substances.* CRC Press, Boca Raton

29. M. D. Allendorf, C. F. Melius, **www.ca.sandia.gov/HiTempThermo**

30. J. D. Cox, G. Pilcher (1970) *Thermochemistry of Organic and Organometallic Compounds.* Academic, London

31. R. Walsh (1981) *Acc. Chem. Res.* 14: 246

32. R. P. Johnson, S. J. W. Price (1972) *Can. J. Chem.* 50: 50

33. S. J. W. Price, A. F. Trotman-Dickenson (1958) *Trans. Faraday Soc.* 54: 1630

34. C. J. Giunta, D. A. Strickler, R. G. Gordon (1993) *J. Phys. Chem.* 97: 2275

35. A. G. Zawadzki, C. J. Giuna, R. G. Gordon (1992) *J. Phys. Chem.* 96: 5364

36. G. A. Nash, H. A. Skinner, W. F. Stack (1965) *Faraday Soc. London Trans.* 61: 640

37. R. G. Gilbert, S. C. Smith (1990) *Theory of Unimolecular and Recombination Reactions.* Blackwell, Oxford

38. H. Basch (1996) *Inorganica Chim. Acta* 252: 265

39. H. Basch, T. Hoz (1995) In: S. Patai (ed) *The Chemistry of Organic Gemanium, Tin, and Lead Compounds.* Wiley, New York p 1

40. I. S. Ignatyev, H. F. Schaeffer III (2001) *J. Phys. Chem.* 105: 7665

41. S. J. Hurst, B. J. Kirkbride, D. W. Sheel (1997), Great Britain patent EP0755902A2

42. K. M. Mackay (1995) In: S. Patai (ed) *The Chemistry of Organic Gemanium, Tin, and Lead Compounds.* Wiley, New York

This page intentionally left blank.

Chapter 3 Gas-Phase Chemical Reactions*

Although the temperatures typically encountered in tin oxide CVD processes are too low and the residence times too short to expect that the system will come to thermodynamic equilibrium, calculation of the equilibrium composition using Gibbs free-energy minimization techniques is a useful starting point for the development of chemical mechanisms. Species in the highest concentration at equilibrium are those for which there is the greatest free-energy driving force for their formation. While the identity of these species is often obvious for systems such as hydrocarbons, in the case of chemistries that are less well characterized, such as the tin oxide CVD systems of interest here, it is unclear which species are most stable. Two useful equilibrium models are (1) global equilibrium to determine ultimate chemical endpoints (i.e., those species that will form given sufficient time at a given temperature) and (2) partial equilibrium, in which some or all of the most stable species are not included in the calculation. The latter case has the effect of imposing an infinite kinetic barrier between those species and the precursors, allowing a second tier of species to form that may represent short-lived but important intermediates in the reaction process. In both cases, condensed phases are excluded, since these are so much more stable than gas-phase species, that were they to be included, essentially no gas-phase species would form, yielding little insight into the processes occurring in the gas prior to deposition.

We present results for two standard tin oxide precursors, DMTC and MBTC, as well as for tin tetrachloride. The latter compound is included in the analysis to provide perspective on the thermal stability of the inorganic system ($SnCL_4$) relative to the organometallic ones. All chemical equilibrium calculations were performed with the EQUIL-code from the Chemkin-suite [1], using the thermochemical data discussed in the previous sections. The temperature range selected was 298–1023 K, the concentration of tin precursor was kept at 2 mol%, while the concentrations of oxygen and water were held at 20 and 5 mol%, respectively. The total pressure was 1 atm. These conditions are similar to those used in commercial tin oxide CVD processes. Note that in the following discussion of reaction mechanisms, all heats of reaction ($\Delta H°_R$) are given at 298 K.

This chapter also describes an experimental investigation of the decomposition kinetics of MBTC. Using a stirred-tank reactor and detection of gas-phase species using Fourier transform infrared (FTIR) spectroscopy, the rate constant for MBTC decomposition at 1 atm was measured. In addition, gas-phase decomposition products were detected, whose identity confirms the qualitative details of the pyrolysis mechanism described in Section 3.3.2.

3.1 $SnCl_4$

Global equilibrium calculations for $SnCl_4$ in N_2 and with excess O_2 reveal that $SnCl_4$ is the most stable tin species over a wide temperature range (Figure 3-1). Experimentally, it is found that no deposition of tin oxide occurs from 1–3% $SnCl_4$ + 20% O_2 mixtures at temperatures up to at least 923 K [2]. In contrast, $SnCl_4$ + H_2O mixtures with no additional O_2 can be used to deposit SnO_2 at temperatures as low as 670 K. Under these conditions, global equilibrium calculations predict tin hydroxides such as Cl_3SnOH will

* The text in this chapter was originally published as in the following papers: 1) Section 5 of M. D. Allendorf, A. M. B. van Mol, "Gas-Phase Thermochemistry and Mechanism of Organometallic Tin Oxide Precursors," invited book chapter, *Topics in Organometallic Chem.*, Springer (Berlin) vol. 9, p. 1, 2005, and 2) Sections 2 and 3.1 of A. M. B. van Mol, M. D. Allendorf,"Decomposition, Oxidation, and Hydrolysis Kinetics of Monobutyltintrichloride," *Proc. 16th Int. Conf. Chem. Vapor Dep./EUROCVD-14*, The Electrochemical Society Proceedings Series, Vol. 2003-08, p. 65.

become the most stable gas phase species, rather than $SnCl_4$. As described above, complexes with water vapor, such as $Cl_4Sn(OH_2)_2$, may be intermediates in the formation of these hydroxides. Although intramolecular loss of two HCl molecules to form $Cl_2Sn(OH)_2$ is endothermic ($\Delta H°_R$ = 34.6 kcal/mol), other kinetically favorable pathways may exist that lead to tin hydroxides (see also Sec. 3.3.2), which may be the actual gas-phase precursors to tin oxide. It is also possible, however, that $SnCl_4$ is hydrolyzed on the surface without prior reaction in the gas phase. The combined evidence from the experiments and equilibrium calculations indicates, in any case, that SnO_2 deposition from $SnCl_4$ requires formation of HCl, which provides a thermodynamic sink to stabilize the chlorine in the molecule.

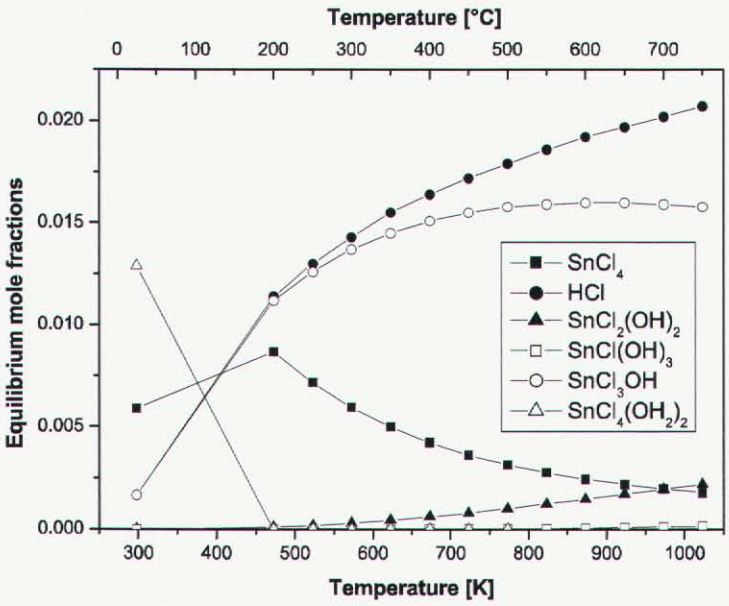

Figure 3-1. Predicted equilibrium gas-phase species for 2 mole% $SnCL_4$ and 5 mole% H_2O.3.2 $SnCl_2(CH_3)_2$

3.1.1 Equilibrium Predictions

The equilibrium calculations for DMTC decomposition in N_2 are consistent with previously reported experimental investigations, which show that DMTC decomposes above 670 K into $SnCl_2$, C_1, and C_2 hydrocarbons [3]. The only discrepancy is the predicted formation of C_6H_6, which has not been found during experiments. This is not surprising, since the higher hydrocarbons formed by recombination of methyl radicals (primarily C_2H_6 and C_2H_4) created by the initial decomposition of DMTC (see below) are unlikely to recombine and form higher hydrocarbons.

Figure 3-2 shows the most stable species at equilibrium for the oxidation of 2 mol% DMTC in the presence of oxygen (20 mol%) and water (5 mol%). $RSnCl_3$ and $SnCl_4$ species were excluded from the calculations because these species, although thermodynamically very stable, are unlikely to form due to the very low concentration of gas-phase Cl atoms in the system and the strong Sn-Cl bond in $SnCl_2$. Including these species would thus unrealistically skew the predictions of the equilibrium calculations. As in the case of $SnCl_4$, chlorinated tin hydroxides are the most stable species. The hydrocarbon ligands are almost completely oxidized to CO_2 and H_2O (not shown in the figure). Similar results are found without the presence of water in the initial mixture, because water is also a byproduct of DMTC oxidation.

If Sn(IV) hydroxides are excluded from the calculation, thereby creating the equivalent of an infinite kinetic barrier to their formation, the results indicate that $SnCl_2$ is the most abundant tin-containing species. Other gas-phase tin oxides, such as Cl_2SnO, $-O(SnCl_2)O-$ (cyclic), SnO, or SnO_2 do not form. Also, the species predicted by Giunta et al. [4], $Cl_2CH_3SnCH_2OO$ and Cl_2CH_3SnO, are not formed in any significant amount. This suggests that as DMTC enters the thermal boundary layer above a heated substrate, it decomposes into $SnCl_2$ and CH_3 groups, which subsequently oxidize to form CO_2 and H_2O. $SnCl_2$ might react further to form tin hydroxides, if kinetically favorable pathways exist, or instead react directly with the surface.

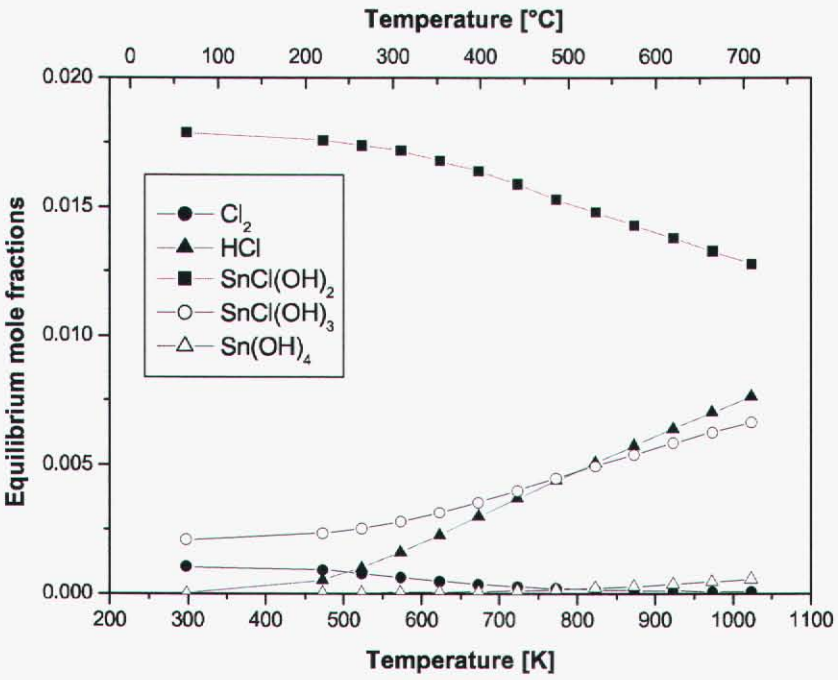

Figure 3-2. Concentrations of gas-phase species at equilibrium as a function of temperature for 2% DMTC, 20% O_2, and 5% H_2O in nitrogen carrier gas at 1 atm total pressure.

3.1.2 Reaction Path Analysis

As discussed in Chapter 2, Giunta et al. published a mechanism describing the gas-phase oxidation of DMTC [4]. At the time of this work, very little thermodynamic data were available for the tin species involved in their mechanism. Consequently, many of the reactions they employed are irreversible (i.e., reverse reaction rates could not be calculated using the equilibrium constant). While much of the chemistry contained in this mechanism is reasonable based on comparison with analogous hydrocarbon reactions (particularly the radical abstraction reactions), now that thermochemical data are available for the tin species, it is possible to examine the heats of reaction to determine whether these reactions used are in fact energetically favorable. The oxidation of DMTC is considerably more complex than the chemistry of either $SnCl_4$ or MBTC (discussed below) and thus it is not possible to obtain a clear picture of the relevant reaction pathways simply by looking at the thermochemistry. Nevertheless, considerable insight can still be gained, pointing to areas that require additional attention.

Mixtures used to deposit tin oxide from DMTC normally contain both oxygen and water vapor. We are not aware of any evidence that DMTC can react directly with oxygen in the gas phase. Previously published mechanisms (including Giunta et al.) assume that gas-phase oxidation of DMTC is initiated by pyrolysis of DMTC, with the first step being Sn–C bond scission (Reaction 3-1 below), requiring

significant thermal energy to break the bond. This is reasonable, since this is by far the weakest bond in DMTC. For comparison, the C–H bond is 103.3 kcal/mol, and the Sn–Cl bond is 94.8 kcal/mol.

$$(CH_3)_2SnCl_2 \leftrightarrow CH_3SnCl_2 + CH_3 \qquad \Delta H°_R = 69.7 \text{ kcal/mol} \qquad (3\text{-}1)$$

Prior to the BAC-MP4 results for chlorinated organotin species reported here, there were no data available for DMTC bond energies other than the experimental investigation by Price and Trotman-Dickenson [5], who found 56 kcal/mol for the energy of $Cl_2(CH_3)Sn–CH_3$. Giunta et al. employ these results in their mechanism. As discussed earlier, there are good reasons to believe the experimental bond energy is much too low, causing the onset of gas-phase pyrolysis predicted by Giunta et al. to occur faster at low temperatures than is realistic. Estimates of the Sn–C bond energy in non-halogenated compounds have been published, with values around 70 kcal/mol reported for Sn-CH_3 bonds [6, 7], in agreement with the BAC-MP4 results, as discussed above.

Although 3-1 appears to be the most likely initiation reaction, we cannot rule out a process in which water vapor and DMTC react, based on the ab initio results described in Sec. 2.6. If this does occur, however, it apparently does not lead to homogeneous nucleation of particles, since anecdotal evidence from the glass industry indicates that DMTC and water vapor can be premixed prior to APCVD of tin oxide without substantial buildup of solids in delivery lines. Perhaps this is due to significant kinetic barriers to the decomposition of the tin–water complexes that initially form, so that further gas-phase reaction does not occur until the reactants enter the heated boundary layer above the substrate.

Bond cleavage reactions subsequent to 3-1 were not considered by Giunta et al. The predicted bond energies suggest, however, that 3-1 is likely followed by rapid cleavage of the second Sn–C bond, for which the bond energy is only 23.5 kcal/mol. This rather weak bond is typical of Group 14 trivalent radicals, as discussed previously for organometallic silicon compounds [8].

$$CH_3SnCl_2 \leftrightarrow SnCl_2 + CH_3 \qquad \Delta H°_R = 23.5 \text{ kcal/mol} \qquad (3\text{-}2)$$

Thus, two straightforward reactions lead directly to the thermodynamically most stable tin compound at deposition temperatures, $SnCl_2$. Both 3-1 and 3-2 produce methyl radicals that can also react with DMTC, as given by Giunta et al.:

$$(CH_3)_2SnCl_2 + CH_3 \leftrightarrow Cl_2Sn(CH_3)CH_2 + CH_4 \qquad \Delta H°_R = -1.5 \text{ kcal/mol} \qquad (3\text{-}3)$$

Extraction of atoms or groups other than H by CH_3 is not expected to be kinetically favorable. The DMTC radical, $Cl_2Sn(CH_3)CH_2$, formed in 3-3 has relatively strong bonds to carbon:

$$Cl_2Sn(CH_3)CH_2 \leftrightarrow Cl_2SnCH_2 + CH_3 \qquad \Delta H°_R = 50.2 \text{ kcal/mol} \qquad (3\text{-}4)$$

$$Cl_2Sn(CH_3)CH_2 \leftrightarrow CH_3SnCl_2 + CH_2 \qquad \Delta H°_R = 77.3 \text{ kcal/mol} \qquad (3\text{-}5)$$

However, if sufficient thermal energy is available in the system to break the Sn–C bond in DMTC, then loss of CH_3 from $Cl_2Sn(CH_3)CH_2$ via R21 should also occur. This leads to formation of Cl_2SnCH_2, which has a relatively weak Sn–C bond (only 49.8 kcal/mol) and may decompose further to yield $SnCl_2$ and CH_2. (Note, however, that since CH_2 has a triplet ground state, this reaction may be kinetically unfavorable due to the intersystem crossing required to form it from singlet Cl_2SnCH_2.)

Reaction of O_2 with $SnCl_2$ is discussed in detail in the section below concerning MBTC. To briefly summarize, formation of the cyclic compound –O($SnCl_2$)O– is predicted by BAC-MP4 calculations. However, equilibrium calculations predict that this species is not thermodynamically stable relative to

$SnCl_2$ at CVD temperatures. In addition, exothermic reactions with radicals that could provide a sink for removal of $-O(SnCl_2)O-$ are rare, making it unlikely that oxidation of $SnCl_2$ proceeds through this compound. Thus, it seems unlikely that $SnCl_2$ reacts extensively with O_2.

The oxidation of the methyl radicals formed by DMTC pyrolysis is well understood compared with the tin chemistry. Gas-phase mechanisms describing this chemistry are readily available [9–11]. These reactions lead to the formation of other reactive species that can attack DMTC, including H, O, OH, and HO_2. The OH radical, in particular, is a very efficient H-abstractor and will therefore quickly react with DMTC:

$$(CH_3)_2SnCl_2 + OH \leftrightarrow (CH_3SnCl_2)CH_2 + H_2O \qquad \Delta H°_R = -15.9 \text{ kcal/mol} \qquad (3\text{-}6)$$

The radical $Cl_2Sn(CH_3)CH_2$ can react with oxygen via 3-7 through 3-9, which are all quite exothermic, supporting Giunta et al.'s model, in which these are the principal chain carriers.

$$Cl_2Sn(CH_3)CH_2 + O_2 \leftrightarrow Cl_2Sn(CH_3)CH_2OO \qquad \Delta H°_R = -22.7 \text{ kcal/mol} \qquad (3\text{-}7)$$

$$Cl_2Sn(CH_3)CH_2OO \leftrightarrow Cl_2(CH_3)SnO + CH_2O \qquad \Delta H°_R = -37.5 \text{ kcal/mol} \qquad (3\text{-}8)$$

$$(CH_3)_2SnCl_2 + Cl_2(CH_3)SnO \leftrightarrow Cl_2(CH_3)SnOH + Cl_2Sn(CH_3)CH_2$$

$$\Delta H°_R = -20.4 \text{ kcal/mol} \qquad (3\text{-}9)$$

Giunta et al. also propose that CH_3SnCl_2 formed in R1 reacts with oxygen:

$$CH_3SnCl_2 + O_2 \rightarrow Cl_2(CH_3)SnO + O \qquad \Delta H°_R = 41.5 \text{ kcal/mol} \qquad (3\text{-}10)$$

$$Cl_2SnCH_3 + O_2 \leftrightarrow Cl_2Sn(CH_3)OO \qquad \Delta H°_R = -24.7 \text{ kcal/mol} \qquad (3\text{-}11)$$

$$Cl_2SnCH_3 + O_2 \leftrightarrow Cl_2SnCH_2 + HO_2 \qquad \Delta H°_R = 59.9 \text{ kcal/mol} \qquad (3\text{-}12)$$

$$Cl_2Sn(CH_3)OO \leftrightarrow Cl_2Sn(CH_3)O + O \qquad \Delta H°_R = 65.6 \text{ kcal/mol} \qquad (3\text{-}13)$$

Reaction 3-10 is endothermic, suggesting a large kinetic barrier. Giunta et al. estimated a 15 kcal/mol barrier height, which is unrealistic based on the predicted thermochemistry. Thus, this step probably represents a minor reaction channel. Peroxide formation from CH_3SnCl_2, however, is very exothermic (3-11). Reaction 3-11 is a "chemically activated" process (as is 3-7), in which the initially formed complex $[Cl_2Sn(CH_3)OO]^{\dagger}$ is energetically hot and can undergo further decomposition[12]. For example, 3-12 and 3-13 may also occur and other exit channels are conceivable as well, such as $Cl_2Sn(CH_2)O + OH$. Determination of which channel dominates requires not only the relevant thermochemistry, but may also require a master-equation approach to the calculation of reaction rates, which we have not undertaken here. However, the high endothermicities of 3-12 and 3-13 suggest that these reactions are unimportant. Several low-energy pathways are then available that eventually lead to Cl_2SnO:

$$Cl_2Sn(CH_3)OO + OH \leftrightarrow Cl_2Sn(CH_3)O + HO_2 \qquad \Delta H°_R = 0.4 \text{ kcal/mol} \qquad (3\text{-}14)$$

$$Cl_2Sn(CH_3)OO + H \leftrightarrow Cl_2Sn(CH_3)O + OH \qquad \Delta H°_R = -36.6 \text{ kcal/mol} \qquad (3\text{-}15)$$

$$Cl_2Sn(CH_3)OO + CH_3 \leftrightarrow Cl_2Sn(CH_3)O + CH_3O \qquad \Delta H°_R = -24.9 \text{ kcal/mol} \qquad (3\text{-}16)$$

$$Cl_2Sn(CH_3)O \leftrightarrow Cl_2SnO + CH_3 \qquad \Delta H°_R = 37.3 \text{ kcal/mol} \qquad (3\text{-}17)$$

Whether or not the peroxide formed in 3-11 can be stabilized after formation of the initial reactive complex and then react via 3-14 through 3-17 is unclear. The equilibrium calculations described above do not indicate that Cl_2SnO is a stable molecule under deposition conditions. Rather, $SnCl_2$ is the thermodynamically favored tin-containing fragment of DMTC. This species is produced by 3-2, which therefore competes with 3-11. Since the number of species decreases in the forward direction of 3-11, entropy favors $SnCl_2$ formation over the peroxide (although negative at 298 K, ΔG^0_R for 3-11 becomes positive at deposition temperatures). Furthermore, the enthalpy of the reverse reaction (3-11) is comparable to that of 3-2, suggesting that if sufficient thermal energy exists to drive R19, then 3-11 should be near equilibrium. Thus, we suspect that DMTC completely decomposes to $SnCl_2$, rather than proceeding from 3-1 to 3-11. Two routes are then possible for $SnCl_2$. It can react with H_2O formed by oxidation of the methyl radicals, thereby subsequently forming the hydroxides predicted by the equilibrium calculations (see Sec. 3.3.2 below). Alternatively, it may react directly with O– or –OH groups on the surface to form SnO_2.

In the mechanism of Giunta et al., CH_3SnCl_2OH, formed by exothermic reaction of CH_3SnCl_2O with CH_4, H_2CO, or HO_2, is a key species whose decomposition leads to gas-phase SnO and SnO_2 formation. A potentially important pathway to form CH_3SnCl_2OH not considered by these authors is reaction with HCl:

$$Cl_2Sn(CH_3)O + HCl \leftrightarrow Cl_2Sn(CH_3)OH + Cl \qquad \Delta H^0_R = -20.6 \text{ kcal/mol} \qquad (3\text{-}18)$$

While not as exothermic as a reaction with HO_2 or H_2CO, HCl should be present in much higher concentrations, such that (3-18) may be the primary route to CH_3SnCl_2OH formation. This compound decomposes via two nonelementary (and irreversible) reactions proposed by Giunta et al.:

$$CH_3SnCl_2OH \rightarrow SnO + CH_3 + Cl + HCl \qquad \Delta H^0_R = 174 \text{ kcal/mol} \qquad (3\text{-}19)$$

$$CH_3SnCl_2OH + O_2 \rightarrow SnO_2 + CH_3 + ClO + HCl \qquad \Delta H^0_R = 176 \text{ kcal/mol} \qquad (3\text{-}20)$$

These reactions are required in the Giunta et al. mechanism to reproduce the DMTC consumption and tin oxide deposition rates, which are too low without them. These steps are rate-limiting in the mechanism and are thus crucial to the understanding of the overall chemistry. However, their overall very high endothermicity, coupled with the equilibrium calculations discussed above indicating that SnO and SnO_2 are at least orders of magnitude lower in concentration than $SnCl_2$, suggest that other chemistry must be employed to account for the DMTC loss and tin oxide growth rates. Based on our experience in attempting to measure the gas-phase kinetics of organometallic compounds, which are prone to react on surfaces, we suggest that DMTC consumption and tin oxide growth via heterogeneous reactions is quite likely and may be a major contributor to the growth rates observed by Giunta et al. This is not to say that gas-phase chemistry is not occurring; on the contrary, it may be quite important under the conditions Giunta et al. were attempting to model (a horizontal laminar-flow reactor operating at atmospheric pressure and temperatures of 793–893 K). However, the rate-limiting step may in fact be a surface process.

When water vapor is also present, numerous exothermic pathways exist that could accelerate DMTC oxidation in the gas phase and form alternate precursors. Reactions involving water are not included in the mechanism of Giunta et al. Formation of complexes with up to two H_2O ligands bound to $SnCl_2$ (through the oxygen atom) is exothermic. (For simplicity, we did not examine structures containing more than two water ligands, but formation of these may be possible.)

$$SnCl_2 + H_2O \leftrightarrow Cl_2SnOH_2 \qquad \Delta H°_R = -20.7 \text{ kcal/mol} \qquad (3\text{-}21)$$

$$Cl_2SnOH_2 + H_2O \leftrightarrow Cl_2Sn(OH_2)_2 \qquad \Delta H°_R = -15.3 \text{ kcal/mol} \qquad (3\text{-}22)$$

Once these form, highly exothermic channels involving H, OH, and the relatively abundant Cl radicals become available. For example, some pathways leading to $SnCl_2(OH)_2$ (the hydroxide with the highest concentration at equilibrium) are as follows:

$$Cl_2SnOH_2 + Cl \leftrightarrow Cl_2SnOH + HCl \qquad \Delta H°_R = -13.9 \text{ kcal/mol} \qquad (3\text{-}23)$$

$$Cl_2Sn(OH_2)_2 + 2H \rightarrow\rightarrow Cl_2Sn(OH)_2 + 2H_2 \qquad \Delta H°_R = -81.3 \text{ kcal/mol} \qquad (3\text{-}24)$$

$$Cl_2Sn(OH_2)_2 + 2Cl \rightarrow\rightarrow Cl_2Sn(OH)_2 + 2HCl \qquad \Delta H°_R = -79.3 \text{ kcal/mol} \qquad (3\text{-}25)$$

$$Cl_2SnOH_2 + OH \leftrightarrow Cl_2SnOH + H_2O \qquad \Delta H°_R = -30.5 \text{ kcal/mol} \qquad (3\text{-}26)$$

$$Cl_2Sn(OH_2)_2 + 2OH \rightarrow\rightarrow Cl_2Sn(OH)_2 + 2H_2O \qquad \Delta H°_R = -112.6 \text{ kcal/mol} \qquad (3\text{-}27)$$

Stripping of chlorine from hydroxides such as $Cl_2Sn(OH)_2$ could eventually lead to gas-phase SnO or SnO_2. However, at the relatively low temperatures typical of tin oxide CVD (~873–973 K), we do not expect these oxides to form, based on the equilibrium calculations described above. Thus, the formation of tin hydroxides is not only thermodynamically favored (i.e., based on minimization of the Gibbs free energy), but there are also exothermic reaction pathways that we expect to be kinetically favorable. The primary tin carrier in the CVD process could therefore be a tin hydroxide. Complete conversion to SnO_2 would most likely occur via reactions on the surface.

3.2 $SnCl_3(C_4H_9)$

3.2.1 Equilibrium Predictions

Figure 3-3 indicates that the most stable tin compounds for an input reaction mixture containing excess H_2O and O_2 (2% MBTC/5% H_2O/20% O_2) are again tin hydroxides, with Cl_3SnOH being the most stable tin-containing species. MBTC itself is not present in significant concentrations under these conditions. The hydrocarbon ligands are almost completely oxidized to CO_2 and H_2O (not shown in Figure 3-3), and chlorine reacts to form HCl. Other tin-containing species, such as Cl_2SnO, SnO_2, and SnO, do not form, nor do the peroxide compounds Cl_3SnOO and Cl_3SnOOH. The results indicate that unsaturated tin species are not stable under these conditions and that the primary tin-carrying precursors are tin hydroxides, as in the case of DMTC. Similar results are obtained when the input mixture to the equilibrium calculation contains only MBTC and O_2.

The removal of hydroxides from the calculation creates the equivalent of an infinite kinetic barrier to their formation and allows potentially reactive (i.e., short-lived) intermediates to be identified. Tin tetrachloride is also excluded from the calculation, since it is such stable species that if included, it would be by far the dominant species, preventing identification of much less stable intermediates. Excluding $SnCl_4$ from these calculations is not unreasonable, since its formation would occur either by recombination of $SnCl_3$ with Cl atoms, whose concentration relative to oxygen will be extremely low during the early stages of decomposition, or by extraction from HCl ($SnCl_3 + HCl \leftrightarrow SnCl_4 + H$), which is endothermic by 19 kcal/mol. In addition, extraction of Cl by $SnCl_3$ from other chlorine-containing tin species is not expected to be very efficient due to high strength of Sn-Cl bonds.

Results of such calculations are seen in Figure 3-4 for the mixture 2% MBTC/20% O_2 (molar basis) in nitrogen. Now the tin compounds in highest concentration are Cl_3SnOO and Cl_3SnOOH at temperatures below ~725 K and $SnCl_3$ and $SnCl_2$ at higher temperatures, although significant concentrations of tin–oxygen species still exist at temperatures >725 K. The two peroxide compounds are intermediates that

could form as the initial product of MBTC decomposition, $SnCl_3$, reacts with oxygen in the heated boundary layer above the surface. At the higher temperatures typical of the gases close to the substrate, these peroxides are not stable and revert to $SnCl_3$ and $SnCl_2$; with sufficient thermal energy, however, they may react further to yield tin hydroxides. The addition of 5% H_2O to the input mixture does not shift the predicted concentrations significantly, since H_2O already forms in significant amounts from MBTC/O_2 mixtures.

Figure 3-5 shows the species in highest concentration predicted for a mixture of MBTC and water without oxygen (2% MBTC/5% H_2O, molar basis). These equilibrium calculations include both tin hydroxides and $SnCl_4$. However, $SnCl_2$ is now the dominant tin-containing molecule at temperatures above 600 K. At lower temperatures, which premixed reactants would encounter as they enter a CVD reactor, complexes of the tin subchlorides $SnCl_3$ and $SnCl_2$ with water, as well as $SnCl_4$ and the hydroxide Cl_3SnOH, are predicted to form. Since little or no MBTC decomposition is expected at these temperatures [13], formation of such species seems kinetically unlikely. More plausible would be direct formation of a water–MBTC complex, as discussed in Sec. 2.6. Although we do not have thermodynamic data for these complexes, the absence of $SnCl_4(H_2O)_2$, which was included in the calculations, suggests that analogous complexes involving MBTC would not be stable at these temperatures. However, these complexes might still function as intermediates, potentially leading to Cl_3SnOH formation. The absence of stable tin–oxygen intermediates at equilibrium may explain why tin oxide cannot be deposited from MBTC/H_2O mixtures. Only carbon can be deposited under these conditions [13], in contrast with MBTC/O_2 mixtures, in which (Figure 3-4) a number of oxygen-containing tin compounds are present at temperatures around 723 K, where MBTC begins to decompose [13].

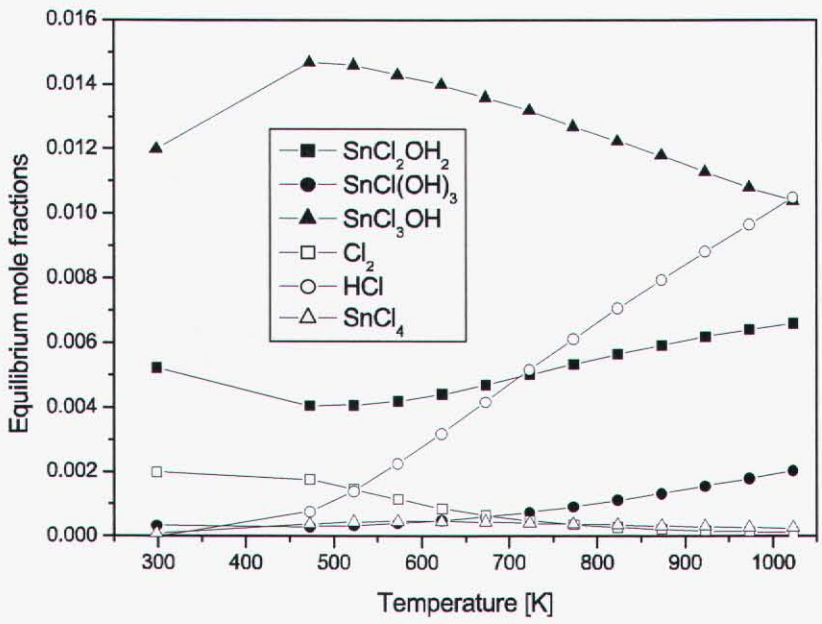

Figure 3-3. Predicted equilibrium gas-phase species present in the oxidation of MBTC (2%) in the presence of water (5%) and oxygen (20%).

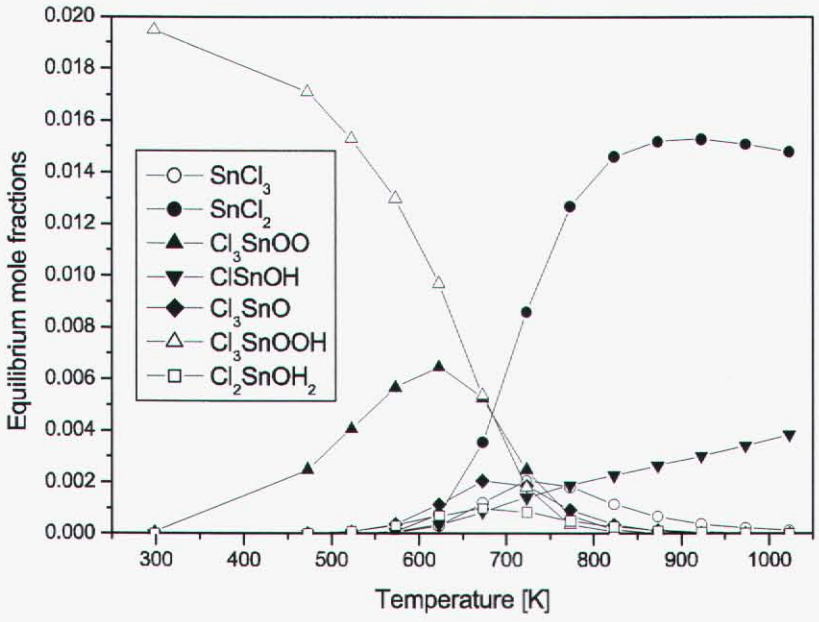

Figure 3-4. Predicted equilibrium gas-phase species for MBTC/O_2 (2%/20% v/v); tetravalent tin hydroxides and tin tetrachloride were not allowed to form.

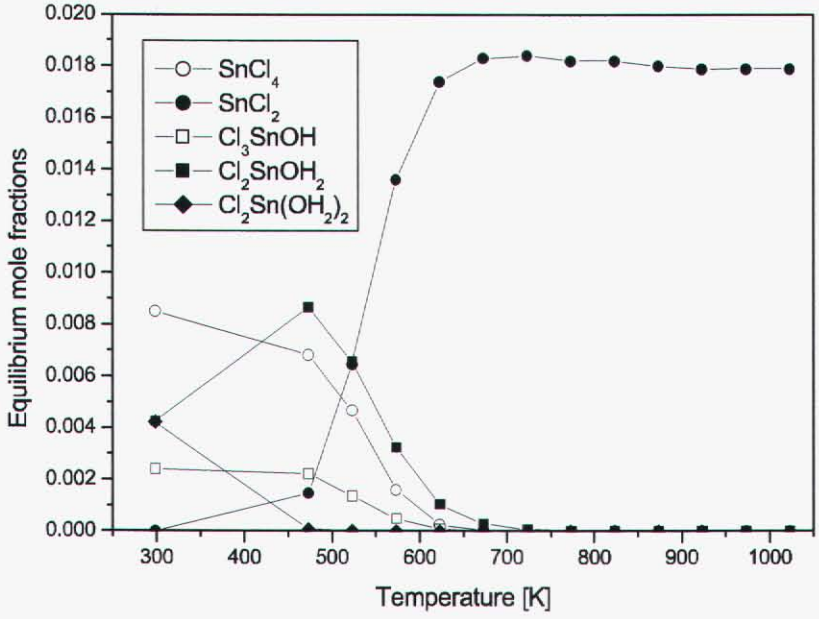

Figure 3-5. Predicted equilibrium gas-phase species present in the oxidation of MBTC/H_2O (2%/5%).

3.2.2 Reaction Path Analysis

Reactant mixtures used to make tin oxide from MBTC on an industrial scale contain both water vapor and oxygen. As suggested for DMTC, reaction is probably initiated by MBTC pyrolysis, since there is no evidence that MBTC itself can react with O_2 in the gas phase. Thus, simple bond-breaking pathways are the likely initiation reactions; for example:

$$C_4H_9SnCl_3 \leftrightarrow SnCl_3 + C_4H_9 \qquad \Delta H°_R = 68.9 \text{ kcal/mol} \qquad (3\text{-}28)$$

At 69 kcal/mol, the Sn–C bond is the weakest in the MBTC molecule. For comparison, the Sn–Cl bond in $SnCl_4$, which is expected to be similar to MBTC, is 84 kcal/mol. Similarly, C–C bonds are of order 90 kcal/mol (in ethane, the bond energy is 91 kcal/mol), making 3-28 the most probable initiation pathway.

Decomposition of the C_4H_9 radical is well understood [14] and occurs rapidly as follows:

$$C_4H_9 \leftrightarrow C_2H_4 + C_2H_5 \qquad \Delta H°_R = 21.5 \text{ kcal/mol} \qquad (3\text{-}29)$$

$$C_2H_5 + Cl \leftrightarrow C_2H_4 + HCl \qquad \Delta H°_R = -67.6 \text{ kcal/mol} \qquad (3\text{-}30)$$

$$C_2H_5 \leftrightarrow C_2H_4 + H \qquad \Delta H°_R = 35.6 \text{ kcal/mol} \qquad (3\text{-}31)$$

Rate constants for these reactions are available in the literature, and all three can be considered well understood for purposes of this discussion. The primary hydrocarbon product identified experimentally is C_2H_4, which qualitatively confirms this mechanism (small concentrations of butene are also found) [13, 15].

The $SnCl_3$ radical may proceed via the following reaction:

$$SnCl_3 \leftrightarrow SnCl_2 + Cl \qquad \Delta H°_R = 42.9 \text{ kcal/mol} \qquad (3\text{-}32)$$

The relative weakness of the Sn–Cl bond in this case reflects a trend observed in all Group 14 compounds, in which BDEs in a series MX_n (n = 2–4) follow the order $MX_4 > MX_3$ and $MX_2 > MX_3$ [16]. For example, the bond energies in $SnCl_4$, $SnCl_3$, and $SnCl_2$ are 84.2, 42.9, and 91.1 kcal/mol based on our combined BAC-MP4 and CC results. The relatively weak bond in $SnCl_3$ makes the rate of 3-32 fast relative to 3-29, and thus not rate-limiting.

Once $SnCl_3$ and/or $SnCl_2$ form, additional reactions involving molecular oxygen or water vapor may occur. $SnCl_3$ can react exothermically with oxygen to form peroxide, while peroxide formation from $SnCl_2$ is only lightly endothermic:

$$SnCl_3 + O_2 \leftrightarrow Cl_3SnOO \qquad \Delta H°_R = -27.7 \text{ kcal/mol} \qquad (3\text{-}33)$$

$$SnCl_2 + O_2 \leftrightarrow [Cl_2SnOO]^{\dagger} \leftrightarrow -O(SnCl_2)O- \text{ (cyclic)} \quad \Delta H°_R = 5.3 \text{ kcal/mol} \qquad (3\text{-}34)$$

Unimolecular decomposition of Cl_3SnOO is highly endothermic (reactions 3-35 and 3-36 for example), but exothermic decomposition pathways involving H-atoms exist (3-38 and 3-39). Reaction with Cl atoms is endothermic (3-37), however:

$$Cl_3SnOO \leftrightarrow Cl_3SnO + O \qquad \Delta H°_R = 73.6 \text{ kcal/mol} \qquad (3\text{-}35)$$

$$Cl_3SnOO \leftrightarrow -O(SnCl_2)O- \text{ (cyclic)} + Cl \qquad \Delta H°_R = 75.9 \text{ kcal/mol} \qquad (3\text{-}36)$$

$Cl_3SnOO + Cl \leftrightarrow -O(SnCl_2)O-$ (cyclic) $+ Cl_2$ $\Delta H°_R = 17.9$ kcal/mol (3-37)

$Cl_3SnOO + H \leftrightarrow -O(SnCl_2)O-$ (cyclic) $+ HCl$ $\Delta H°_R = -27.3$ kcal/mol (3-38)

$Cl_3SnOO + H \leftrightarrow SnCl_3O + OH$ $\Delta H°_R = -28.8$ kcal/mol (3-39)

$-O(SnCl_2)O- + Cl \leftrightarrow -O(SnCl)O- + Cl_2$ $\Delta H°_R = -19.5$ kcal/mol (3-40)

Reactions 3-38 and 3-39 may not make a major contribution to the overall removal of Cl_3SnOO, however, since H is present in such small concentrations (much smaller than Cl, according to equilibrium predictions). Nevertheless, formation of $SnCl_3O$ via 3-39 does provide an exothermic route to the most stable tin hydroxide identified by the equilibrium calculations:

$SnCl_3O + RH \leftrightarrow SnCl_3OH + R$ (RH = HCl, H_2O, or MBTC) (3-41)

$\Delta H°_R$ is negative for all R indicated in 3-41 (as much as –24.6 kcal/mol when RH is MBTC) and since all RH are present in substantial amounts during deposition, these pathways could be at least minor contributors to hydroxide formation.

Ab initio calculations indicate that Cl_2SnOO rearranges to the compound $-O(SnCl_2)O-$. Abstraction of a chlorine atom from this heterocycle by H, O, OH, or Cl is exothermic (e.g., 3-40 above). Reaction 3-40, in particular, appears to be a kinetically favorable path, since chlorine atoms are in relative abundance. However, equilibrium calculations predict that this cyclic compound is not thermodynamically stable relative to $SnCl_2$, since very little forms. Thus, the initial peroxide complexes formed when the tin-containing fragments of MBTC react with oxygen will likely fall apart via the reverse of their formation reaction (unless they react with a hydrogen atom), leading to small steady-state concentrations of these species.

In contrast, there are numerous exothermic pathways involving water vapor. Ab initio calculations indicate that formation of complexes with up to two H_2O ligands bound to $SnCl_2$ or $SnCl_3$ (through the oxygen atom) is exothermic. For simplicity, we did not examine structures containing more than two water ligands, but formation of these may be possible. For example, as discussed in Sec. 2.5:

$SnCl_2 + 2H_2O \leftrightarrow Cl_2Sn(OH_2)_2$ $\Delta H°_R = -20.7$ kcal/mol (3-42)

$SnCl_3 + 2H_2O \leftrightarrow Cl_3Sn(OH_2)_2$ $\Delta H°_R = -12.8$ kcal/mol (3-43)

Once these form, highly exothermic channels involving Cl (which is relatively abundant and an effective H-atom abstractor, H, and OH radicals become available. For example, some pathways leading to $SnCl_3OH$ (the hydroxide at equilibrium with the highest concentration) are as follows:

$Cl_3SnOH_2 + H \leftrightarrow Cl_3SnOH + H_2$ $\Delta H°_R = -67.7$ kcal/mol (3-44)

$Cl_3SnOH_2 + Cl \leftrightarrow Cl_3SnOH + HCl$ $\Delta H°_R = -66.7$ kcal/mol (3-45)

$Cl_3SnOH_2 + OH \leftrightarrow Cl_3SnOH + H_2O$ $\Delta H°_R = -82.8$ kcal/mol (3-46)

Stripping chlorine ligands from hydroxides such as Cl_3SnOH or $Cl_2Sn(OH)_2$ could eventually lead to gas-phase SnO or SnO_2. However, at the relatively low temperatures typical of tin oxide CVD (~873–973 K), we do not expect this based on the equilibrium calculations described above. Even intermediate

decomposition products such as Cl_2SnO, which is thermodynamically quite stable in the analogous silicon system, are not predicted to form, as evidenced by 3-47 below:

$$Cl_3SnOH \leftrightarrow Cl_2SnO + HCl \qquad \Delta H°_R = 73.2 \text{ kcal/mol} \qquad (3\text{-}47)$$

Thus, the primary tin carrier in the CVD process is again expected to be a tin hydroxide, whose conversion to SnO_2 is most likely on the deposition surface.

3.3 Measurements of MBTC Decomposition in a Stirred Tank Reactor

3.3.1 Introduction

The calculations described in Section 3.2 suggest that the chemistry and kinetics of MBTC thermal decomposition, oxidation, and hydrolysis reactions in the gas phase are a critical element in model development. In this section the focus is on analyzing the gas-phase reactions occurring during deposition of tin oxide. Experiments were performed in a continuously stirred tank reactor (CSTR) system, where concentration and temperature distributions can be neglected, thus allowing analysis of the intrinsic chemical kinetics.

3.3.2 Experimental Procedures

The system used for conducting the experiments is depicted in Figure 3-6. The heart of the system is a hot-wall quartz spherical continuously stirred tank reactor (CSTR). The gases are brought into the reactor through four nozzles of a cross-shaped injector, placed just below the centre of the reactor in two orthogonal planes. The diameter of the reactor, 120 mm, and the diameter of the nozzles, 1 mm, were chosen on the basis of fluid dynamics relations of axial symmetric jets as proposed by David and Matras [17]. The reactor is placed inside an electrical resistance furnace (Watlow) with a capacity of 1000 W. Reactor temperature is regulated by means of a PID-controller (Watlow), using a K-type thermocouple located in a thermo-well, placed near the center of the reactor. The gases entering the reactor are preheated to prevent temperature gradients [18]. This reactor configuration prevents the occurrence of significant concentration and temperature distributions, allowing for monitoring intrinsic reaction kinetics. Analysis of the gas phase in the reactor is performed by means of Fourier transformed infrared spectroscopy (FTIR). The FTIR (MIDAC 2500) has a spectral resolution between 0.5 and 32 cm^{-1} and is equipped with an MCT or a DTGS detector. The FTIR was calibrated for MBTC, CH_4, C_2H_4, HCl, CH_2O, CO, CO_2, and H_2O to allow quantitative measurement of gas-phase species.

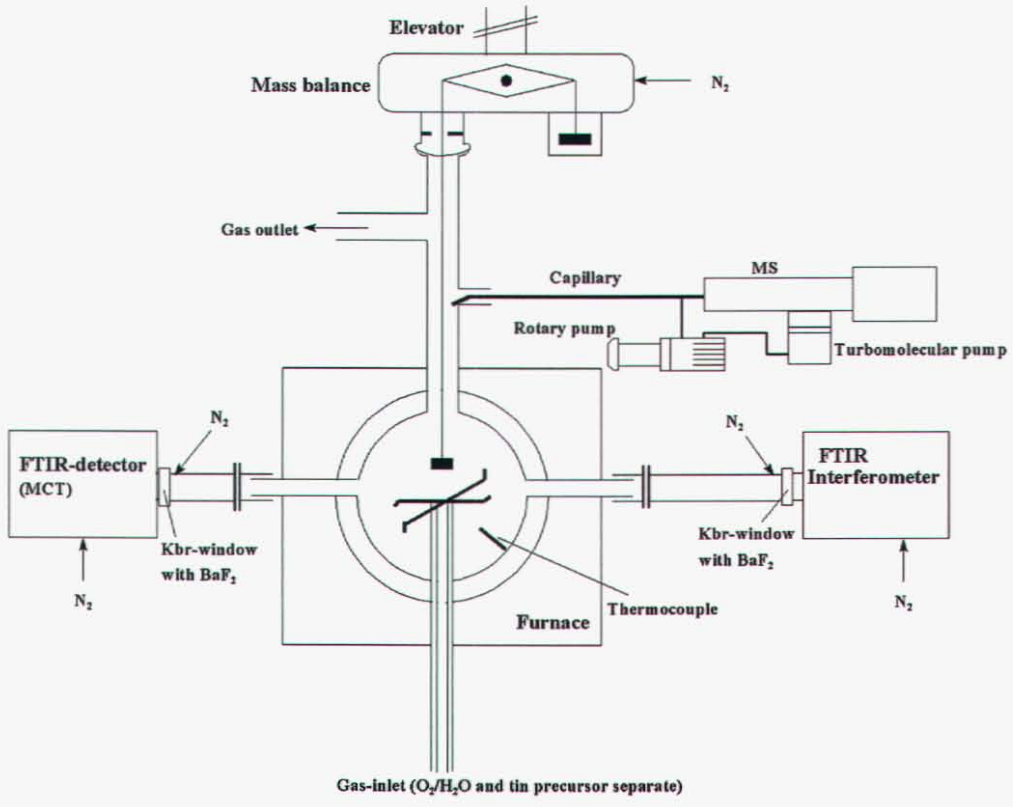

Figure 3-6. Experimental setup of CSTR system.

Experiments were performed at atmospheric pressure and reactor temperatures ranging from 643 to 903 K. The concentration of MBTC at every temperature was varied between 0.5 and 3 mol%. The preheater was set at 723 K, the same temperature as the reactor till. However, above 723 K, MBTC starts to decompose, so the preheater is kept at 723 K for experiments conducted at temperatures of 723 K and above. The residence time in the reactor was kept at 2 s for all experiments. For experiments where tin oxide is expected to deposit, a 10×10×0.7 mm borosilicate glass (Corning 7059) substrate is suspended in the reactor. Deposition rates are determined by ex-situ measuring the mass increase of the substrate gained during the experiment.

Flow rates of nitrogen (Hoekloos, 99.999%) were controlled by thermal mass flow controllers (Brooks). The flow of MBTC is established by bubbling nitrogen through an isothermal vessel containing liquid MBTC (99+%). The flow rate of MBTC is controlled by the bubbler efficiency and the vapor pressure of MBTC at the temperature of the vessel, which was kept at 448 K. The relation used for the vapor pressure of MBTC is [19]

$$\log P(\text{Torr}) = 9.1 - 3.070 * 1000/T(\text{K}) \tag{3-48}$$

Calibration of the bubbler revealed a bubbler efficiency of 75%.

For every experiment the system is allowed 2 minutes to stabilize before any spectra were recorded. This means that during decomposition experiments, the reactor was precoated with carbon, and during deposition experiments, the reactor was precoated with tin oxide.

3.3.3 Results and Discussion

3.3.3.1 Decomposition of MBTC

Figure 3-7 depicts two typical FTIR spectra recorded during pyrolysis and oxidation of MBTC. Decomposition of MBTC starts in the CSTR at about 723 K. Products detected using FTIR are mainly HCl and C_2H_4, with minor amounts of CH_4 and 1-C_4H_8. X-ray diffraction analysis of powder in the exhaust reveals that $SnCl_2$ also is formed during pyrolysis. At 873 K, all MBTC has been converted.

The conversion of MBTC between 723 K and 873 K has been used to determine an overall decomposition rate of MBTC at 1 atm. The overall rate can be determined by applying the mass balance over an ideal CSTR and assuming a first-order dependence

$$[\mathrm{MBTC}]_{out} = [\mathrm{MBTC}]_{in}/(1 + k * \tau) \tag{3-49}$$

where $[\mathrm{MBTC}]_{out}$ is the concentration of MBTC in the reactor as measured by FTIR shown in Figure 3-8. For an ideal CSTR, this is identical to the concentration of MBTC leaving the reactor. $[\mathrm{MBTC}]_{in}$ is the concentration of MBTC entering the reactor, τ is the residence time in the reactor, and k is the overall rate constant. This overall rate constant is assumed to follow the Arrhenius equation. Linear least squares analysis yields a rate constant for MBTC decomposition in N_2 at 1 atm of

$$k = 3.6 \times 10^8 \exp(-15115/T)\ s^{-1} \tag{3-50}$$

The overall activation energy for decomposition is thus 125.7 kJ/mol.

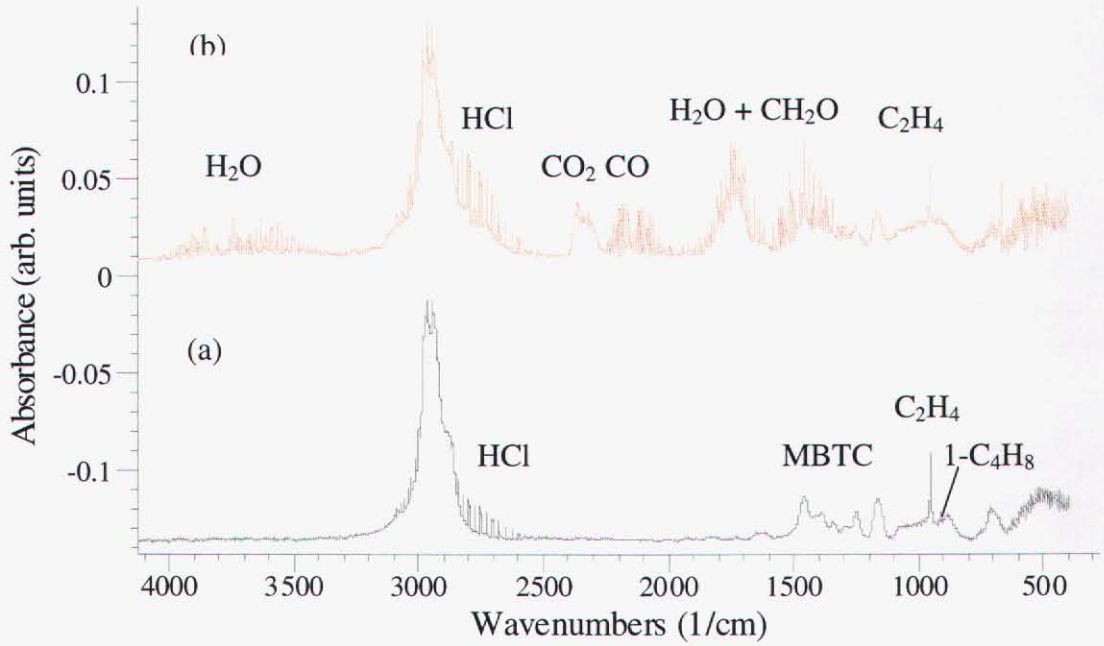

Figure 3-7. Typical FTIR spectra recorded during (a) pyrolysis of 0.23 mol/m^3 MBTC, and (b) reaction between 0.23 mol/m^3 MBTC and 3.15 mol/m^3 O_2. Other experimental conditions were T = 773 K and □ = 2 s.

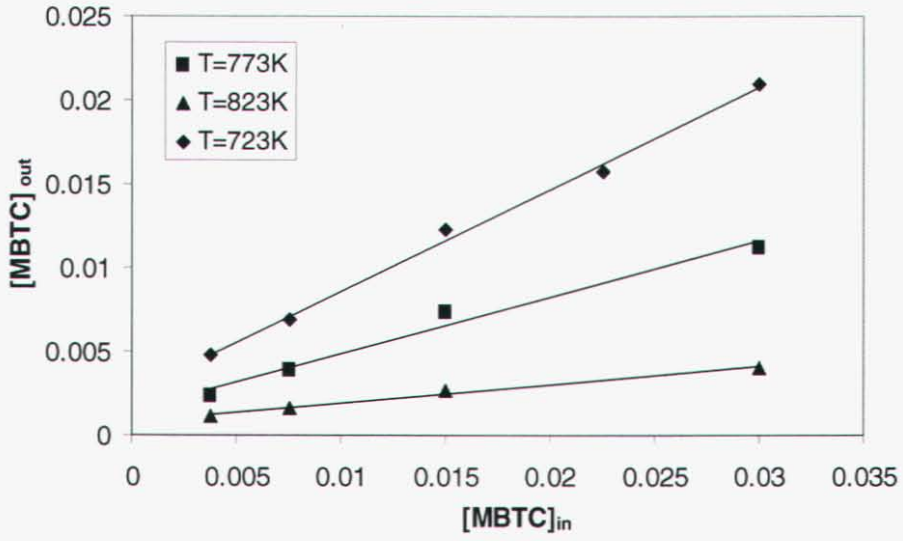

Figure 3-8. Variation of mole fraction MBTC as a function of inlet mole fraction MBTC and reactor temperature.

Decomposition is expected, based on predicted bond energies in MBTC, to be initiated by the cleavage of the Sn–C bond:

$$C_4H_9SnCl_3 \leftrightarrow SnCl_3 + C_4H_9 \qquad (3\text{-}51)$$

Similar initiation steps have been reported for dimethyltin dichloride [20] and tetramethyltin [21]. The Sn–C bond is about 289 kJ/mol. The considerable lower value found for the overall activation energy in the CSTR experiments, 126 kJ/mol, is probably caused primarily by subsequent radical attack of H or Cl on MBTC.

The presence of high concentrations of C_2H_4 and only minor concentrations of 1-C_4H_8 can be explained by the well-understood mechanism of C_4H_9 decomposition [22]:

$$C_4H_9 \leftrightarrow 1\text{-}C_4H_8 + H \qquad k(800\ K) = 2.66{\cdot}10 \text{ [5]} \qquad [52a]$$

$$C_4H_9\ (+M) \leftrightarrow C_2H_5 + C_2H_4\ (+M) \qquad k(800\ K) = 3.33{\cdot}10 \text{ [3]} \qquad [52b]$$

$$C_2H_5\ (+M) \leftrightarrow C_2H_4 + H\ (+M) \qquad [53]$$

The rate for 52b is two orders of magnitude higher than the rate for 52a, resulting in much higher concentrations of ethene with respect to 1-butene. Hydrogen chloride is most likely formed by abstraction of hydrogen by chlorine radicals:

$$SnCl_3\ (+M) \leftrightarrow SnCl_2 + Cl \qquad [54]$$

$$Cl + C_4H_9SnCl_3 \leftrightarrow C_4H_8SnCl_3 + HCl \qquad [55]$$

$$Cl + C_2H_5 \leftrightarrow C_2H_4 + HCl \qquad [56]$$

Reaction 54 yields gas-phase tin dichloride, which is found in the exhaust of the reactor. Tin dichloride has absorption features below the detection limits of the FTIR setup, but has a melting point of about 523

K and therefore condenses in the cold part of the exhaust system. Reaction 3-55 yields a butyltin trichloride radical, where the free electron is most likely located at a secondary carbon atom according to analogues in the hydrocarbon chemistry [23]. This means that 2-butene is formed on subsequent decomposition. However, this species could not be clearly identified with FTIR.

Figure 3-9 shows the formation of HCl and C_2H_4 as function of reactor temperature and inlet concentration MBTC. At 873 K and 923 K, the HCl concentration is constant, indicating that MBTC is completely decomposed. Reactions 3-51 and 3-54 through 3-56 indicate that the $MBTC_{in}/HCl_{out}$ mole fraction ratio should be 1.0 at high temperatures. However, a ratio of about 2:1 is found, indicating that not all of the $SnCl_3$ is converted into $SnCl_2$ (no chlorinated hydrocarbons were found). Note that we are also assuming that no HCl is lost to the walls in this analysis.

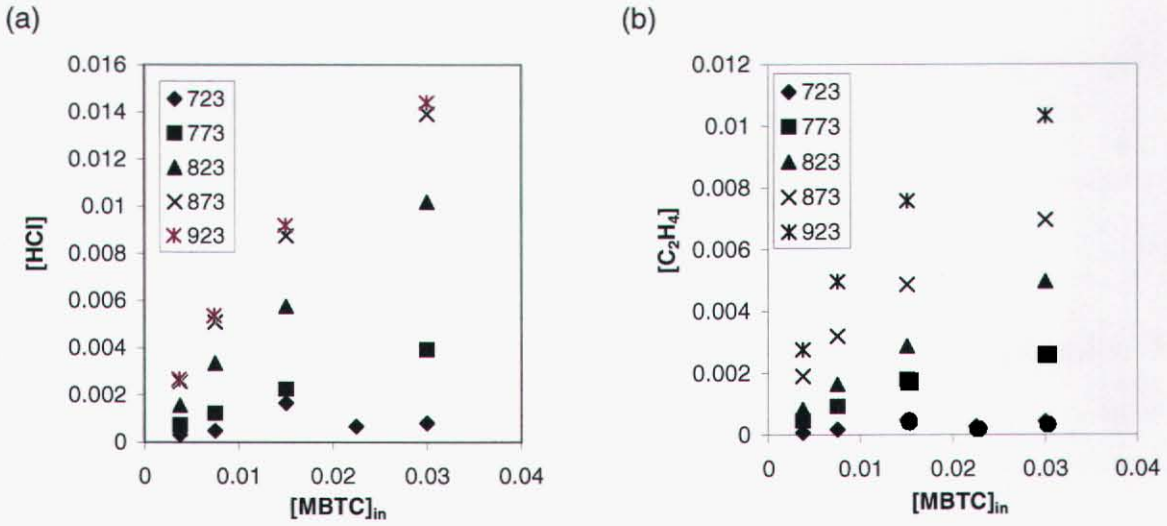

Figure 3-9. Mole fraction of (a) HCl and (b) C_2H_4 as a function of reactor temperature and inlet mole fraction MBTC.

3.4 References

1. R. J. Kee, F. M. Rupley, J. A. Miller, M. E. Coltrin, J. F. Grcar, E. Meeks, H. K. Moffat, A. E. Lutz, G. Dixon-Lewis, M. D. Smooke, J. Warnatz, G. H. Evans, R. S. Larson, R. E. Mitchell, L. R. Petzold, W. C. Reynolds, M. Caracotsios, W. E. Stewart, P. Glarborg, C. Wang, O. Adignun (2000). Reaction Design, Inc., San Diego, CA
2. A. M. B. Van Mol, G. R. Alcott, M. H. J. M. de Croon, C. I. M. A. Spee, J. C. Schouten (2000) In: M. D. Allendorf, M. L. Hitchman (eds) *Proc. Fifteenth Int. Symp. Chem. Vapor Dep.*, vol. 2000-13. The Electrochemical Society Proceedings Series, Pennington, NJ p 765
3. A. M. B. Van Mol, M. H. J. M. de Croon, C. I. M. A. Spee, J. C. Schouten (1999) *J. Phys. IV.* France 9: PR8
4. C. J. Giunta, D. A. Strickler, R. G. Gordon (1993) *J. Phys. Chem.* 97: 2275
5. S. J. W. Price, A. F. Trotman-Dickenson (1958) *Trans. Faraday Soc.* 54: 1630

6. J. A. M. Simoes, J. F. Liebman, S. W. Slayden (1995) S. Patai (ed) *The Chemistry of Organic Germanium, Tin, and Lead Compounds.* Wiley, New York p 245
7. H. Basch (1996) *Inorganica Chim. Acta.* 252: 265
8. M. D. Allendorf, C. F. Melius (1993) *J. Phys. Chem.* 97: 720
9. C. J. Pope, J. A. Miller (2000) *Proc. Combust. Inst.* 28: 1479
10. N. M. Marinov, W. J. Pitz, C. K. Westbrook, A. M. Vincitore, M. J. Castaldi, S. M. Senkan, C. F. Melius (1998) *Combust. Flame.* 114: 192
11. R. G. Gilbert, S. C. Smith (1990) *Theory of Unimolecular and Recombination Reactions.* Blackwell, Oxford
12. A. M. B. van Mol, M. D. Allendorf (2003) In: M. D. Allendorf, F. Maury, F. Teyssandier (eds) *16th Int. Symp. Chem. Vapor Dep./EUROCVD-14,* vol 2003-08. The Electrochemical Society Proceedings Series, Pennington p 65
13. V. D. Knyazev, I. A. Dubinsky, I. R. Slagle, D. Gutman (1994) *J. Phys. Chem.* 98: 5279
14. M. D. Allendorf, A. H. McDaniel, A. M. B. Van Mol (2002) In: C-P. Klages, H. J. Gläser, M. A. Aegerter (eds) *4th Int. Conf. Coatings on Glass, Braunschweig.* p 195
15. R. Walsh (1981) *Acc. Chem. Res.* 14: 246
16. R. David, D. Matras, *Can. J. Chem. Eng.*, **53,** 297 (1975).
17. P. Azay, M. Côme. *Ind. Eng. Chem. Process Des. Dev.*, **18,** 754 (1979).
18. A.M.B. Van Mol, H.T. Linden, C.I.M.A. Spee, M.H.J.M. de Croon, , J.C. Schouten, *Adv. Mat: CVD*, **7**, 101 (2001).
19. S.J.W. Price, A. F. Trotman-Dickenson,, *Trans. Faraday Soc.*, **54**, 1630 (1958).
20. R.P. Johnson, S.K.W. Price, *Can. J. Chem.*, **50**, 50 (1972).
21. V. Knyazev, I. Slagel, *J. Phys. Chem.*, **100**, 5318 (1996).
22. I. Galiba, J.M. Tedder, R.A. Watson, *J. Chem. Soc. A*, 1321 (1964).

This page intentionally left blank.

Chapter 4 Measurements of Tin Oxide Deposition Rates*

4.1 Introduction

The objective of the investigations described in this chapter is to provide data needed to develop robust models of SnO_2 CVD and use these data to understand the mechanisms controlling film growth. We report SnO_2 growth rates as a function of temperature, total pressure, flow rates, and concentration of MBTC and H_2O.

To accomplish this, we used a stagnation-flow reactor (SFR) based on a design developed by Tripathi et al.[1] The utility of an SFR for probing CVD mechanisms is well established.[2-4] With proper experimental design, reactions of the precursors with the reactor walls prior to the deposition surface can be excluded. Optical probing of the gases above the substrate is also possible, although this was not conducted here. From a modeling perspective, this geometry is very attractive, since stagnation flow can be transformed from two-dimensional fluid motion to one-dimensional by considering an unconfined infinite-radius disk.[2] This greatly simplifies the calculation and enables rapid testing of complex deposition mechanisms.

We also provide experimental and modeling results demonstrating that the flows within this new reactor are well behaved and can be modeled using a one-dimensional code such as SPIN (from the Surface CHEMKIN suite of codes)[5]. The results indicate that multiple reaction mechanisms are at work in the SnO_2 CVD from MBTC. Which mechanism dominates depends on the conditions of deposition, in particular, gas residence time, substrate temperature, water vapor concentration, and total pressure.

4.2 Experimental Methods

Figure 4-1 shows a schematic of the SFR. The reactor consists of a stainless-steel deposition chamber equipped with windows for observation and optical probing, electrical feedthrough ports for temperature measurement and heating power, and a controlled downstream butterfly valve with a mechanical pump that maintains the reactor pressure at 15–100 Torr. The reactor is oriented so that gases flow in a downward direction. The walls of the reactor are temperature-controlled using a recirculating high-temperature oil bath. Using mass flow controllers, reactants are delivered via heated transfer lines to the mixing chamber (located above the deposition chamber), whose wall temperature is also heated to prevent condensation of reactants. In these experiments, the reactor walls and mixing chamber were heated to 100 °C using a high-temperature polydimethylsiloxane fluid. After passing through the mixing chamber, gases enter the deposition chamber through a 7.6-cm-diameter copper showerhead containing 313 1.58-mm-diameter holes. The showerhead design was optimized using the analysis of Tripathi [6], which ensures uniform gas flow across the showerhead and convergence of individual gas jets prior to encountering the substrate. Copper was chosen for its high thermal conductivity, so that the showerhead can be maintained

* The text in this chapter was originally published in the following papers: (1) Y. Chae, A. H. McDaniel, W. G. Houf, M. D. Allendorf, "Stagnation-Flow Reactor Investigation of the Deposition of Tin Oxide from Monobutyltintrichloride," *J. Electrochem. Soc.*, 151 (2004), C527, and (2) Y. Chae, W. G. Houf, A. H. McDaniel, M. D. Allendorf, "Mechanisms for the Chemical Vapor Deposition of Tin Oxide from Monobutyltintrichloride," *J. Electrochem. Soc.*, 153 (2006), C309.

at a temperature near that of the mixing-chamber walls. The distance between the showerhead and the substrate surface is 3.8 cm.

Substrates (5.0-cm-diameter fused quartz used in these experiments) are heated by a silicon carbide (SiC) heater (Morgan Advanced Ceramics, Hudson, NH). Temperature control is achieved by a PID controller, using a type-K thermocouple placed on the back of the substrate. Substrate temperatures were calibrated as a function of the backside substrate temperature. To prevent deposition on the SiC heater top surface and eliminate temperature nonuniformities caused by the serpentine design of the heating element, a SiC transfer disk is placed between the heater and the substrate. To avoid deposition on the backside of the heater, a gas-purged quartz shroud was used (Figure 4-1).

MBTC and H_2O were delivered to the reactor by bubbling N_2 carrier gas through the liquid. MBTC with a purity of 99.83% was obtained from Atofina. The vapor pressure of MBTC [7] is only 0.064 Torr at 298 K, so the MBTC bubbler was heated to 353 K to increase it to 2.5 Torr, allowing MBTC concentrations in the range 0.05–0.5% to be obtained in the reactor. The actual delivery rate was calibrated by measuring the weight of MBTC delivered as a function of carrier gas flow rate; a delivery efficiency of 90% of the theoretically expected value was found. The H_2O bubbler was maintained at 278 K, allowing the inlet H_2O concentration to vary from 0 to 2.0 mol%. For all experiments an inlet O_2 concentration of 20 mol% was used.

For most experiments, a total pressure of 25 Torr and total flow rate of 5 slpm were used as the standard experimental condition to maintain a constant inlet velocity. However, both total flow rate and pressure were varied to determine the effect of these variables on the deposition rate. Total pressures varied from 15 to 100 Torr. The total flow rate varied from 2.5 to 10 slpm; N_2 was used to balance the flow rate.

To determine the film thickness, a narrow strip of the film was etched from the substrate using the Zn/HCl method reported by Szanyi [8]. The film thickness was then measured using a profilometer. Scanning electron microscopy (SEM) was used to observe the morphology of the fractured surface of the film, and X-ray diffraction (XRD) measurements were performed to establish film crystallinity.

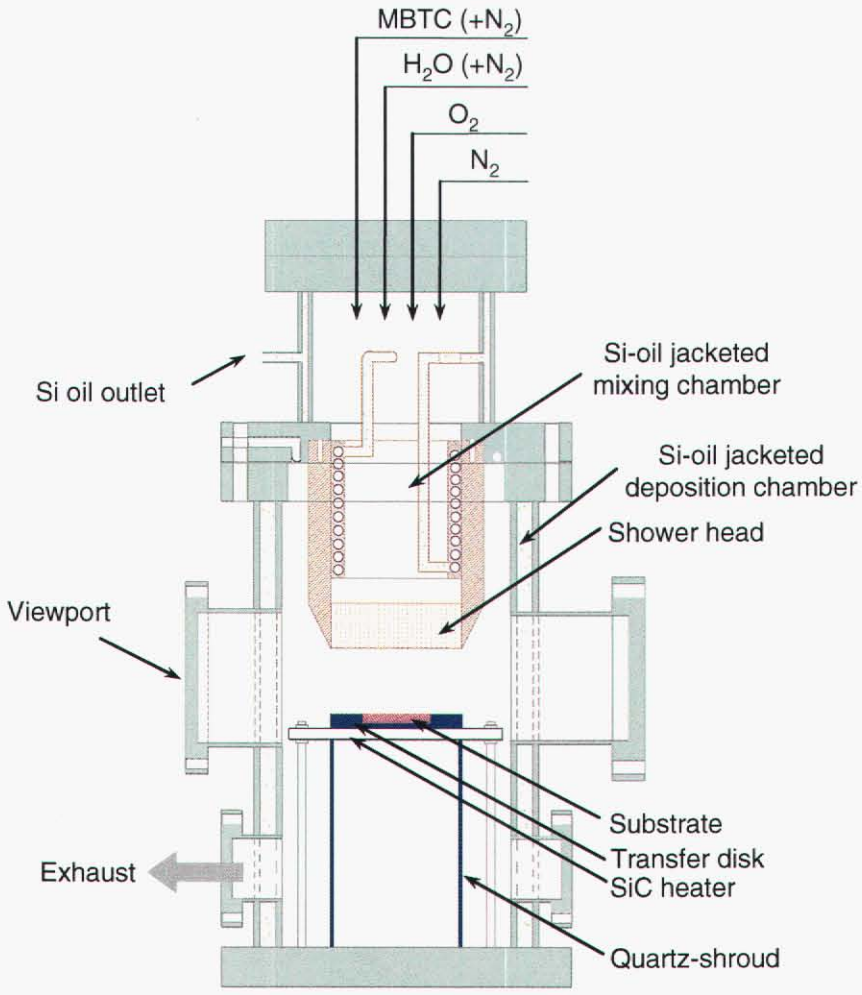

Figure 4-1. Schematic of the stagnation-point flow reactor used in all deposition experiments.

4.3 Results

4.3.1 Reactor Characterization

For the data obtained in this investigation to be useful for modeling investigations, it is essential to establish that the fluid dynamics and heat transfer within the reactor are well behaved. In particular, it is important that flows across the substrate be uniform and without recirculation zones, and that the temperature across the portion of the substrate used to determine deposition rates is constant. Consequently, we performed simulations of the reactor flow environment and experiments to confirm this, showing that one-dimensional stagnation-flow codes can be used to model this reactor.

Simulations of the flow and gas temperature profiles inside the SFR using the CURRENT model [8] (developed by Sandia National Laboratories) show that the gas flows within the reactor are well behaved. This model solves the Navier Stokes equations in two dimensions, using a staggered grid with the SIMPLER algorithm [9]. Figure 4-2 shows the streamlines (a) and temperature field (b) predicted for an inlet gas temperature of 392 K, substrate temperature of 853 K, total pressure of 25 Torr, and total nitrogen flow rate of 5.0 slpm. The substrate temperature profile used as input for CURRENT was obtained from measurements using a thermocouple (see below). As shown in Figure 4-2, the streamlines

and temperature profiles are well developed, while the absence of recirculation zones near the substrate indicates that buoyancy-driven forces are not important and that flows across the substrate are stable. As also can be seen in Figure 4-2, the thermal boundary layer extends approximately 1.8 cm above the substrate, with the region of gas temperatures >773 K (where gas-phase reactions might begin to occur) being only a few mm thick. In addition to these calculations, we assessed the validity of the one-dimensional approximation for this reactor using criteria defined by Houtman et al. [10] for stagnation flow. The results indicate that the one-dimensional approximation is valid over the central 60% of the substrate for the aspect ratio (inlet-substrate distance/substrate radius = 1 in this reactor) and Reynolds numbers (20–80) used in these experiments [10]. The stable flow conditions indicated by the CURRENT calculations coupled with the Houtman et al. analysis indicate that this reactor provides a favorable environment for obtaining reproducible SnO_2 deposition-rate data and for modeling it using one-dimensional stagnation-flow codes such as SPIN [5].

To demonstrate that these flow conditions result in uniform deposition rates across the substrate, we measured the film thickness across the substrate for deposition temperatures of 773 K and 853 K (0.1 mol% MBTC, 20 mol% O_2; all other conditions the same as in the CURRENT simulations), as shown in Figure 4-3. The thickness is essentially constant across the substrate at 773 K. In the central (~20-mm-diameter) region of uniform thickness, the variation in the growth rate is ±5.8% and ±3.8% at substrate temperatures of 773 K and 853 K, respectively, which is consistent with a measured substrate temperature variation of ±7 K. However, the thickness at 853 K has a gradient at the edge of the substrate caused by thermal losses at the edges. Thermocouple measurements show that temperature nonuniformities exist in the 0–12 mm and 32–50 mm regions at this temperature and the magnitude of these gradients increases with temperature. Thus, all growth-rate data were measured in the central region of uniform thickness.

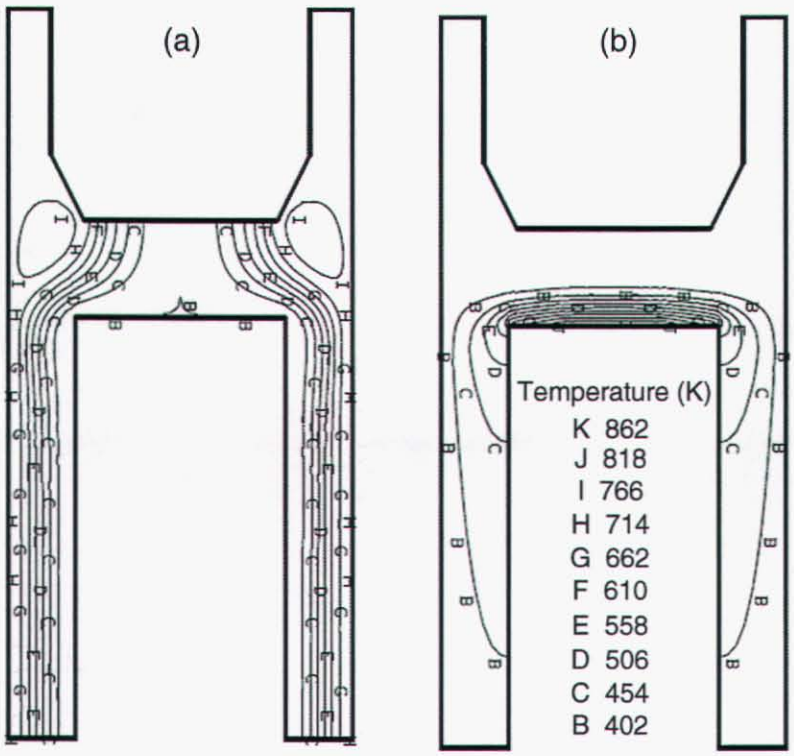

Figure 4-2. (a) Streamlines of N_2 flow and (b) the temperature field within the reactor predicted by the CURRENT program for a total pressure of 25.0 Torr, inlet velocity of 76 cm s^{-1} (5.0 slpm), substrate tem. of 853 K, wall temp of 373 K, and showerhead temp of 392 K.

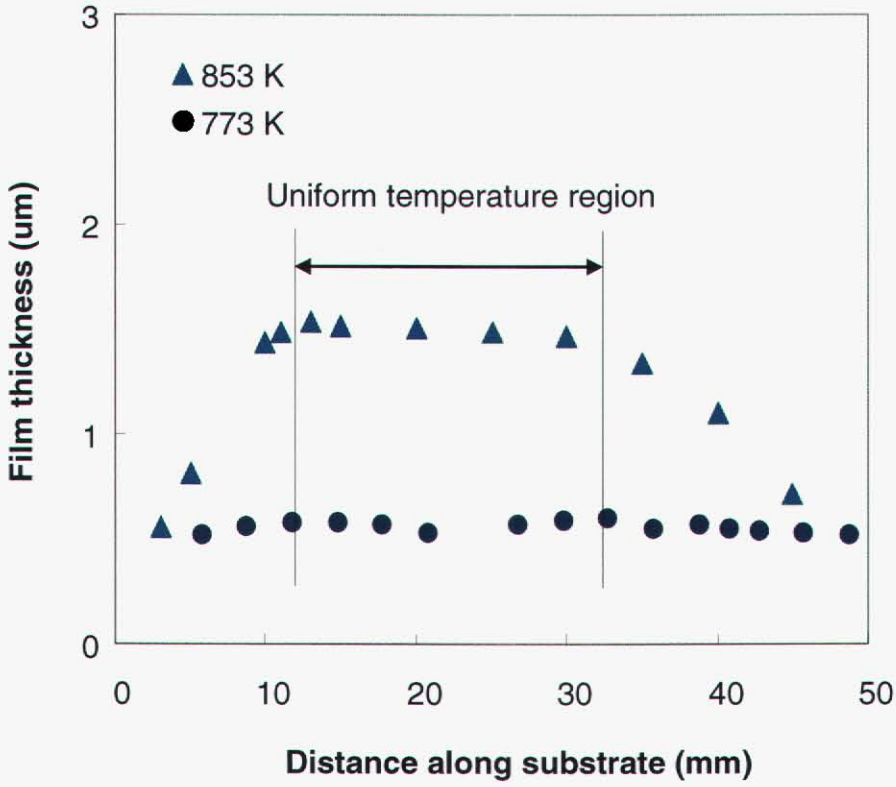

Figure 4-3. Uniformity of film thickness across the substrate. The experimental conditions were as follows: total pressure of 25.0 Torr, substrate temperature of 773 K and 853 K, 0.1 mol% MBTC, 20.0 mol% O_2. The slight shift (~ 3 mm) of the profile to the left of centerline is due to substrate placement with respect to the showerhead.

4.3.2 Film Composition and Morphology

Figure 4-4 shows SEM images of the films deposited by MBTC + O_2 (4a–c) and MBTC + O_2 + H_2O (4d–f) as a function of substrate temperature the thickness of the SnO_2 films is uniform and dense for MBTC + O_2 mixtures with and without H_2O. No pores were found at the SnO_2/SiO_2 interface, as seen in the cross-sectional view (inset of Figure 4-4f). For the films deposited from MBTC + O_2 mixtures, an increase in the substrate temperature from 573 K to 873 K causes an increase in the grain size of 40% (determined from the FWHM of the (110) XRD peak). Also, the surface morphology changes from small grains to large grains as the deposition temperature increases, but the grains have similar sharp edges regardless of temperature. For the films deposited by MBTC + O_2 + H_2O, the grain sizes and surface roughness (~40 Å) are the same regardless of temperature. However, the surface morphology changes with the temperature. At 573 K, the edges of the grains at the surface are rounded, but as the temperature increases, they become sharper.

XRD analysis from Figure 4-5 indicates that the films are polycrystalline and that the preferential orientation changes with both temperature and the addition of H_2O. The films deposited from MBTC + O_2 at 573 K have a preferred orientation of (200). However, with increasing temperature, the (110) peak gradually becomes larger. At 873 K, the (110) peak has the highest intensity, and the diffraction pattern is the same as that of SnO_2 powder, showing that no preferential orientations exist at this temperature. In contrast, the preferential orientation changes when H_2O is used in the reactant mixture. Films deposited by MBTC + O_2 + H_2O at 573 K have a preferred orientation of (211). Increasing the substrate temperature, however, causes the (110) peak to become the highest intensity peak for growth temperatures ≥673 K. This change in crystalline orientation may indicate a change in deposition mechanism with temperature and H_2O addition, but other factors could also be responsible, including temperature-dependent nucleation rates and surface diffusion.

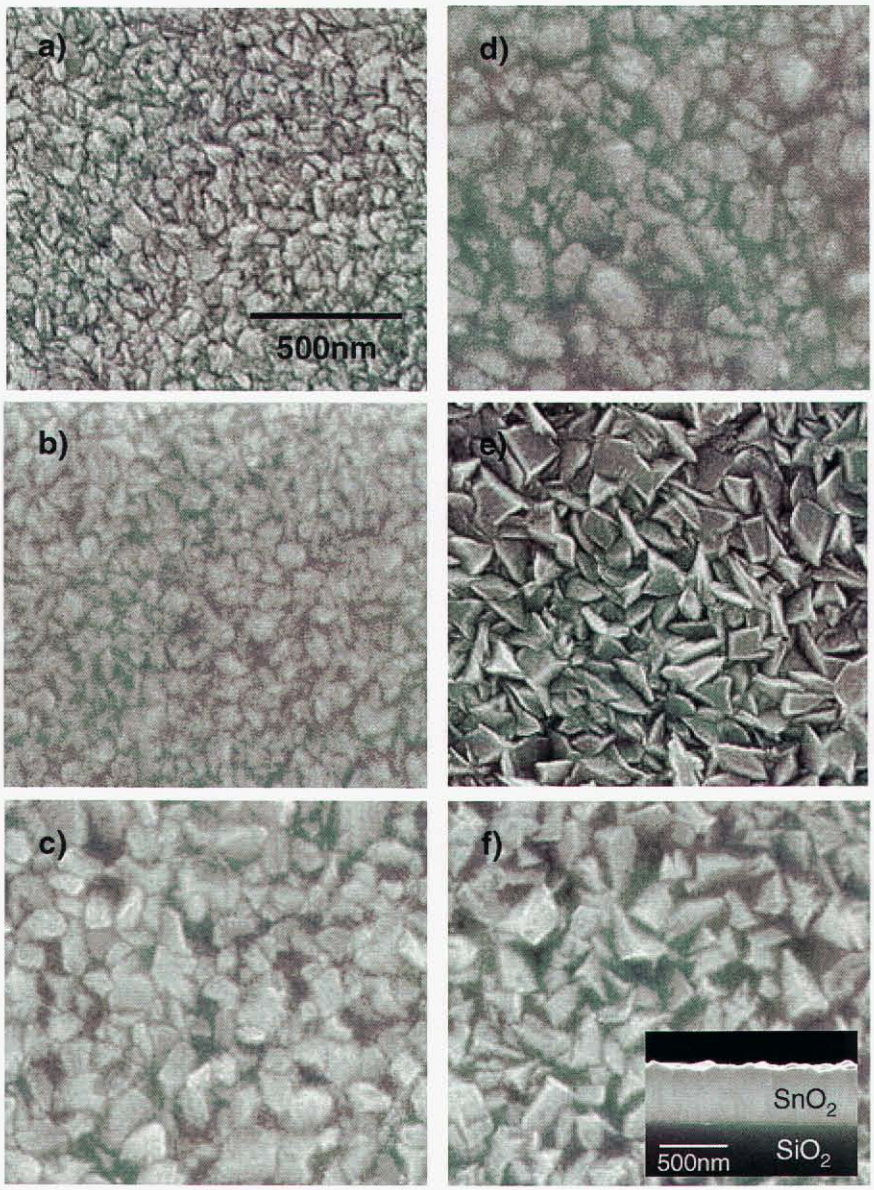

Figure 4-4. Surface morphology of SnO_2 films obtained from MBTC + O_2 (a-c) and MBTC + O_2 + H_2O (d-f) at a total pressure of 25.0 Torr, 0.1 mol% MBTC, 20.0 mol% O_2, and (for d - f) 0.4

mol% H_2O. (Deposition temperatures are as follows: a&d: 573 K; b&e: 673 K; c&f: 873 K. Inset of f) is a cross-sectional view of SnO_2 film deposited on SiO_2.

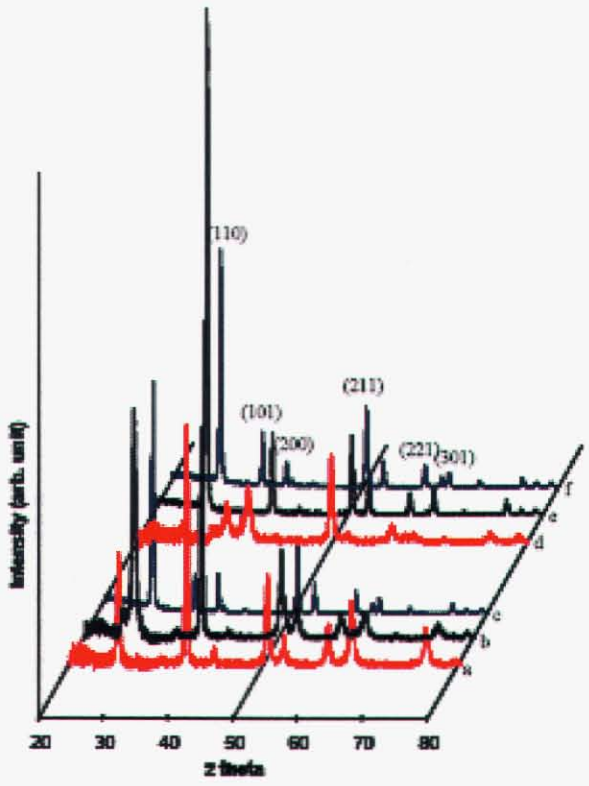

Figure 4-5. X-ray diffraction patterns of SnO_2 film by MBTC + O_2 (a-c) and MBTC + O_2 + H_2O (d-f) at total pressure of 25 Torr, 0.1 mol% MBTC and 20 mol% O_2. (a&d: 573 K, b&e: 673 K, and c&f: 873 K).

4.3.3 Deposition from MBTC + O_2

Prior to conducting extensive deposition measurements, we determined that the growth rate is independent of deposition time under the conditions of our experiments. Experiments were performed at the standard conditions (total pressure of 25 Torr, total flow rate of 5.0 slpm, and reactant concentrations of 0.1 mol% MBTC and 20 mol% O_2), using a substrate temperature of 823 K, for successively longer deposition times. The film thickness obtained in this manner is linearly proportional to the deposition time: 1.3-, 2.5-, and 5.4-μm thick at deposition times of 2.5, 5, and 10 min, respectively. This linear behavior indicates that there is no induction time prior to the establishment of steady-state growth.

The temperature dependence of the deposition rate does not correspond to a single activation energy, as shown in Figure 4-6. The Arrhenius plots of the growth rate, shown as a function of MBTC concentrations, exhibit a substantial change in activation energy at 673 K. In the low-temperature region (below 673 K), the activation energy determined from the slope of growth rate vs. $1/T$ ranges from 19.9 to

17.8 kcal/mol. In the high-temperature region above 673 K, the activation energy is much lower, ranging from 11.4 ± 1.1 kcal/mol. This activation energy is in good agreement with the values derived by Lee et al. (8 kcal/mol)[12] and van Mol (11.38 kcal/mol) from their experiments at 1 atm total pressure[7]. The observed change in activation energy suggests a change in the deposition mechanism. Since the value for the high-temperature region is large enough to exclude mass-transport-limited growth, for which the activation energy should be near zero, both growth mechanisms must represent chemical-kinetic processes.

The dependence of the growth rate on MBTC concentration can be extracted from the data in Figure 4-6. The reaction order thus obtained is sublinear over the temperature range of 723–923 K. Table 4-1 shows reaction orders obtained from the slope of the growth rate vs. MBTC concentration. Although there are minor variations in the MBTC reaction order as a function of temperature, the scatter in the data exhibited by the slope measured at 823 K indicates that the reaction order is essentially constant as a function of temperature and equal to 0.74 ± 0.09.

Table 4-1. Reaction order of MBTC for MBTC + O_2 reaction.

Temperature (K)	Reaction order
723	0.78
773	0.69
823	0.74 ± 0.09
873	0.85
923	0.83

We also examined the effect of total flow rate, which correlates roughly with the gas residence time. The growth rate at 823 K is found to be independent of this variable, as shown in Figure 4-7. To obtain the data displayed in this figure, the individual reactant flow rates were adjusted to increase the total flow rate, while maintaining constant total pressure and partial pressures of the reactants. Thus, reactant inlet concentrations did not vary, but the rate of mass transfer increased, and the residence time decreased. Since higher inlet velocities decrease the thermal boundary layer thickness, the residence time is reduced. Thus, the growth rate should decrease if a thermally activated gas-phase reaction produces the actual growth precursor. The lack of a dependence on flow thus suggests that either gas-phase reactions involved in the generation of precursor species are much faster than the reactions on the surface producing the deposit, or gas-phase chemistry is slow at 823 K relative to the gas residence time. In either case, deposition is rate-limited by a surface reaction. The lack of a flow-rate dependence also confirms that the variable activation energy is the result of a change in growth mechanism and not the result of growth conditions that are in a transition zone between mass-transport and surface-kinetic limitations. In the latter case, the growth rate should increase with decreasing boundary-layer thickness.

The effect of total pressure (P) was also examined, since our data must be extrapolated to atmospheric pressure for use in modeling industrial deposition processes. In addition, the functional dependence of the growth rate on pressure can be used to distinguish mass-transport from kinetically limited growth regimes (see the Discussion section). Deposition rates were measured as a function of P at 773, 823, and 923 K by adjusting the reactor pressure set point from 15 to 100 Torr, while maintaining constant partial pressures of MBTC and O_2 and total flow rate. The growth rates are plotted against P^{-1} in Figure 4-8, since it can be shown (see Discussion) that mass-transport-limited growth under these conditions is inversely proportional to total pressure with an intercept at $P^{-1} = 0$ (infinite pressure) of zero. The data in Figure 4-8 indicate that at 773–823 K, the pressure dependence is relatively weak, indicating that, as concluded

previously, growth is limited by surface kinetics. At 923 K, however, a strong linear dependence on P^{-1} is observed, suggesting that growth is approaching the mass-transport limit at this temperature. The non-zero intercept confirms, however, that temperatures >923 K are required to achieve fully mass-transport-limited growth.

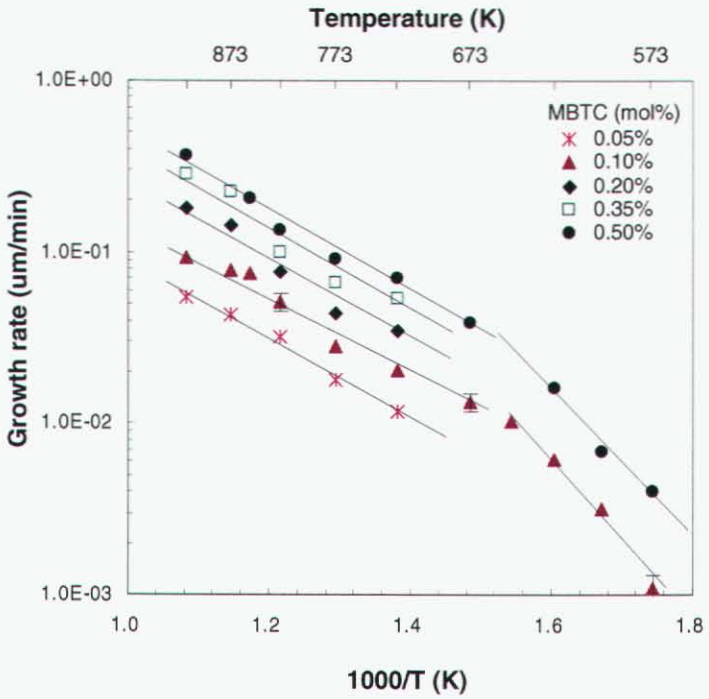

Figure 4-6. Temperature dependence of the SnO_2 growth rate obtained from various MBTC + O_2 mixtures at a total pressure of 25 Torr and 20.0 mol% O_2.

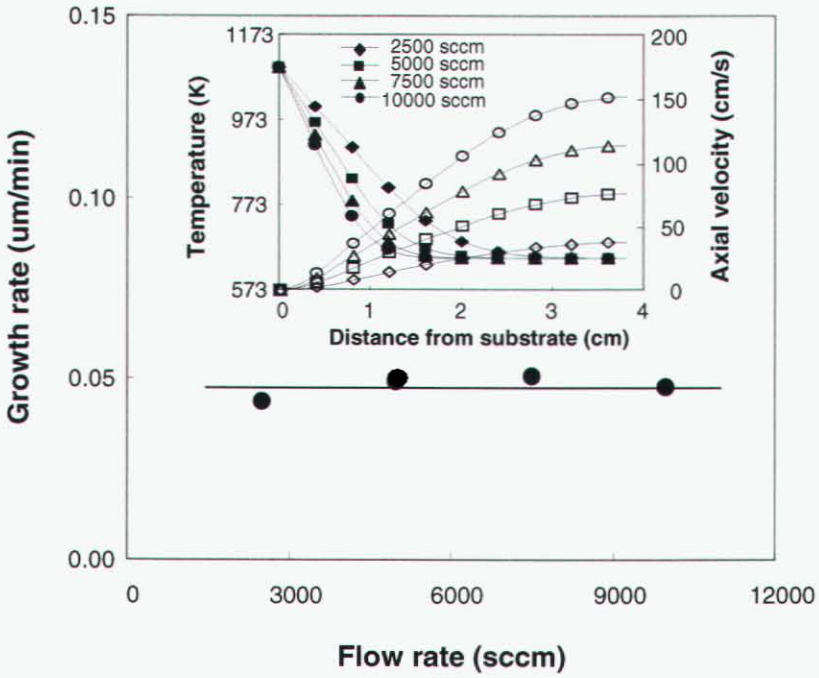

Figure 4-7. Influence of flow rate on growth rate. The partial pressures of MBTC and O_2 were 0.025 and 5.0 Torr, respectively. The total pressure and substrate temperature were 25.0 Torr and 823 K, respectively. Inset: temperature (closed symbols) and axial velocity (open symbols) profiles along the reactor centerline (0 cm and 3.8 cm are the positions of the substrate and showerhead, respectively) calculated using the CHEMKIN SPIN code17).

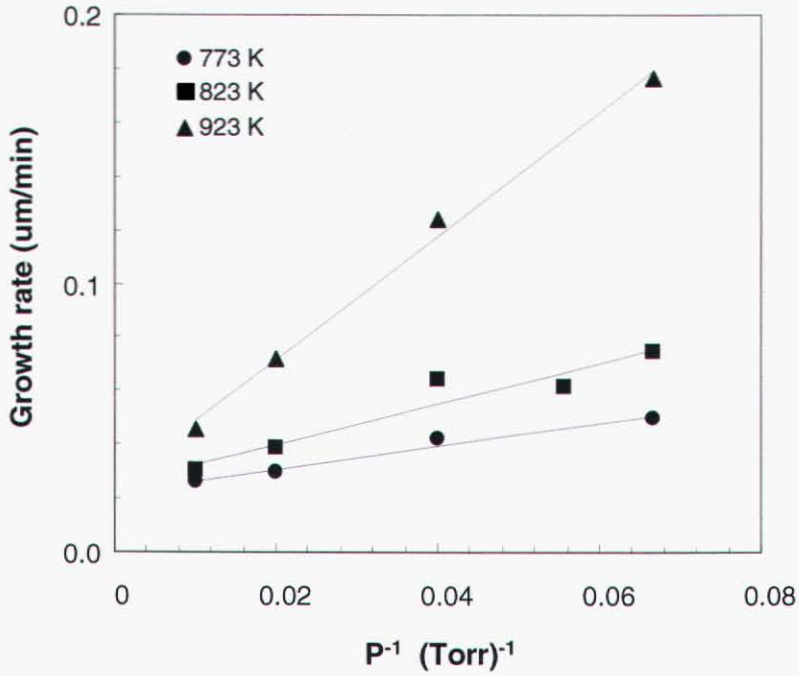

Figure 4-8. Influence of total pressure on growth rate. The partial pressures of MBTC and O_2 are 0.05 and 10.0 Torr, respectively.

4.3.4 Deposition from MBTC + O_2 + H_2O

The effect of H_2O on the growth rate was assessed by measuring SnO_2 growth rates as a function of inlet H_2O concentration with constant MBTC and O_2 concentrations. Results of these experiments are displayed in Figure 4-9, where the large increase of the growth rate caused by addition of 0.4 mol% water vapor to 0.1% MBTC/20% O_2 (line 2 in Figure 4-9) is clearly seen. Addition of H_2O increases the growth rate at all temperatures except 923 K compared with deposition without H_2O. This behavior is qualitatively the same as that observed by Lee et al. in a hot-wall tubular reactor at 1 atm.[7] The effect of water addition at temperatures below 673 K is much more remarkable than that at higher temperatures. For example, the increase in the growth rate at 673 K is 4.6 times higher than that at 873 K; at 573 K, the growth rate increases by a factor of 21. Corresponding changes in the activation energy are also observed. In the low-temperature region, the activation energy decreases from 19.8 to 8.5 kcal/mol when 0.4 mol% H_2O is added. On the other hand, the growth rate in the high-temperature region becomes almost independent of temperature, with an activation energy of only 1.2 kcal/mol. This low activation energy for $T > 673$ K suggests that the growth rate is limited by mass transfer. To confirm this, the MBTC concentration was varied from 0.2 to 0.4 mol% (line 4 in the figure). As expected, the growth rate is proportional to MBTC concentration, while the activation energy remains low (1.2–2.5 kcal/mol).

The SnO_2 growth rate also depends on the inlet H_2O concentration, as shown in Figure 4-10, although the magnitude of the effect depends on temperature. Data for substrate temperatures of 673 K and 873 K are

shown, using fixed MBTC and O_2 concentrations of 0.1 and 20 mol%, respectively. These data show that H_2O dramatically increases the growth rate at both temperatures, but only at low H_2O/MBTC ratios. The growth rate quickly saturates at 873 K, with an H_2O/MBTC ratio of 1.0 sufficient to produce the maximum growth rate. At 673 K, however, the approach to saturation is more gradual, requiring an H_2O/MBTC ratio of ~8 to reach the maximum growth rate.

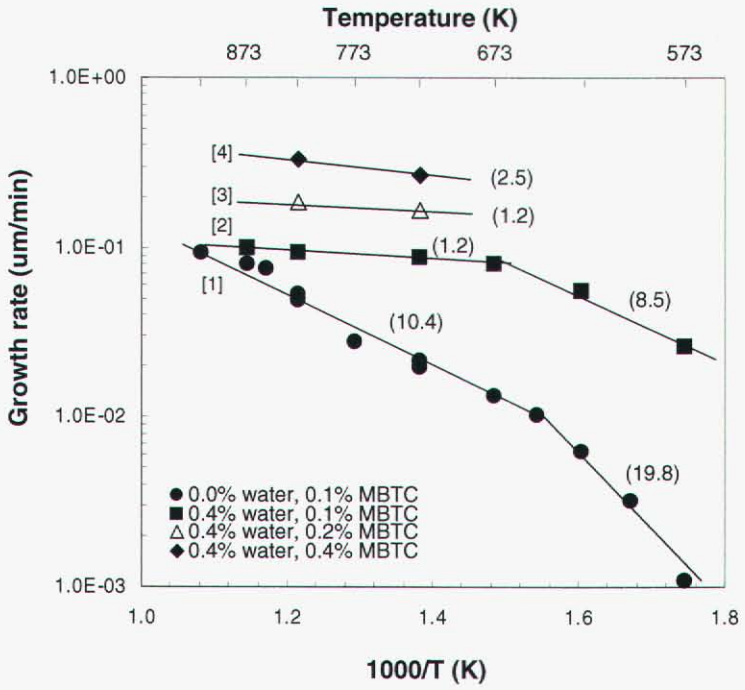

Figure 4-9. Comparison of growth rates obtained from MBTC + O_2 and MBTC + O_2 + H_2O mixtures at a total pressure of 25.0 Torr, total flowrate of 5.0 slpm, and 20.0 mol% O_2. The number in parenthesis represents the activation energy in kcal mol^{-1}.

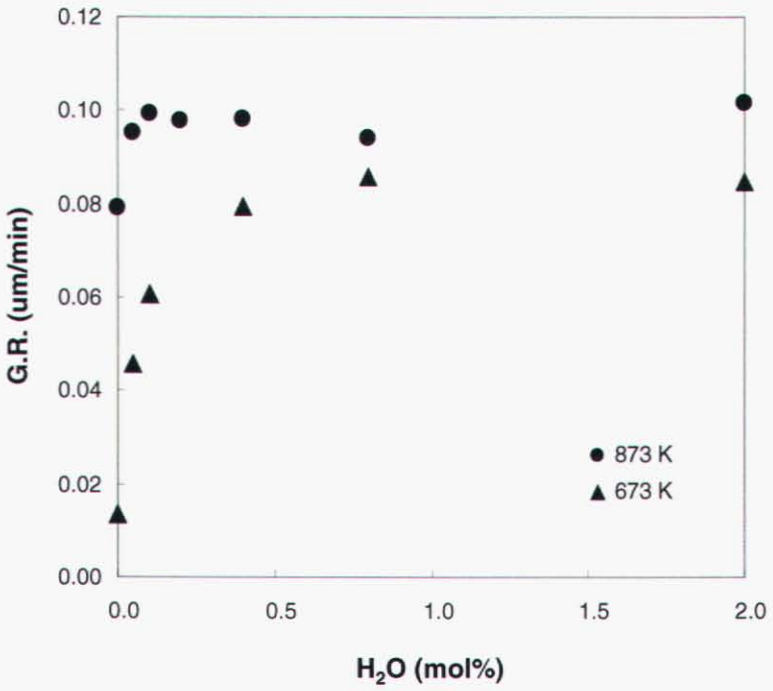

Figure 4-10. Effect of H_2O concentration on growth rate for MBTC + O_2 + H_2O reaction: total pressure of 25.0 Torr, and 0.1 mol% MBTC and 20.0 mol% O_2.

4.3.5 Effect of Gas Inlet Velocity

The effect on the growth rate of increasing the gas inlet velocity, which decreases the residence time of the gases between the inlet and the substrate, depends on temperature, as seen in Figure 4-11. Data obtained at substrate temperatures of 823 K published earlier [13] and new data reported here for 923 K are shown for an inlet mixture consisting of 0.1 mol% MBTC and 20 mol% O_2 in N_2 carrier gas at 25 Torr. At 823 K, the growth rate is constant regardless of the inlet velocity, indicating that growth is limited by the kinetics of a surface reaction. At 923 K (the highest temperature for which we have growth data), however, the growth rate increases 32% as the gas inlet velocity is increased by a factor of 4 from 38 cm/s to 152 cm/s. The increasing growth rates at 923 K suggest that growth is beginning to be limited by mass transport due to faster surface chemistry at this higher temperature. It is also possible, however, that gas-phase chemistry becomes sufficiently fast at 923 K that some of the MBTC undergoes pyrolysis and oxidation. Preliminary kinetic modeling suggests that the primary tin-containing products are $SnCl_x$ (x = 2–4) [14]. Tin oxide growth rates from $SnCl_2$ + O_2 and $SnCl_4$ + O_2 measured at 1 atm are both substantially slower than from MBTC + O_2 [15]. Thus, decreasing the time available for gas-phase reactions at 923 K may result in higher concentrations of the more reactive MBTC, thereby increasing the growth rate.

4.3.6 Effect of Inlet Oxygen Concentration

Experiments in which the inlet mole fraction of O_2 was varied indicate a strong dependence of the SnO_2 growth rate on the concentration of this reactant. As seen from the data (symbols) in Figure 4-12, growth rates increase steadily with O_2 mol% (ranging from 1 to nearly 100) at all temperatures examined. The reaction orders (obtained by linear regression) are 0.35, 0.32, and 0.37 at 598, 723, and 823 K, respectively. At 598 K, the growth rate appears to level off at the highest O_2 concentrations, but at higher temperatures, a steady increase is observed. Given the high concentrations, this steady increase is

somewhat surprising and suggests that O_2 is not very reactive with the surface, requiring high concentrations to saturate available adsorption sites.

4.3.7 Effect of Inlet MBTC Concentration

Results of a limited number of experiments in which the inlet MBTC concentration in an MBTC + O_2 + H_2O mixture was varied at 65 Torr suggest that total pressure affects the growth-rate dependence on this experimental parameter. The data were obtained at a substrate temperature of 823 K and are compared in Figure 4-13 with previously obtained data [13] at 25 Torr. The partial pressure of MBTC was increased to 0.62 Torr, which is the maximum we can generate at this pressure with our experimental facility. The partial pressures of O_2 and H_2O were maintained at 5 and 0.1 Torr, respectively. The results for two experiments indicate that at these high partial pressures, varying the MBTC concentration has little effect on the growth rate. This is in contrast with data obtained at 25 Torr and low MBTC concentrations, where a nearly linear dependence on MBTC concentration is observed. As is evident from Figure 4-13, which also shows the results of computational simulation discussed in the next chapter, it is possible to reproduce this effect using models derived from data obtained at 25 Torr.

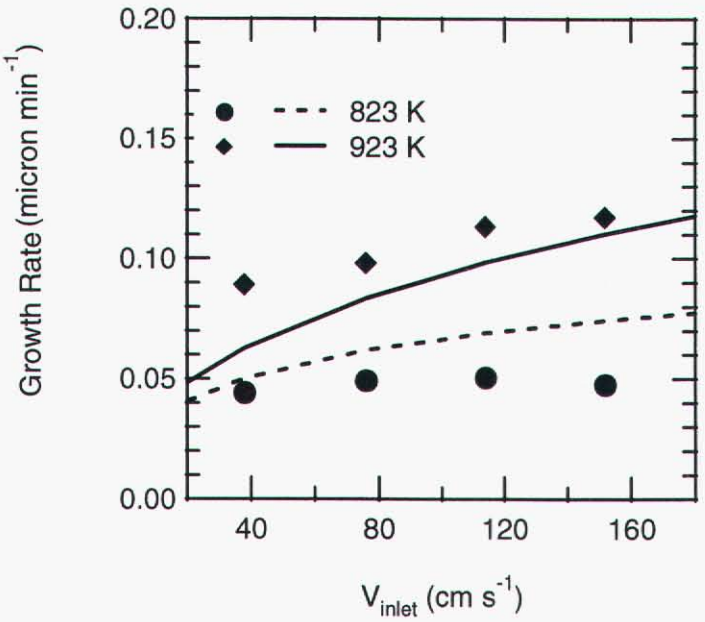

Figure 4-11. Effect of gas inlet velocity (V_{inlet}) on growth rate. Growth rates were obtained from 0.1 mol % MBTC + 20 mol % O_2 mixtures at substrate temperatures of 823 and 923 K and a total pressure of 25 Torr (symbols). Curves are growth rates simulated using model 1B.

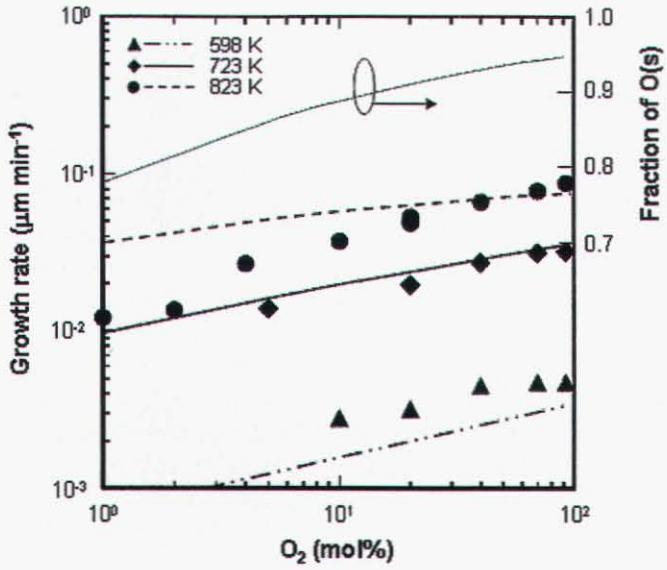

Figure 4-12. Effect of oxygen on the growth rate as a function of temperature for 0.1 mol % MBTC + O_2. The three bottom curves show the growth rates simulated by model 1B. The top solid curve is the fraction of sites occupied by adsorbed oxygen atoms (O(s)) at 723 K. The total pressure is 25 Torr. The sticking coefficient of O_2 ($\gamma(O_2)$) used for all simulations shown in 10^{-4}.

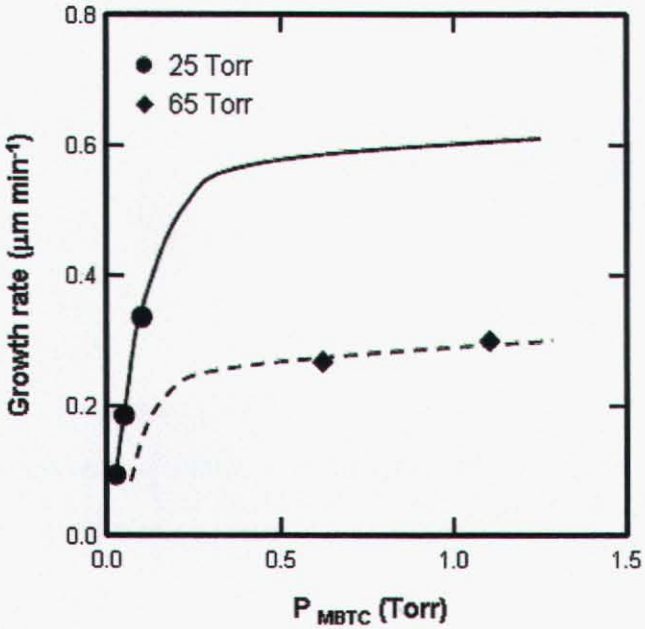

Figure 4-13. Comparison of growth rates at total pressures of 25 and 65 Torr for MBTC + O_2 + H_2O at 823 K. Curves are the growth rate obtained from model 2D. The simulation conditions are 20 mol % (5 Torr) O_2 + 0.4 mol% (0.1 Torr) H_2O for 25 Torr, and 7.7 mol % (5 Torr) O_2 + 0.15 mol% H_2O (0.1 Torr) for 65 Torr.

4.4 Measurements of SnO_2 Deposition from MBTC + O_2/H_2O at 1 atm

Deposition of SnO_2 from MBTC and O_2 begins below 673 K. Since these temperatures are well below the lower temperature limit for MBTC pyrolysis (723 K) and we have no evidence for a direct reaction in the gas phase between MBTC and O_2, this result indicates that MBTC and O_2 can react with the surface to form SnO_2 in the absence of gas-phase reactions. A typical FTIR spectrum of the gas phase during the deposition process is shown in Figure 3-7. Addition of oxygen to MBTC yields (besides HCl and C_2H_4, which are also found during pyrolysis of MTBC) water and oxidized carbon species such as CO, CO_2, and CH_2O. H_2O, and HCl are formed in about equal amounts, while the concentrations of CO_2, and CH_2O are an order of magnitude lower.

Deposition from MBTC, O_2, and H_2O starts even below 350 °C. Monitoring the composition of the gas phase with FTIR proved to be difficult, because of the strong IR-absorption of water. Figure 4-14 shows the deposition rate measured by suspending a substrate in the reactor for deposition from MBTC and oxygen with and without water.

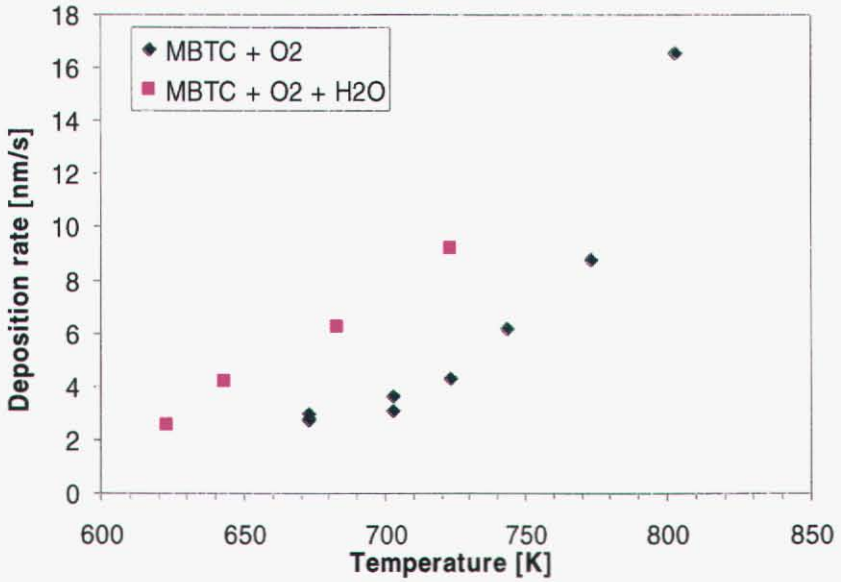

Figure 4-14. Deposition rate of tin oxide as function of reactor temperature. The concentration of MBTC was 0.26 mol/m^3; O_2: 3.4 mol/m^3; and H_2O: 0.34 mol/m^3.

The growth rate increases by a factor of 2 when water is added to the precursor mixture at 673 K. Assuming the rate limiting step for deposition of SnO_2 occurs in the gas-phase, the overall activation energy for MBTC + O_2 + H_2O (fitted from 623–723 K) is about 52 kJ/mol. This value was obtained by assuming a rate-limiting step in the gas phase with a first-order dependence on MBTC, taking into account the surface-to-volume ratio of the CSTR. The discrepancy between this activation energy and the activation energy obtained from decomposition (125.7 kJ/mol) is quite large and suggests that either surface reactions influence the overall deposition rate [16] or that a fast reaction between unreacted MBTC and H_2O occurs.

Similar to pyrolysis of MBTC, we expect that the reaction mechanism between MBTC and O_2 is initiated by bond breaking of Sn–C in MBTC, shown in Reaction 3-28 (Section 3.3.2) The *n*-butyl radical follows the well-known hydrocarbon oxidation chemistry, yielding H_2O, C_2H_4, CO, CO_2, and CH_2O [17]. Ab

initio calculations show that tin-containing products of MBTC pyrolysis, $SnCl_2$ and $SnCl_3$, can react with O_2 to form, respectively, Cl_3SnOO and $-O(SnCl_2)O-$ (cyclic) [16]. Subsequent reactions can eventually lead to the formation of $SnCl_3OH$; for example:

$$Cl_3SnOO + H \leftrightarrow Cl_3SnO + OH \quad (4\text{-}1)$$

$$SnCl_3O + RH \leftrightarrow SnCl_3OH + R \ (RH = MBTC, HCl, \text{or } H_2O) \quad (4\text{-}2)$$

Equilibrium calculations [16] suggest that Cl_3SnOH is the likely film precursor. Complete conversion to tin oxide most likely occurs via reactions on the surface.

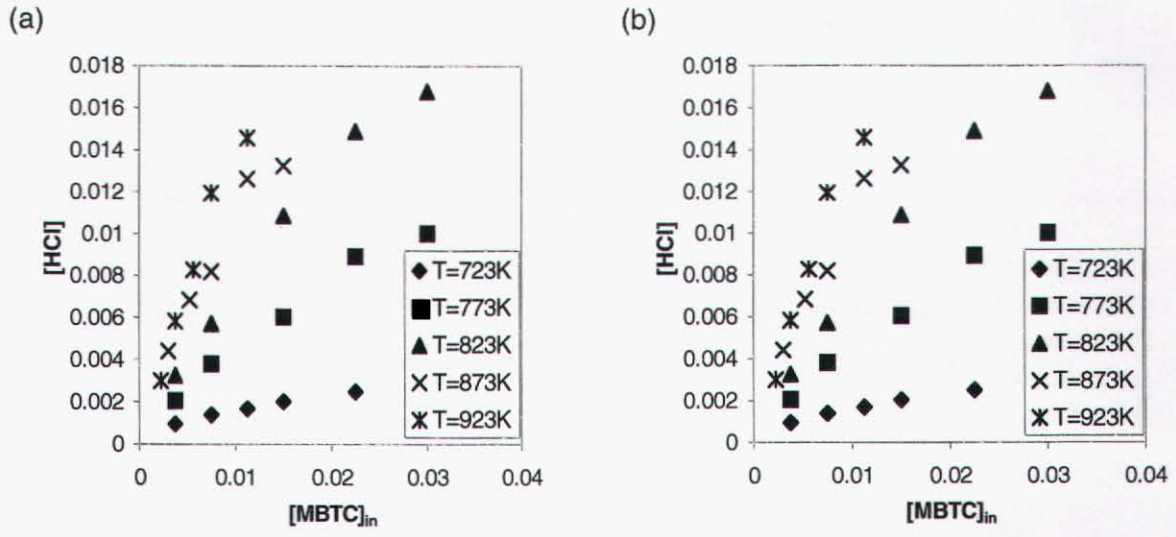

Figure 4-15. Formation of HCl (a) and C_2H_4 (b) as a function of reactor temperature and inlet mole fraction MBTC during deposition of tin oxide from MBTC and 20 mole% O_2.

Figure 4-15 shows the formation of HCl and C_2H_4 as a function of mole fraction $MBTC_{in}$ and reactor temperature. The formation of gas-phase intermediates like $SnCl_2$ and $SnCl_3$ is supported by the fact that not only the tin oxide growth rate, but also HCl formation, increases with reactor temperatures above 823K, while the conversion of MBTC is already complete at 823 K. The formation of C_2H_4 decreases with temperature above 873K. The reaction order for CO formation is greater than 1.0 above 873 K, implying that C_2H_4 is being oxidized at these higher temperatures.

The role of water is more difficult to interpret from these CSTR experiments. The hydrolysis experiments showed that adding water enhances the growth rate of tin oxide. During the oxidation process also water is formed. Ab initio calculations show that water exothermically reacts with $SnCl_2$ or $SnCl_3$ to form, respectively, $SnCl_2(OH_2)_x$ and $SnCl_3(OH_2)_x$ with $x = 1, 2$ [16]. Subsequent reactions with the radical pool (H, OH, Cl) lead again to Cl_3SnOH. However, modeling of the CSTR using the Aurora code [18] shows that even if the reaction rates between $SnCl_x$ and H_2O are set at the gas-kinetic limit, this does not lead to significantly higher conversion rates for MBTC. This results from the fact that water neither reacts directly with MBTC nor does it affect substantially the concentration of Cl atoms that react with MBTC. Thus, the role of water may be to form OH groups on the surface that can react with gas-phase MBTC, causing it to decompose heterogeneously.

4.5 Discussion

The results described in this chapter suggest that tin oxide deposition from MBTC is a complex process in which several different mechanisms contribute to growth. Which one is rate-controlling depends on the composition of the reactant mixture, the deposition temperature, and the pressure. We now examine these results in more detail, making use of previous investigations of this chemistry in our laboratories concerning the extent of gas-phase chemistry in this system. A more detailed analysis of the effects of total flow rate and total pressure is also provided, which allows mass-transport regimes to be more clearly identified. The results allow conclusions to be drawn concerning the relative importance of gas-phase chemistry, surface reaction, and mass transport. These conclusions provide the basis for developing a detailed chemical reaction mechanism, a subject that will be addressed in Chapter 5.

4.5.1 Deposition from MBTC + O_2

For SnO_2 deposition from MBTC + O_2 mixtures, the change in the activation energy at 673 K appears to be caused by a transition from one growth mechanism to another, based on the magnitude of the change and the relatively large activation energies. As discussed in the introduction, both gas-phase and surface chemistry can occur in CVD processes involving MBTC. However, measurements of MBTC pyrolysis rates in a CSTR indicate that at temperatures ≤723 K, gas-phase decomposition of MBTC does not occur[7]. In those experiments, the gas residence time (2 s) was considerably longer than typical residence times in the SFR experiments discussed here (~0.1 s). Gas-phase pyrolysis of MBTC can therefore be ruled out in our experiments at temperatures ≤723 K. Since we also do not expect MBTC itself to react with O_2 at any temperature typical of CVD [19], the tin oxide growth observed in these experiments at temperatures ≤723 K must be entirely heterogeneous, involving the reaction of unreacted MBTC and O_2 with the surface. The transition between growth mechanisms indicated by the change in activation energy at 673 K must therefore correspond to a change in a rate-limiting step in the surface chemistry. The chemical nature of these mechanisms cannot be discerned from these experiments. While there are numerous possibilities, including surface coverage effects, temperature-dependent sticking coefficients, and site blocking, detailed knowledge from, for example, experiments in ultrahigh vacuum is required to do more than speculate about the actual rate-controlling step in the process.

The extent of gas-phase MBTC decomposition at temperatures >723 K is unclear, although the evidence indicates that surface processes, not gas-phase reactions, continue to limit the deposition rate. The lack of a dependence on total flow rate Q_{tot} (Figure 4-16) is important evidence in this regard. By increasing the flow rate, the mass-transfer rate is increased (thereby increasing the Reynolds number, defined as $lu\rho/\mu$, where l is the distance between the showerhead and substrate, u is the inlet velocity, ρ is the mixture density, and μ is the viscosity at the inlet), and the residence time and thermal boundary-layer thickness decrease. This effect is illustrated by the inset of Figure 4-16, which shows calculated profiles of gas-phase temperature and axial velocity obtained from the CHEMKIN SPIN program [5] for a range of Q_{tot} and a substrate temperature of 823 K. In the figure, the showerhead is located at 3.8 cm and substrate at 0 cm. The gas residence time can be estimated by dividing the thermal boundary thickness by the average axial velocity. Both increasing inlet gas velocity and thinner boundary layers at higher flow rate contribute to shorter residence times. The inset plot shows that, for Q_{tot} of 2,500 sccm, the thermal boundary thickness (~3.0 cm) is double the thickness at 10,000 sccm. Increasing the residence time within the thermal boundary layer should increase the extent of MBTC pyrolysis and oxidation. Thus, if a gas-phase reaction producing the SnO_2 precursor is the rate-controlling step, the growth rate should increase as flow rate decreases. However, growth rates are constant as a function of Q_{tot} and are sensitive only to the substrate temperature, again demonstrating that a surface reaction is the rate-controlling step.

It should be noted, however, that even small amounts of gas-phase MBTC decomposition might lead to tin-containing species whose surface reactivity is considerably greater than that of MBTC. In the high-temperature region (above 673 K), the CSTR experiments mentioned earlier indicate that MBTC can decompose by gas-phase reactions if sufficient residence time is available, yielding $SnCl_2$, C_2H_4, and HCl by a mechanism including both unimolecular MBTC decomposition and radical-chain processes involving H and Cl atoms[7]. Although the extent of MBTC decomposition must be much smaller in our experiments than in the CSTR due to the much shorter gas residence times (~0.1 s vs. 2.0 s), small amounts of MBTC decomposition and/or oxidation products might be produced. Gas-phase radicals are typically expected to have much higher sticking coefficients than their unreacted precursors (unit sticking coefficients are often assumed for radicals in modeling CVD processes). Therefore, a gas-phase contribution to deposition cannot be ruled out completely. A detailed modeling analysis of the gas-phase processes is required to obtain a more quantitative estimate of the contribution of this chemistry to film growth.

The effect of total pressure P on the growth rate is important to characterize, since it not only provides insight into how the data obtained here can be extended to higher pressures, but also the extent to which mass-transport limitations exist. To understand the effect, the functional dependence on pressure of the diffusion mass flux of MBTC (J_{MBTC}) to the surface must be characterized. If we consider a mass-transfer boundary layer with thickness d above the substrate, J_{MBTC} can be expressed as follows for the binary system of MBTC and N_2:

$$J_{MBTC} = -\rho D (\Delta y_{MBTC} / d) = -\rho D (M_{MBTC} / M_{mix})(\Delta x_{MBTC} / d) \quad (4\text{-}3)$$

(assuming M_{mix} is constant) where ρ is mixture density, M_{MBTC} is the molecular weight of species MBTC, D is the diffusivity of MBTC in N_2, and Δx_{MBTC} and Δy_{MBTC} are the difference in the MBTC mole fraction and mass fraction between the surface at $z = 0$ and the top of the boundary layer at $z = d$, respectively.

Because the Reynolds number was constant in the experiments (i.e., constant mass flow rate), the boundary layer thickness d did not change with total pressure. The density ρ is proportional to P, while the diffusivity D is proportional to P^{-1}, so ρD is independent of pressure. Thus, the only pressure effect remaining in J_{MBTC} is that contained in Δx_{MBTC} ($= P_{MBTC} / P$), which is proportional to P^{-1}(P_{MBTC} was constant). Therefore, if mass transfer limits the deposition process, J_{MBTC}, and therefore the growth rate, should be proportional to P^{-1}. However, if a surface reaction limits the process, the rate should be independent of J_{MBTC} and therefore of P; growth is then a function of surface temperature only. In this analysis, the nonzero intercept at P^{-1}(i.e., at infinite pressure) indicates that surface kinetics still contribute to the observed rate, since the growth rate should go to zero at $P^{-1} = 0$ if the process is mass-transport limited.

Using this analysis, two observations can be made from Figure 4-17. First, the growth rate is nearly independent of P^{-1}at 773 K, but the slope increases as temperature increases, suggesting an approach to the mass-transport limit. When the growth rates are plotted against $T^{-1}$the activation energies at 15, 25, 50, and 100 Torr are 12.1, 10.2, 8.4, and 5.4 kcal/mol, respectively. The decrease in activation energy with increasing pressure is consistent with a trend toward mass-transport-limited growth: since J_{MBTC} is proportional to P^{-1}, higher pressures lead to reduced mass flux rates, decreasing mass transport to the point that it eventually is slower than the surface kinetics. Second, however, the lines for all three temperatures extrapolate to nonzero intercepts at $P^{-1} = 0$, indicating that even in the limit of infinite pressure at these temperatures, growth can still occur due to slow surface chemistry. Thus, deposition is not mass-transport limited at any of the temperatures examined. Extrapolation of these results to 1 atm and the temperatures (>873 K) typical of on-line deposition suggests that tin oxide growth from MBTC + O_2 will be mass-transport limited under these conditions. Note, however, that this assumes that residence times are sufficiently short that no gas-phase chemistry occurs.

4.5.2 Deposition from MBTC + O_2 + H_2O

Addition of H_2O has a major impact on the growth process, lowering the activation energy and changing the rate-controlling step from a combination of surface reaction and mass transfer to purely mass-transport limited growth, as shown by the very low activation energies at $T \geq 673$ K in Figure 4-16. In addition, growth rates are proportional to the MBTC concentration at these temperatures. These facts indicate that the transport of MBTC itself to the surface or of intermediates produced by rapid MBTC reaction in the gas phase is rate-controlling.

Two possibilities may be considered to explain the change of the rate-controlling step and the saturation effect of the growth rate by adding water vapor (Figure 4-17). One explanation is that H_2O facilitates the surface reaction by making hydroxyl groups available on the surface. This increases the reactivity of the surface, such that surface chemistry is no longer the rate-limiting step. If true, these groups must be extremely reactive, since small amounts of water cause very large increases in growth rate at low surface temperatures (Figure 4-16). In this mechanism, the saturation of the growth rate with the water vapor partial pressure is caused by a saturation of the surface with hydroxyl groups, so that excess amounts of H_2O no longer increase the surface coverage. The formation of these hydroxyl groups must be thermally activated, since the approach to saturation is slower at 673 K than at 873 K. The existence of hydroxyl groups on tin oxide surfaces has been confirmed at 673 K by x-ray photoelectron spectroscopy [20] and their involvement in the oxidation of tetramethyltin [21] and in the dissociative adsorption of H_2O on SnO_2 surfaces [22] has already been proposed. In a related CVD system, Matero et al. report that Al_2O_3 atomic layer deposition growth rates can be increased by exposing the surface to H_2O, a result that is attributed to an increase in the surface hydroxyl concentration [23].

Another explanation that must be considered is the formation of a reactive Sn–H_2O complex by a gas-phase reaction. Such a complex could be formed in two ways: (1) products of MBTC decomposition, $SnCl_2$ and $SnCl_3$, react with gaseous H_2O to yield Sn–O–H products (Cl_3SnOH), as suggested previously, [19] or (2) MBTC reacts directly with H_2O and forms a complex[24]. The energetics of the first pathway were predicted by ab initio calculations [19]. The results indicate that several exothermic pathways exist by which the complexes Cl_2SnOH_2 and Cl_3SnOH_2 can react to produce Cl_3SnOH, which equilibrium calculations predict is the thermodynamically most stable tin-containing species under typical growth conditions[19,24]. Ab initio calculations also predict that forming complex between the MBTC analogue CH_3SnCl_3 and two water molecules is exothermic, suggesting that similar chemistry could occur with MBTC. Since this reaction would almost certainly have much lower activation energy than that required for the first mechanism to occur (which requires breaking the Sn–C bond in MBTC at 69 kcal/mol), MBTC hydrolysis could occur at much lower temperatures. This is consistent with the observed growth rate behavior: mass-transport-limited growth at temperatures as low as 673 K, which are too low to pyrolyze MBTC, requiring that any gas-phase chemistry leading to formation of a precursor be very fast relative to its transport to the surface. Thus, the second mechanism seems to be the more likely of the two.

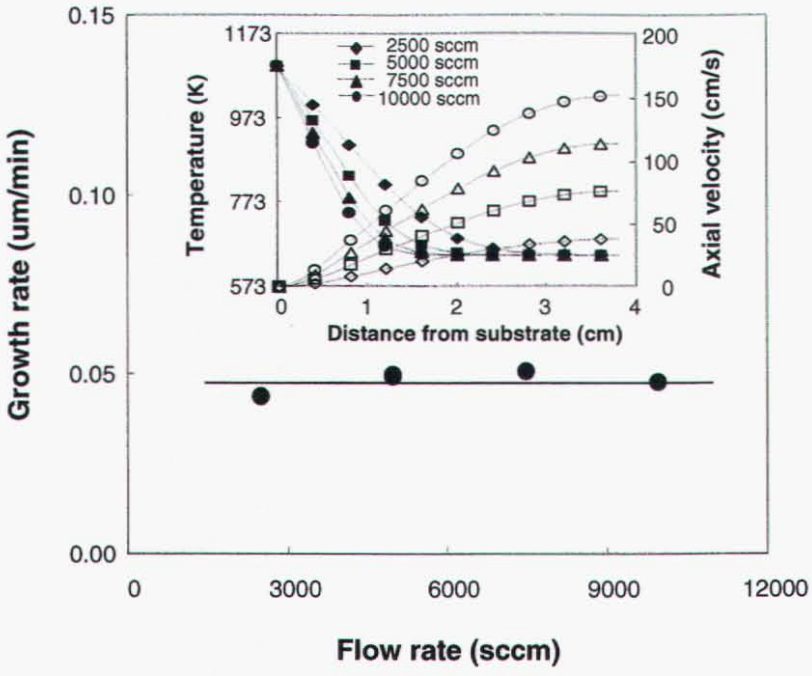

Figure 4-16. Influence of flow rate on growth rate. The partial pressures of MBTC and O_2 were 0.025 and 5.0 Torr, respectively. The total pressure and substrate temperature were 25.0 Torr and 823 K, respectively. Inset: temperature (closed symbols) and axial velocity (open symbols) profiles along the reactor centerline (0 cm and 3.8 cm are the positions of the substrate and showerhead, respectively) calculated using the CHEMKIN SPIN code [5].

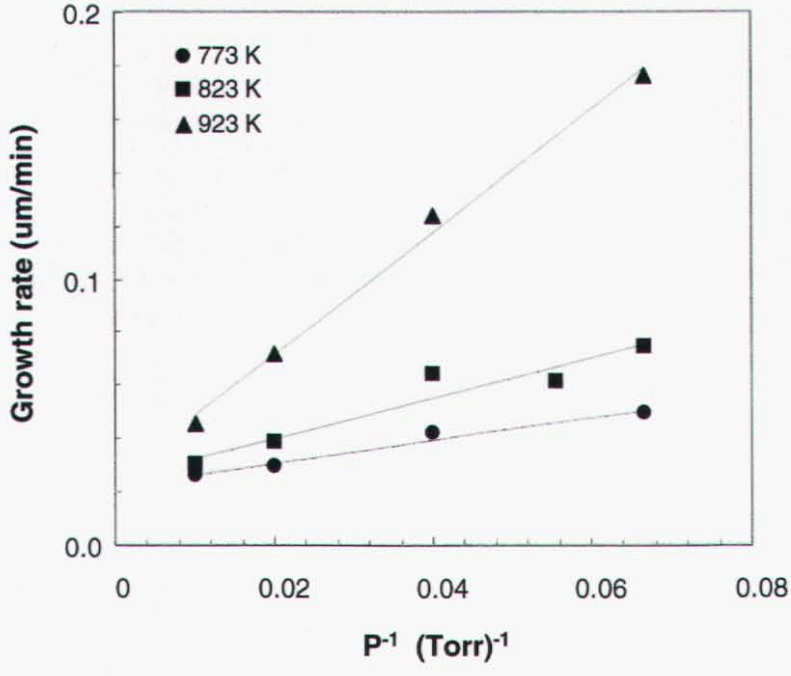

Figure 4-17. Influence of total pressure on growth rate. The partial pressures of MBTC and O_2 are 0.025 and 10.0 Torr, respectively.

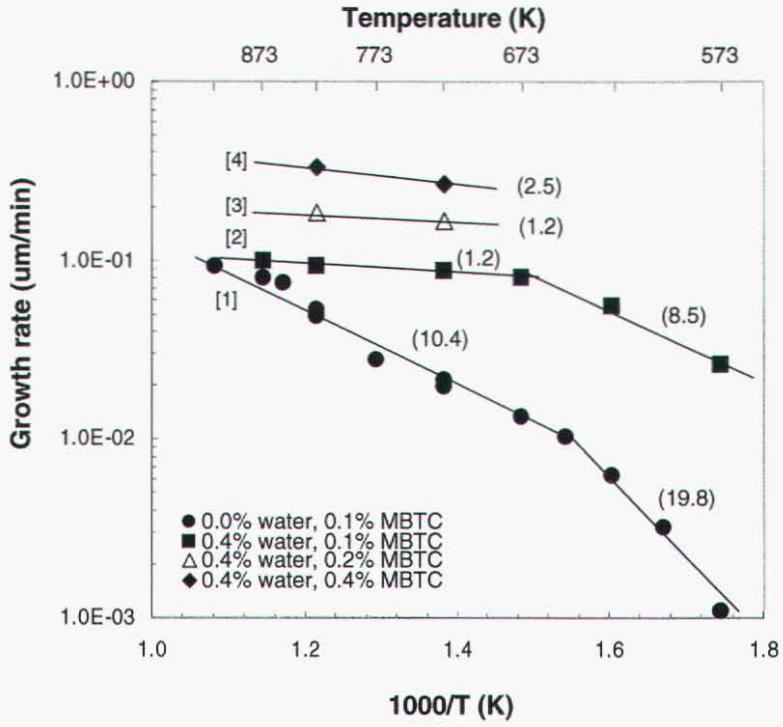

Figure 4-18. Comparison of growth rates obtained from MBTC + O_2 and MBTC + O_2 + H_2O mixtures at a total pressure of 25.0 Torr, total flow rate of 5.0 slpm, and 20.0 mol% O_2. The number in parenthesis represents the activation energy in kcal/mol.

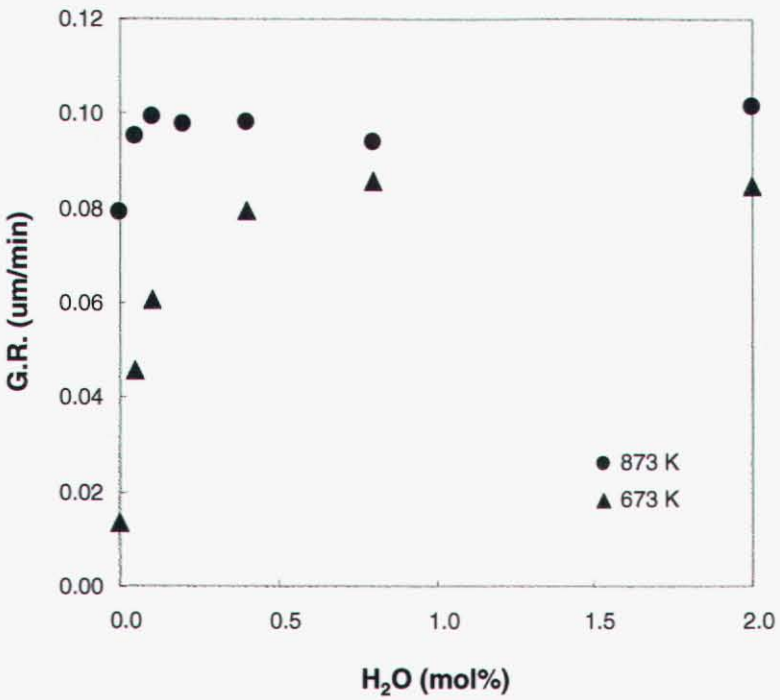

Figure 4-19. Effect of H_2O concentration on growth rate for MBTC + O_2 + H_2O reaction: total pressure of 25.0 Torr, and 0.1 mol% MBTC and 20.0 mol% O_2.

4.6 Summary and Conclusions

The investigations described in this chapter provide, for the first time, an extensive set of tin oxide growth rate data obtained under conditions that are both well characterized and sufficiently simple from the point of view of fluid flow that they can be used to develop and validate detailed models of tin oxide growth. The SFR design supplies not only well-behaved, uniform flow, leading to uniform growth rates across the substrate, but also an inherently simple reactor geometry that can be simulated using one-dimensional reacting flow models.

Growth rates measured using MBTC mixed with O_2 as the precursors are governed by multiple reaction mechanisms. While it is not possible from these data to isolate the contribution of gas-phase chemistry in this system, it appears that, under the conditions adopted in these experiments, heterogeneous processes dominate growth over most of the temperature range examined. In the 573–673 K range, undecomposed MBTC reacts with possibly chemisorbed oxygen at a relatively slow rate. We interpret the substantial change in the activation energy at 673 K as being caused by a shift from one heterogeneous mechanism to another, although higher temperatures will also accelerate gas-phase reactions that may ultimately lead to more reactive gas-phase precursors. At higher temperatures, the pressure dependence of the growth rate indicates that deposition begins to approach the mass-transport limit.

Consistent with results obtained by other investigators [12], we find that the addition of H_2O causes growth rates to increase at all but the highest temperatures examined (573–923 K). The effect is particularly dramatic at the low end of the temperature range, where growth rates can increase by as much as a factor of 21. Although the details of the chemistry are not clear, the rate-controlling step clearly shifts from surface-dominated kinetics in the absence of H_2O to growth limited by MBTC transport. The growth rate can be saturated at modest H_2O/MBTC ratios. These results suggest that either H_2O adsorption produces highly reactive, perhaps catalytic, sites that dominate the growth process, or that an extremely

rapid gas-phase process leads to the formation of species whose reactivity is much higher than that of MBTC and O_2 alone. We note that, although our data were obtained at low pressure, the magnitude of the measured growth rates is very similar to that observed by Lee et al. in their investigation of tin oxide deposition from MBTC/O_2/H_2O mixtures at 1 atm [12], suggesting that, at a minimum, it should be possible to extrapolate our results to atmospheric pressure, where full-scale manufacturing processes are operated. Additional experiments are required, however, to assess the effect of the higher MBTC concentrations used during manufacturing (on the order of 1 mol% or more).

The roles of O_2 and H_2O in SnO_2 CVD are still unclear. Although the effect of H_2O addition is large, the high growth rates thus obtained cannot be achieved in the absence of O_2. MBTC/H_2O mixtures produce only carbon films [7], demonstrating that O_2 has a crucial role in the deposition process. We previously speculated that the role of H_2O may be either to react with MBTC decomposition products to form more reactive gas-phase intermediates [19], or to form surface hydroxyl groups that increase the MBTC reactivity toward the surface. The role of O_2 in either case could be to remove surface carbon and thus maintain a reactive surface for deposition[19]. Thus, both homogeneous and heterogeneous processes must be considered in future investigations to establish the growth mechanism. Which mechanism is the most important for a particular film growth process depends on residence time, temperature profile of reaction region, and amount of H_2O present in the reactants.

4.7 References

1. A. B. Tripathi, D. A. Boyd, H. A. Gallivan, H. A. Atwater, R. M. Murray, D. G. Goodwin, L. R. Raja, R. J. Kee, and J. Musolf, in Proc. Fifteenth Int. Symp. Chem. Vap. Dep., M. D. Allendorf and M. L. Hitchman, Editors, PV 2000-13, p. 240, The Electrochemical Society Proceedings Series, Pennington, NJ (2000).
2. M. E. Coltrin, R. J. Kee, and G. H. Evans, J. Electrochem. Soc., 136, 819 (1989).
3. W. G. Breiland and G. H. Evans, J. Electrochem. Soc., 138, 1806 (1991).
4. A. Moller, R. Kall, V. Till, G. Wortberg, and G. Adomeit, J. Cryst. Growth, 174, 837 (1997).
5. M. E. Coltrin, R. J. Kee, G. H. Evans, E. Meeks, F. M. Rupley, and J. F. Grcar, "SPIN: A Fortran Program for Modeling One-Dimensional Rotating Disk/Stagnation-Flow Chemical Vapor Deposition Reactors", Sandia National Laboratories Report SAND91-8003 (1991).
6. A. B. Tripathi, In-situ diagnostics for metalorganic chemical vapor deposition of YBCO, California Institute of Technology (2001).
7. A. M. B. van Mol and M. D. Allendorf, in 16th Int. Symp. Chem. Vapor Dep./EUROCVD-14, M. D. Allendorf, F. Maury, and F. Teyssandier, Editors, PV 2003-08, p. 65, The Electrochemical Society Proceedings Series, Pennington, NJ (2003).
8. J. Szanyi, Appl. Surf. Sci., 185, 161 (2002).
9. W. S. Winters, G. H. Evans, and C. D. Moen, Sandia National Laboratories Report (1997).
10. S. V. Patankar, Numerical Heat Transfer and Fluid Flow, McGraw-Hill, New York (1980).
11. C. Houtman, D. B. Graves, and K. F. Jensen, J. Electrochem. Soc., 133, 961 (1986).
12. S.-M. Lee, D.-L. Kim, H.-J. Youn, and K. S. Hong, Jpn. J. Appl. Phys., 39, 407 (2000).
13. Chae, Y.; Houf, W. G.; McDaniel, A. H.; Troup, J.; Allendorf, M. D. J. Electrochem. Soc. 151, C527 (2004).
14. Allendorf, M. D.; Nielsen, I. M. B.; Melius, C. F.; Mol, A. M. B. v., in Teyssandier, F., Ed. in 6th Int. Symp. Chem. Vapor Dep./EUROCVD-14, The Electrochemical Society Proceedings Series, Pennington, NJ, PV 2003-8, 2003.
15. Mol, A. M. B. v. "Chemical Vapor Deposition Tin Oxide Thin Films", Ph.D. Thesis, Eindhoven University of Technology, 2003.
16. Allendorf, M.D., Nielsen, I.B., Melius, C.F., Van Mol, A.M.B. Proc. 16th Int. Symp. Chem. Vap. Dep. And EuroCVD-14, The Electrochemical Society, 2002.
17. Pope, S.B., Miller, J.A., Comb. Symp. 28, 1519 (2000).
18. Kee, R. J.; Rupley, F. M.; Miller, J. A.; Coltrin, M. E.; Grcar, J. F.; Meeks, E.; Moffat, H. K.; Lutz, A. E.; Dixon-Lewis, G.; Smooke, M. D.; Warnatz, J.; Evans, G. H.; Larson, R. S.; Mitchell, R. E.; Petzold, L. R.; Reynolds, W. C.; Caracotsios, M.; Stewart, W. E.; Glarborg, P.; Wang, C.; Adignun, O. Chemkin Collection; Release 3.6 ed.; Reaction Design, Inc.: San Diego, CA, 2000.
19. M. D. Allendorf, I. M. B. Nielsen, C. F. Melius, and A. M. B. van Mol, in 6th Int. Symp. Chem. Vapor Dep./EUROCVD-14, M. D. Allendorf, F. Maury, and F. Teyssandier, Editors, PV 2003-8, p. 55, The Electrochemical Society Proceedings Series, Pennington, NJ (2003).
20. G. Gaggiotti, A. Galdikas, S. Kaciulis, G. Mattogno, and A. Setkus, J. Appl. Phys., 76, 4467 (1994).

21. P. G. Harrison, A. Ashworth, E. N. Clark, and J. McManus, J. Chem. Soc. Faraday Trans., 86, 4059 (1990).

22. D. S. Vlachos, P. D. Skafidas, and J. N. Avaritsiotis, Sensors Actuators B-Chem, 25, 491 (1995).

23. R. Matero, A. Rahtu, M. Ritala, M. Leskela, and T. Sajavaara, Thin Sol. Films, 368, 1 (2000).

24. M. D. Allendorf and A. M. B. van Mol, submitted to Topics Organomet. Chem. (2003).

This page intentionally left blank.

Chapter 5 Mechanism Development and Modeling of Tin Oxide CVD[†]

5.1 Introduction

As discussed in Chapter 4 [1], development of a model describing the SnO_2 deposition process from MBTC requires extensive knowledge of chemical reaction rates, including the kinetics of gas-phase MBTC pyrolysis, oxidation, and hydrolysis, as well as SnO_2 growth rates. Only two studies of SnO_2 deposition using MBTC have been reported [2, 3], and no quantitative models have been published.

In Chapter 4, we reported [1] SnO_2 growth rates as a function of substrate temperature, MBTC concentration, total pressure (15–100 Torr), and total flow rate. The data were obtained under highly controlled conditions in a stagnation-flow reactor (SFR). From a modeling perspective, the SFR geometry is very attractive, since stagnation flow can be transformed from two-dimensional to one-dimensional fluid motion by approximating it as flow over an unconfined infinite-radius disk [4]. This transformation greatly simplifies the calculation and enables rapid testing of complex deposition mechanisms. Analysis of the growth-rate data obtained in this way showed that deposition from MBTC + O_2 mixtures is governed by multiple reaction mechanisms, but that heterogeneous processes dominate growth over most of the range of substrate temperatures examined.

The previous work also quantified the effect of adding H_2O to the MBTC + O_2 mixture, which is well known to accelerate SnO_2 CVD rates [1]. At all but the highest temperatures examined (573–923 K), H_2O increases the growth rate measured in the SFR substantially. Increases as large as a factor of 21 were measured at 573 K, decreasing to a factor of 1.2 at 873 K. The H_2O/MBTC ratio required to saturate the growth rate also increases with temperature. From these results, we suggested that either H_2O adsorption produces highly reactive, perhaps catalytic, sites that dominate the growth process, or that a rapid gas-phase process leads to the formation of an MBTC-H_2O complex or tin hydroxide whose reactivity is much higher than that of MBTC and O_2 alone. The results are consistent with measurements by Lee et al. [2] made in a tubular reactor at 1 atm.

In this chapter, we describe an analysis of the SFR data obtained previously [1] to develop models that predict the growth of SnO_2 from MBTC + O_2 mixtures, including the effect of H_2O addition. To increase the utility and robustness of these models, we also report additional growth rate measurements that characterize the effect of O_2 concentration on the growth rate and extend the range of total pressures used to 100 Torr. Two mechanisms for deposition from MBTC + O_2 mixtures and four mechanisms for deposition from MBTC + O_2 + H_2O mixtures are proposed and evaluated, and comparison with the SFR data leads to selection of the most probable mechanism in each case. Since industrial-scale SnO_2 deposition processes operate at atmospheric pressure, we extrapolate the model to these conditions and find that the predicted growth rates agree with the published results of Lee et al. within a factor of 1.5. The selected models, while not of an elementary chemical nature, are chemically reasonable and capture the trends exhibited by the experiments across a wide range of process variables.

[†] The text in this chapter was originally published in the paper, Y. Chae, W. G. Houf, A. H. McDaniel, M. D. Allendorf, "Mechanisms for the Chemical Vapor Deposition of Tin Oxide from Monobutyltintrichloride," *J. Electrochem. Soc.*, 153 (2006), C309.

5.2 Numerical Modeling

5.2.1 Computational Methods

Although the gas flows within the SFR used for SnO_2 deposition experiments are, at a minimum, two-dimensional, it has been shown that the flow impinging on the substrate can be accurately modeled using a one-dimensional reacting-flow code, in which the stagnation flow between showerhead and substrate is transformed from 2-D fluid motion to 1-D by considering an unconfined infinite-radius disk.[7] This greatly simplifies and accelerates the calculations and enables rapid testing of complex deposition mechanisms. For the analyses described here, we used the SPIN model [8] from the CHEMKIN suite of codes.[9]

SPIN requires transport data for all gas-phase species included in the mechanism (viscosity, diffusivity, and thermal conductivity) and chemical kinetic mechanisms describing any chemistry occurring in the gas-phase and on the surface. Transport data for non tin-containing reactants and products were taken from the CHEMKIN Transport Database.[10] Heat capacity data for MBTC and the $C_4H_9SnCl_3$–H_2O gas-phase complex were obtained from ab initio calculations; [11] all other heat capacities are taken from the CHEMKIN Thermodynamic Database.[10, 12] The diffusivity and viscosity of the two tin species were calculated from kinetic theory based on Lennard-Jones parameters.[6] Transport properties for all gas-phase species used in the mechanisms considered here are listed in Table 5-1. The base case experimental conditions are given in Table 5-2. For modeling the surface chemistry, a maximum density of open surface sites of 5.0×10^{-9}mol/cm^2 was assumed, based on the density of SnO_2.

Table 5-1. Transport properties of species used in the simulations.

Species name	ε/K_B	σ	μ	α
$C_4H_9SnCl_3$	528.069	5.500	0.000	0.000
$C_4H_9SnCl_3$-H_2O	549.780	4.053	0.000	0.000
HCl	344.700	3.339	0.000	0.000
Cl_2	316.000	4.217	0.000	0.000
N_2	97.530	3.621	0.000	1.760
H_2O	572.400	2.605	1.844	0.000
C_2H_4	280.800	3.971	0.000	0.000
O_2	107.400	3.458	0.000	1.600

ε/K_B, σ, μ, and α are, respectively: Lennard-Jones potential well depth in Kelvins; collision diameter in Angstroms; dipole moment in Debye; and polarizability in cubic Angstroms.

Table 5-2. Initial conditions for simulation to predict growth rates over total pressure of 15 to 100 Torr.

Total flow rate (sccm)	5000
MBTC (Torr)	0.025
O2 (Torr)	10
H2O (Torr)	0.1
N2 (Torr)	balance to total pressure
Total pressure (Torr)	15 - 100
Inlet velocity (cm s-1)	124.0 (15 Torr)
	75.8 (25 Torr)
	18.9 (100 Torr)

5.2.2 Approach to Mechanism Development

The results of previous experiments, modeling, and theory described earlier in this report allow constraints to be placed on the characteristics of potential deposition mechanisms, thereby simplifying the scope of the problem considerably. Several assumptions were thus made to facilitate model development. First, film growth is assumed to be at steady-state under the experimental conditions, since no induction time is found for deposition from MBTC + O_2 mixtures.[1] Second, gas-phase reactions are assumed not to be rate-limiting in these experiments, a conclusion developed in our earlier experimental investigation of SnO_2 CVD from MBTC.[1] In that work (reproduced in Figure 5-1, we showed that the growth rate is independent of gas-phase residence time (varied by changing the total gas flow rate) at 823 K, indicating that the rate-limiting process is a surface reaction.

Measurements of MBTC decomposition rates in a stirred tank reactor [5] suggest that there is potential for gas-phase MBTC pyrolysis at the highest temperatures we examined (923 K). These kinetics, obtained at 1 atm and a residence time of 2.0 s, indicate that temperatures ≥773 K are required for measurable decomposition. In our experiments, the residence time at this temperature is less than 0.2 s (determined by integrating the velocity profile calculated by SPIN). Due to pressure falloff effects, the MBTC decomposition rate will be slower at 25 Torr by about a factor of 4, based on RRKM calculations we performed. Thus, we estimate that at 923 K, 29% of the MBTC decomposes at a gas flow rate 5000 sccm, with much smaller amounts at higher flow rates due to the shorter gas-phase residence times. Thus, in the modeling analysis that follows, we assume that the byproducts of tin oxide deposition are the result of surface chemistry, not gas-phase decomposition of precursors. The only species considered here are HCl, C_2H_4, and CO, based on FTIR experiments [5] identifying these as the primary gas-phase species produced during SnO_2 deposition from MBTC. Other observed products, such as CO_2, H_2O, CH_4, CH_2O, and 1–C_4H_8, are not accounted for by our mechanisms.

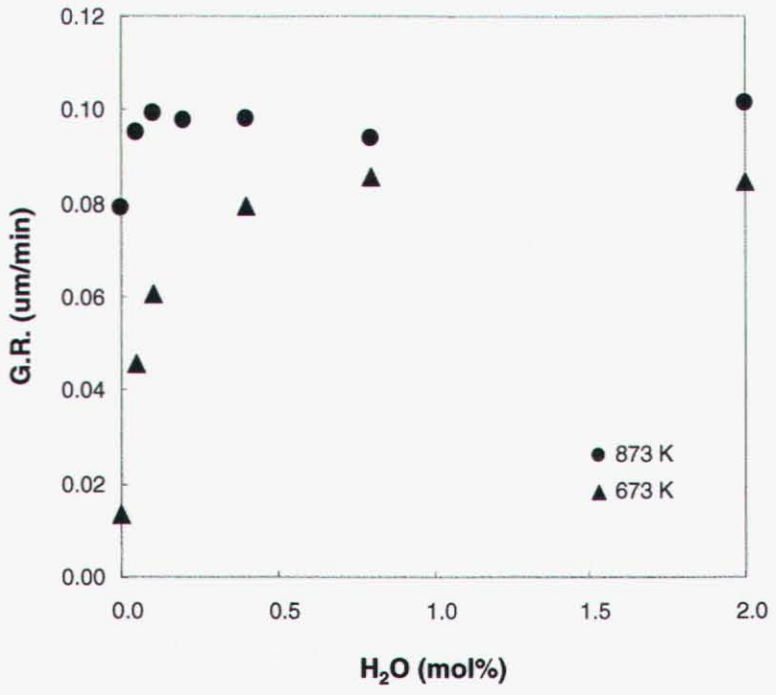

Figure 5-1. Effect of gas inlet velocity (V_{inlet}) on growth rate. Growth rates were obtained from 0.1 mol % MBTC + 20 mol % O_2 mixtures at substrate temperatures of 823 K and 923 K and a total pressure of 25 Torr (symbols). Curves are growth rates simulated using model 1B.

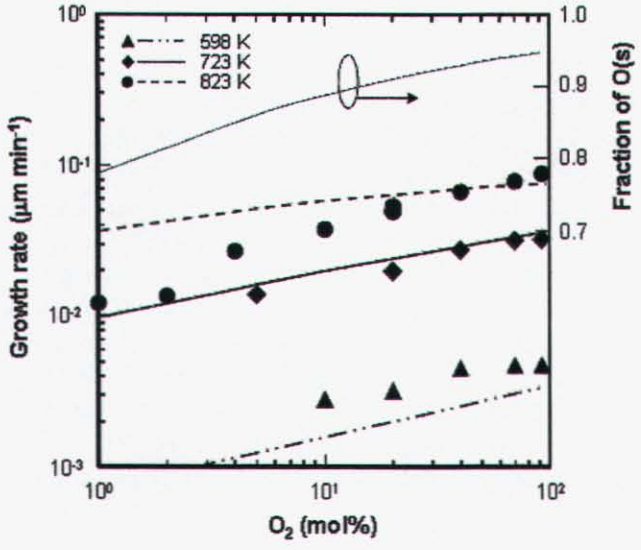

Figure 5-2. Effect of oxygen on the growth rate as a function of temperature for 0.1 mol % MBTC + O_2. The three bottom curves show the growth rates simulated by model 1B. The top solid curve is the fraction of sites occupied by adsorbed oxygen atoms [O(s)] at 723 K. The total pressure is 25 Torr. The sticking coefficient of O_2 [$\gamma(O_2)$] used for all simulations shown is 10^{-4}.

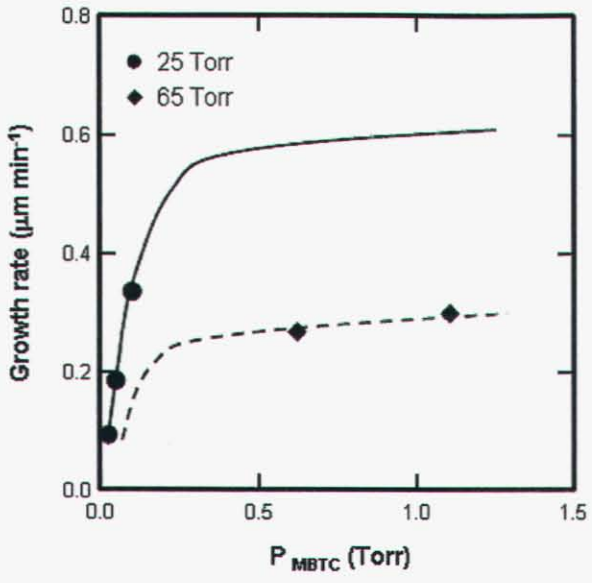

Figure 5-3. Comparison of growth rates at total pressures of 25 and 65 Torr for MBTC+O_2+H_2O at 823 K. Curves are the growth rate obtained from model 2D. The simulation conditions are 20 mol % (5 Torr) O_2 + 0.4 mol% (0.1 Torr) H_2O for 25 Torr, and 7.7 mol % (5 Torr) O_2 + 0.15 mol% H_2O (0.1 Torr) for 65 Torr.

A third assumption is that sticking coefficients (γ) for species on open adsorption sites (designated OS(s) in each mechanism) are assumed to be 1.0. This assumption was made during the initial stages of model development in order to reduce the number of adjustable parameters. As will be seen below, this does not appear unreasonable, particularly for large molecules such as the tin precursors. In addition, we find (see Results section) that model predictions are largely insensitive to $\gamma(O_2)$. Since experimental and computational investigations in the literature indicate that the details of the O_2 adsorption process in particular are complex, including coverage and temperature-dependent sticking coefficients, and we are unable to experimentally probe surface oxygen, building additional complexity into the model is not warranted.

Based on these assumptions, we consider two possible reaction mechanisms for SnO_2 growth from MBTC + O_2 mixtures, as shown in Figure 5-4 and Table 5-3. The first mechanism assumes that adsorbed MBTC (reaction S1) reacts with gas-phase O_2 (Model 1A). Reaction S2, which describes this reaction, yields the gas-phase byproducts (C_2H_4, HCl, and CO) that are observed in the FTIR experiments[5]. In the second mechanism (Model 1B), MBTC reacts with an oxygen-covered surface (reaction S4), formed by dissociative adsorption of O_2 (reaction S3). The same gas-phase products are formed as in model 1A, with the addition of Cl_2 to balance the chlorine; unfortunately, Cl_2 cannot be detected by FTIR, so we have no direct evidence of its formation.

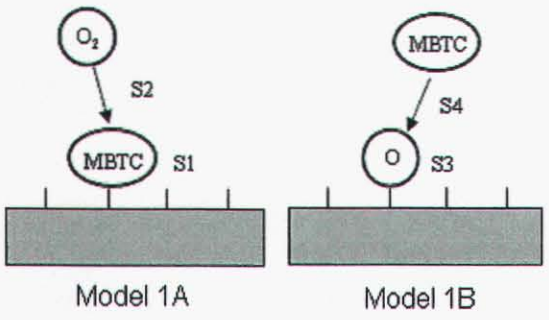

Figure 5-4. Reaction models for the deposition from MBTC + O_2 mixtures. S1-S4 refer to the reactions shown in Table 5-3.

Table 5-3. Reaction mechanisms and rate constants.

	A	E_a
1) Model 1A		
S1. $C_4H_9SnCl_3$ + OS(s) → $C_4H_9SnCl_3$(s)	S.C. = 1*	
S2. $C_4H_9SnCl_3$ (s) + 3/2O_2 → SnO_2 (B) + 3/2 C_2H_4 + 3HCl + CO + OS(s)	5.0×10^{15}	19000
2) Model 1B		
S3. O_2 + 2OS(s) → 2O(s)	S.C.=1*	
S4. $C_4H_9SnCl_3$ + 2O(s) → SnO_2 (B) + $2C_2H_4$ + HCl + Cl_2 + 2OS(s), $[C_4H_9SnCl_3]^{0.74}$	2.0×10^{23}	20000
3) Model 2A		
S5. $C_4H_9SnCl_3$ + OS(s) → $C_4H_9SnCl_3$ (s)	S.C. =1*	
S6. $C_4H_9SnCl_3$ (s) + 1/2O_2 + H_2O → SnO_2 (B) + $2C_2H_4$ + 3HCl + OS(s), $[H_2O]^{0.5}$, $[O_2]^{1.12}$	1.5×10^{16}	12000
4) Model 2B		
S7. O_2 + 2OS(s) → 2O(s)	S.C.=1*	
S8. $C_4H_9SnCl_3$ + H_2O + O(s) → SnO_2 + $2C_2H_4$ + 3HCl + OS(s)	2.0×10^{25}	20000
5) Model 2C		
G9. $C_4H_9SnCl_3$ + H_2O → $C_4H_9SnCl_3$-H_2O	4.0×10^{14}	10000
S10. O_2 + 2OS(s) → 2O(s)	S.C. =1*	
S11. $C_4H_9SnCl_3$-H_2O + O(s) → SnO_2 (B) + $2C_2H_4$ + 3HCl + OS(s)	1.0×10^{27}	21000
6) Model 2D		
G12. $C_4H_9SnCl_3$ + H_2O → $C_4H_9SnCl_3$-H_2O, $[C_4H_9SnCl_3]^{0.72}$	4.0×10^{14}	10000
S13. $C_4H_9SnCl_3$-H_2O + OS(s) → $C_4H_9SnCl_3$-H_2O(s)	S.C.=1*	
S14. $C_4H_9SnCl_3$-H_2O(s) + 1/2O_2 → SnO_2 (B) + $2C_2H_4$ + 3HCl + OS(s), $[O_2]^{0.76}$	1.0×10^{10}	13700

(s) and (B) indicate an adsorbed species and deposited species on the surface, respectively. Fitted reaction orders are shown following the reaction (e.g., the reaction order of O_2 in S6 is 1.12). OS(s) and O(s) are the open (vacant) site and oxygen site adsorbed on a surface, respectively. S.C. stands for sticking coefficient. Units of A and E_a are mol-cm-sec-K and cal mol^{-1}, respectively. The superscript numbers on brackets are the reaction order against the species in the brackets.

* Sticking coefficient initially assumed to be unity. See text for discussion of growth rate sensitivity to this value.

To model the effect of mixing H_2O with the reactant gases on the growth of tin oxide films, we considered an additional class of mechanisms in which MBTC and H_2O react in the gas phase to form a complex. Previously we reported [1] that growth saturates with increasing H_2O concentration and speculated that this may be due either to the saturation of surface OH groups or to formation of a reactive gas-phase MBTC–H_2O complex. Unlike the MBTC + O_2 reaction, however, a gas-phase reaction in which premixed MBTC and H_2O form a complex is predicted by ab initio calculations to be exothermic[13, 14]:

$$C_4H_9SnCl_3 + 2H_2O \rightarrow C_4H_9SnCl_3(H_2O)_2 \qquad \Delta H_o\ (298\ K) = -14.85\ kcal/mol \qquad (5\text{-}1)$$

Thus, we developed two basic categories of mechanisms for this deposition chemistry: (1) all reactions occur on the surface and (2) gas-phase complex formation followed by surface reaction. Four plausible reaction models were considered as shown in Figure 5-5. Rate constants for these reactions were determined by manual fitting, within the constraints described in this section. Models 2A and 2B are purely heterogeneous and involve formation of adsorbed MBTC (2A) or O (2B), followed by a surface reaction with other gas-phase reactants. The sticking coefficients for the adsorption reactions were initially set to 1.0 and were then varied to characterize the sensitivity to this reaction. Manual fitting was performed by adjusting the A factor and E_a of the surface reactions of S6 and S8. Models 2C and 2D include an irreversible gas-phase reaction to form an MBTC–H_2O complex, followed by adsorption and either a surface reaction (S11) between O(s) and the MBTC-H_2O complex, or a surface reaction (S14) between MBTC–H_2O(s) and O_2, respectively. The gas-phase reaction between MBTC and H_2O is assumed to be irreversible, since experimental evidence presented below indicates this process, if it occurs, must be very fast. Transport properties for the MBTC–H_2O complex were estimated based on the collision diameter, Lennard-Jones potential well depth, and dipole moments of MBTC and H_2O.

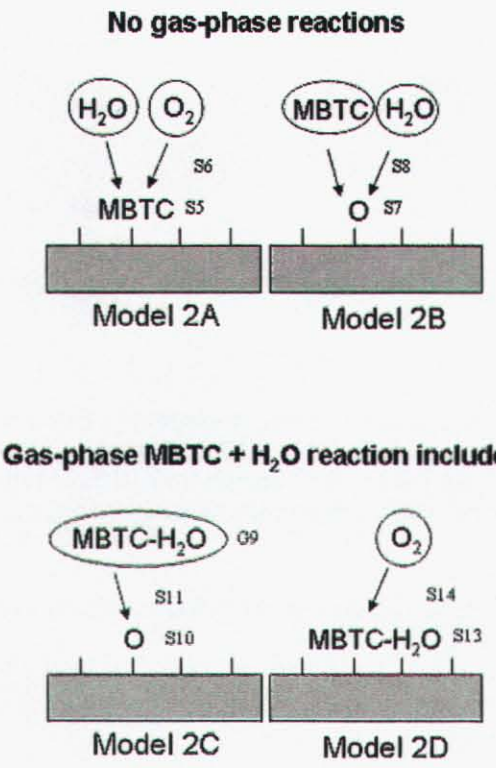

Figure 5-5. Possible reaction models for MBTC + O_2 + H_2O. S5-S14 and G9 are the surface and gas-phase reactions shown in Table 5-3.

Note that all mechanisms considered here are global in nature and are not designed to capture the details of elementary heterogeneous processes. Since we have no way to probe such reactions in the SFR, developing mechanisms comprised of detailed elementary surface reactions would not only needlessly increase the number of adjustable parameters, but would also artificially build in chemistry that is not based on experimental evidence.

5.3 Results

5.3.1 Deposition from MBTC + O_2 Mixtures

Due to the high O_2 concentration in our experimental conditions, model 1B is the more chemically appealing one of the two shown in Figure 5-4, and there is some evidence in the literature to support it. Pulkkinen et al.[15] simulated the kinetics of adsorption, dissociation, and desorption of O_2 at the SnO_2 surface using Monte Carlo techniques. They reported that O_2 dissociates when it adsorbs on SnO_2 surfaces. The oxygen surface coverage is about 50 times higher than that of other components (O_2, O_2^-, and O^-).

For both mechanisms, rate constants were obtained by fitting the pre-exponential factor A and activation energy E_a to the experimental data shown in Figure 5-6 (from Ref. 1; 25 Torr total pressure, 0.1 mol% MBTC, 20 mol% O_2). We assumed a simple first-order reaction to MBTC and changed the reaction order for mechanism 1B only. The sticking coefficient in reactions S1 and S3 was fixed at 1.0, as discussed above. The results of these fits are also shown in Figure 5-6, and the resulting rate constants are given in Table 5-3.

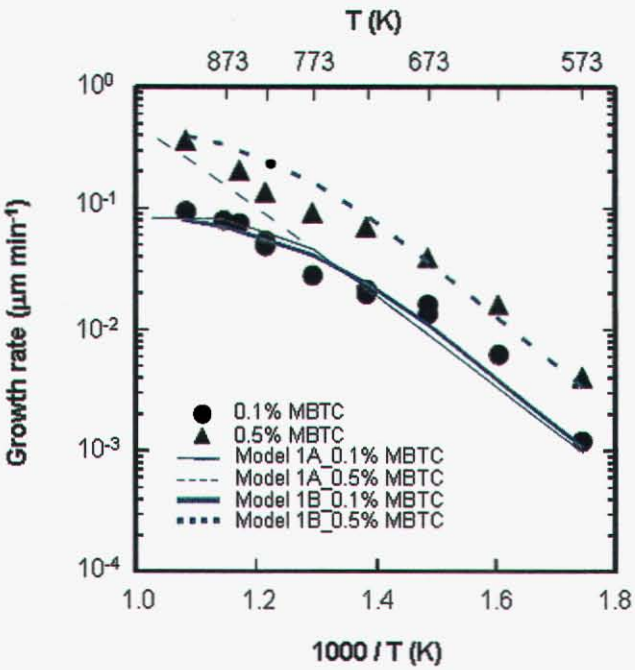

Figure 5-6. Comparison of growth rates simulated using models 1A and 1B with experimental data for 0.1 – 0.5 mol % MBTC + 20 mol % O_2 mixtures. Bold and thin curves show the growth rate simulated using models 1B and 1A, respectively.

Models 1A and 1B can be distinguished by comparing their ability to predict both the temperature and MBTC concentration dependence, as seen in Figure 5-6. Model 1A is only partially successful in reproducing the observed growth rates. Although the best fit to the 0.1 mol% MBTC data is rather good (deviations of 19, 1, and 2 % are found at 573, 723 and 873 K, respectively), these rate constants produce a different trend at 0.5 mol% MBTC than that exhibited by the data. In particular, the predicted growth rates are insensitive to the MBTC concentration below 773 K and do not show the nonlinear behavior above this temperature. On this basis, we exclude Model 1A from further consideration.

Model 1B reproduces the trends displayed by the experimental growth-rate data for both 0.1 mol% and 0.5 mol% MBTC. In this case, the predicted growth rate increases with MBTC concentration at all temperatures. The best-fit rate activation energy of 20 kcal/mol is consistent with our previously measured [1] values, which ranged from 19.9 to 17.8 kcal/mol. The MBTC reaction order obtained from the fit (0.74) also agrees with the values obtained by experiments (0.74 ± 0.09). Note that Model 1B predicts that the surface reaction step (S4) is rate-determining. In Ref. 7 we speculated that the change in activation energy (Figure 5-6) is the result of a change in mechanism. However, Model 1B describes this transition reasonably well, suggesting that the change is due to a gradual shift toward mass-transport-limited growth.

The robustness of Model 1B is evident from a comparison of predicted and measured growth rates as a function of inlet O_2 concentration. Reasonable agreement is obtained without modification of the rate constants, as seen in Figure 5-2. Predicted growth rates are within a factor of two of the observed rate at $T < 723$K, although the predictions for 598 K do not capture the plateau observed at ≥40 mol% of O_2. At 823 K, the agreement is not good at low O_2 concentrations. This may occur because oxygen adsorption in the model is irreversible, while in the experiments oxygen can desorb from the surface. The desorption of surface oxygen is most likely slower at lower temperatures, leading to saturation of the growth rate as the surface becomes fully covered by adsorbed oxygen. Although we are unaware of any other reports of SnO_2 growth dependence on O_2, the observed trend is similar to deposition of SnO_2 from $SnCl_4$ and O_2. Ghoshtagore suggested an Eley–Rideal mechanism in which chemisorbed oxygen reacts with gas-phase $SnCl_4$ [16, 17].

Model 1B also reproduces the trend in the growth rate as a function of inlet gas velocity. Deviations from experiment are no more than 50% in all cases (Figure 5-1). This supports the overall concept of the mechanism, namely, that gas-phase residence times are sufficiently short under these conditions that unreacted MBTC interacts with the substrate to form SnO_2. Although gas-phase reactions at 923 K may be occurring, two observations suggest that they do not affect the growth kinetics under these conditions. First, experiments indicate that the thermodynamically stable tin-containing products of MBTC decomposition and oxidation at these temperatures are $SnCl_4$ and $SnCl_2$, both of which are known to have slower SnO_2 growth kinetics at 1 atm than MBTC [6, 16, 17]. Thus, gas-phase reactions should produce less-reactive species and thus cause the growth rate to decrease with temperature, rather than increase. In contrast, the data in Figures 5-1 and 5-6 both show that growth rates increase continuously with temperature. The small (~30%) increase in growth rate at 923 K seen in Figure 5-1 as the inlet gas velocity increases by a factor of 4 is consistent with a small amount of gas-phase MBTC decomposition (shorter gas-phase residence times lead to more of the reactive MBTC reaction, rather than less reactive decomposition products). Thus, although gas-phase MBTC reactions cannot be completely ruled out in these experiments, the available data and modeling are consistent with the assumption discussed above that this chemistry makes a minor contribution to the growth rate under these conditions.

As discussed above, a value of 1.0 was assigned to the O_2 sticking coefficient $\gamma(O_2)$ in reaction S3 to minimize the number of adjustable parameters in the model. However, variation of $\gamma(O_2)$ shows that growth rates predicted by Model 1B are insensitive to this parameter until its value becomes very small. The effect of varying $\gamma(O_2)$ in reaction S3 is shown in Figure 5-7. The ratios of the rate calculated for a

given value of $\gamma(O_2)$ to the growth rate at $\gamma(O_2) = 1.0$ are plotted as a function of O_2. Above $\gamma(O_2) = 0.01$, the growth rates are the same as those at $\gamma(O_2) = 1.0$ because the surface has sufficient O(s) coverage to react with MBTC. Decreasing $\gamma(O_2)$ further to 10^{-4} results in only minor deviations from the growth rate predicted at $\gamma(O_2) = 0.01$ (maximum of 16%).

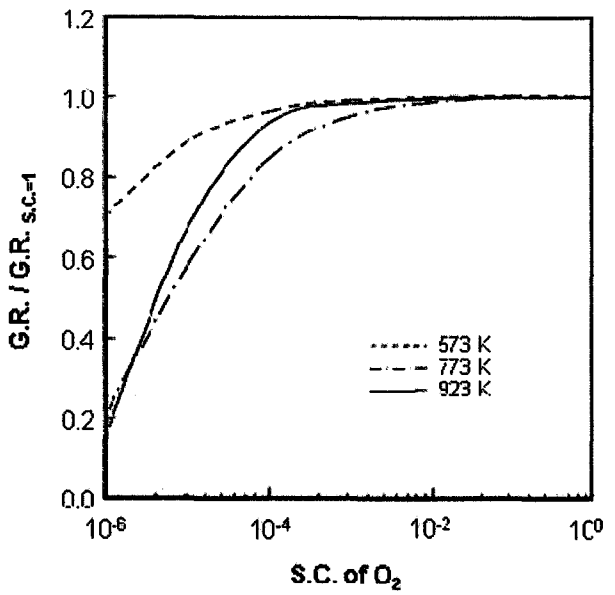

Figure 5-7. The effect of varying O_2 sticking coefficient on the growth rate (G.R.) predicted by model 1B. The *A* factor and E_a of reaction S4 were fixed while the sticking coefficient of S3 was varied.

Unfortunately, there are no published experimental values of $\gamma(O_2)$ on SnO_2 for comparison with these results. However, Pulkkinen et al. used $\gamma(O_2) = 0.01$ in kinetic Monte Carlo simulations of O_2 adsorption on SnO_2 from 400 to 1000 K.[15] On the chemically similar $TiO_2(110)$ surface (the thermodynamically most stable surface), Henderson et al.[18] found an initial value $\gamma(O_2)$ of 0.5–0.6 that decreased to 0.05 at the highest O_2 exposures employed. Their results indicate that O_2 adsorption above 150 K is dissociative and occurs at surface oxygen vacancy sites representing <5 % of the surface sites. In contrast, Gopel et al.[19] obtained an initial sticking coefficient of 8×10^{-5} at 300 K on $TiO_2(110)$, which they also attribute to an adsorption process involving intrinsic surface defects that are thermodynamically stable at temperatures up to 1000 K. These results indicate that mechanism 1B is qualitatively consistent with observations concerning O_2 adsorption, but that temperature- and coverage-dependent effects on $\gamma(O_2)$ are present that are not fully captured in the model. The lack of sensitivity to $\gamma(O_2)$ indicates, however, that it is not necessary to capture the details of this adsorption process to obtain an accurate prediction of SnO_2 growth rates from MBTC + O_2 mixtures.

5.3.2 Deposition from MBTC + O_2 + H_2O Mixtures

As discussed above, a total of four different mechanisms were considered to describe tin oxide growth from mixtures of MBTC with O_2 and H_2O. The best-fit rate expressions for each mechanism (reactions S5 through S14) are given in Table 5-3. As in the case of MBTC + O_2, the *A* factor and E_a were used as simulation parameters and were obtained by fitting the experimental data at 0.1 mol% MBTC, 20 mol% O_2, 0.4 mol% H_2O, and total pressure of 25 Torr.

All four models are in good agreement (within a factor of 2 or better; Figure 5-8) over the entire temperature range of the experimental data for deposition from 0.1% MBTC (for clarity, some predictions of models 2B and 2C are omitted in Figure 5-8). Furthermore, the fitted activation energies (12–21 kcal/mol) are in good agreement with the experimental values, indicating that the model description of the kinetically limited regime (substrate temperatures <~673 K) is at least consistent with the data. However, models 2B and 2C predict an increase in growth rate as the MBTC concentration increases, contrary to the experimental observations at surface temperatures <673 K. The experimental data indicate that growth rates at these temperatures are independent of the MBTC concentration (0.1 to 0.4 mol% MBTC).

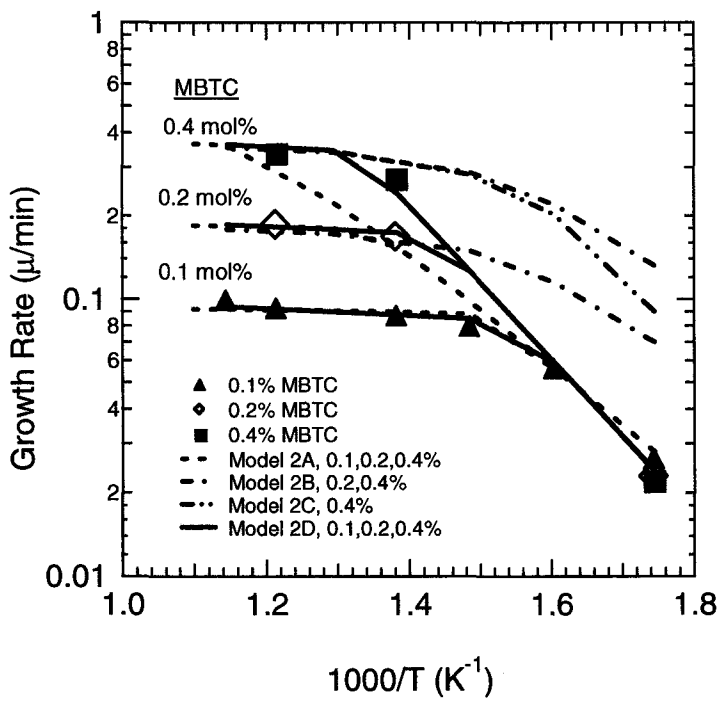

Figure 5-8. Comparison of growth rates predicted by models 2A-2D. MBTC concentrations are indicated in the figure. For all curves, the remaining input conditions are 20 mol % O_2, 0.4 mol % H_2O, and 25 Torr total pressure. For clarity, some simulation results for models 2B and 2C are omitted.

The simulations just described assume a sticking coefficient ($\gamma(C_4H_9SnCl_3)$ or $\gamma(C_4H_9SnCl_3\text{-}H_2O)$ of 1.0 in reactions S7 and S10. Because a surface reaction is the rate-controlling step below 673 K, a change in γ may produce a different trend in the growth rate. To characterize the effect of this value on the predicted growth rate, the values of γ were varied over the range from 1.0×10^{-7} to 1. The results show that decreasing γ reduces the absolute growth rate, but the trends with MBTC concentration are similar to those predicted when $\gamma = 1.0$. Thus, on this basis, models 2B and 2C can be excluded from further consideration, leaving only mechanisms 2A and 2D as potential candidates for the deposition from MBTC + O_2 + H_2O mixtures. These models give very similar results at substrate temperatures ≥673 K, so the effects of other process variables must be examined to distinguish between the two. Data from our previous work and the new data discussed above enable such a distinction through a comparison of the growth dependencies on O_2 and H_2O.

The dependence of the growth-rate on O_2 predicted by models 2A and 2D is quite different, as seen in Figure 5-9, in which data and results for all four models are displayed for a substrate temperature of 823

K and 0.1 mol% MBTC and 0.4 mol% H_2O inlet concentrations. The growth rate calculated from model 2A increases with O_2 concentration and then saturates above 5 mol% O_2. Although this trend is similar to the experimental data, there are large deviations below 5 mol% O_2. On the other hand, the predictions of model 2D are in good agreement with the data, having a maximum deviation of 26% at 1 mol% O_2. The reaction order obtained from fitting the model to the O_2 dependence in the region where the growth rate changes with O_2 is 0.76, similar to the value 0.68 that is experimentally measured. Thus, model 2D, involving formation of a gas-phase MBTC–H_2O complex, has better fidelity with the complete data set than any of the other models.

As a final check, the two models were compared with the dependence of the growth rate on inlet H_2O concentration, as seen in Figure 5-10. Growth rate profiles simulated using models 2A and 2D both agree well with experimental data at temperatures of 673 and 873 K (at 0.1 mol% MBTC, 20 mol% O_2, and total pressure of 25 Torr). The predictions of model 2A become similar to those of model 1A for MBTC + O_2 when the H_2O concentration becomes extremely low, as expected. However, the growth rates predicted by model 2A deviate significantly from the data at higher MBTC concentrations (by a factor of 1.7 from the data at 723 K and 0.4 mol% MBTC; not shown in Figure 5-8), while those of model 2D are in better agreement. Thus, model 2D remains the most effective one for simulating tin oxide growth from MBTC + O_2 + H_2O mixtures.

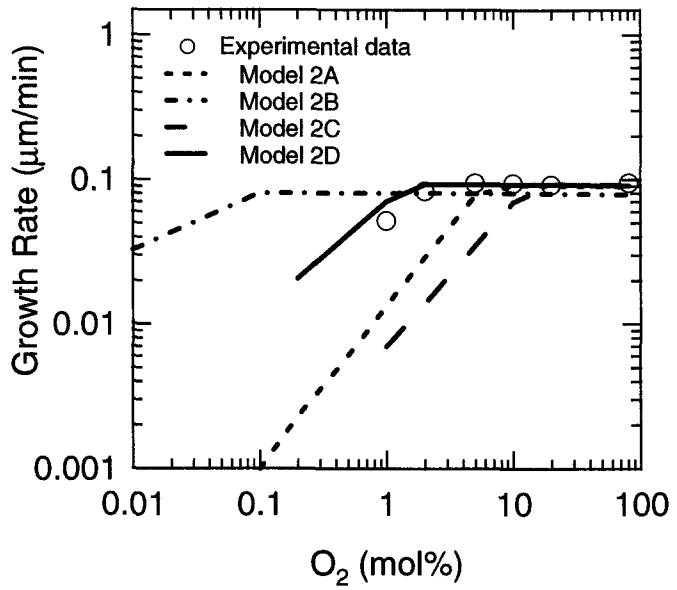

Figure 5-9. The effect of O_2 concentration on growth rate as a function of temperature for 0.1 mol % MBTC + O_2 + 0.4 mol % H_2O at a total pressure and substrate temperature of 25.0 Torr and 823 K, respectively. Curves show the simulation results obtained from models 2A-2D.

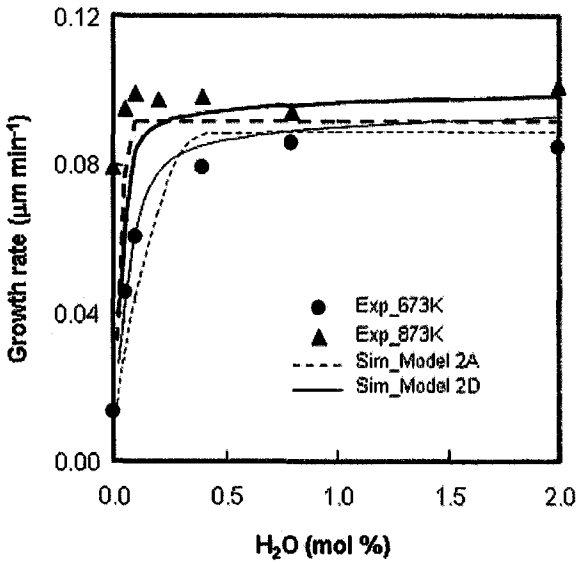

Figure 5-10. Comparison of experimental data with simulated growth rate using two reaction models 2A and 2D for 0.1 mol % MBTC + 20 mol % O_2 + H_2O at 25 Torr. Bold curves show the growth rate predicted at 873 K.

Model 2D implies that the MBTC–H_2O species is very reactive, having a sticking coefficient (reaction S13) of 1. Although this sticking coefficient was initially set to unity to reduce the number of fitting parameters, as remarked upon above, we find that γ(MBTC-H_2O) must be reduced by more than a factor of 10 to alter the predictions significantly. For example, reducing γ(MBTC-H_2O) from 1 to 0.01 increases the deviation of the predicted growth rate at 873 K from 4.4% to only 25.7%. This is consistent with the experimental observation that growth at this temperature is at the mass transport limit.

Reaction G12 (gas-phase complex formation) is assumed to be irreversible. However, it may be that the complex is actually only an intermediate and that the real precursor is a gas-phase hydroxide, perhaps formed by the following reversible reactions:

$$C_4H_9SnCl_3 + H_2O \leftrightarrow C_4H_9SnCl_3(H_2O) \quad (5\text{-}2)$$

$$C_4H_9SnCl_3(H_2O) \leftrightarrow C_4H_9SnCl_2(OH) + HCl \quad (5\text{-}3)$$

This sequence is consistent with the first-order dependence on H_2O concentration in model 2D. Thermodynamic data are not available to assess whether or not equilibrium favors the formation of either $C_4H_9SnCl_3(H_2O)$ or $C_4H_9SnCl_2(OH)$. However, using data calculated by ab initio methods for $C_4H_9SnCl_3(H_2O)_2$ and $C_4H_9SnCl(OH)_2$, [20] equilibrium calculations performed for the conditions in Figure 5-8 (0.1% MBTC) predict that 1.4% of the MBTC reacts to form the dihydroxide at 573 K, while at 873 K nearly 8% of the MBTC reacts. These results suggest that a gas-phase reaction between MBTC and H_2O could form significant amounts of a tin hydroxide. To achieve the large increases in growth rates observed when H_2O is added to the system requires that the hydroxide product be much more reactive with adsorbed species on the surface than MBTC itself, since most of the MBTC is not converted to the complex. This is consistent, however, with the high sticking coefficient used in model 2D.

5.3.3 Model Extrapolation to Higher Pressures and MBTC Concentrations

The reaction models discussed above were developed using data obtained at relatively low precursor concentrations and total pressures. Practical SnO_2 deposition processes, however, operate at atmospheric pressure and concentrations of the tin-containing precursor ≥1 mol%.[21] Thus, it is important to establish the utility of the model for use under other operating conditions by comparing its predictions with deposition rates obtained under a wider range of experimental conditions. Since models 1B and 2D have the best overall performance, we compared their predictions with the previously measured pressure and reactant concentration dependencies to determine whether they can be extended to other conditions.

For deposition from MBTC + O_2 mixtures, growth rates simulated using model 1B as a function of pressure up to 100 Torr at 773 K are in good agreement with experimental data, as shown in Figure 5-11 (Parameters for the simulations are listed in Table 5-2). Deposition rates for MBTC + O_2 + H_2O mixtures simulated by model 2D (Figure 5-11) are also in good agreement with experimental data. Under the conditions of these experiments, the thermal boundary layer thickness does not vary with pressure, because the convective mass flux toward the surface is constant. However, the diffusion mass flux to the surface depends on pressure, due to the P^{-1} dependence of the concentration gradient within the boundary layer[1]. It is evident from the model predictions shown in Figure 5-11 that the growth rate decreases as the total pressure increases and that the simulations are in good agreement with experiments. This indicates that growth is mass-transport limited under these conditions (consistent with Figure 5-8) and that it is possible to predict the growth rate within a factor of 1.5 over the pressure range 15–100 Torr.

The growth-rate dependence on MBTC concentration agrees well with model 2D results for MBTC + O_2 + H_2O mixtures, as shown in Figure 5-3. Although the body of data is relatively small, the predictions clearly capture the initial rise in the growth rate as the MBTC concentration increases. The simulations also reproduce the plateau that occurs in the data. The model indicates that this occurs when the MBTC concentration becomes sufficiently high that the surface is saturated with adsorbed MBTC–H_2O complexes.

Although we cannot obtain growth rate data at 1 atm in the SFR, the experimental results of Lee et al.[2] provide an opportunity to test the robustness of the model at this pressure, which is typical of on-line glass coating operations. A comparison with these data provides a particularly rigorous test, since a tubular reactor with the substrate resting on the bottom of the tube was used, which is quite different from the SFR. To model these experiments, the boundary-layer code CRESLAF [22] from the CHEMKIN suite of codes was used. Films were grown from 1.0 mol% MBTC, 20 mol% O_2, and 0.5–2.0 mol% H_2O. Unfortunately, some assumptions were necessary to model the experiments because Lee et al. omitted some key information, including the exact position of the substrate within the reactor and the shape of the temperature profile. We assumed that the substrate was placed at 10 cm from reactor inlet and that the temperature of the reactor wall is uniform. Figure 5-12 shows a comparison of Lee et al.'s data with simulated growth rates using model 2D. The results indicate that model 2D predicts the growth rate with average deviations of 31.6% and 30.5% found at 0.5 mol% and 1.5 mol% H_2O, respectively. However, the model does not capture the trend at 0.5 mol% H_2O, and overpredicts the effect of increasing the H_2O concentration, although the slight bend in the experimental curve is reproduced by the model in the 1.5 mol% simulation. The reasons for this are not clear, but the disagreement is not surprising, given the lack of complete clarity regarding the conditions of the experiments. The model does accurately predict the activation energy for growth, however. At 1.5 mol% H_2O, the experimental activation energies are 0 and 2.33 kcal/mol for the regions 873–923 K and 723–823 K, respectively, while the model predicts 0.13 kcal/mol for the region of 723–923 K. These low activation energies indicate that the growth rate is near the mass transport limit of the precursor. This result suggests that the model 2D description of the chemistry, although obtained at low pressures, can be extended to the conditions that are more realistic for industrial coating reactors.

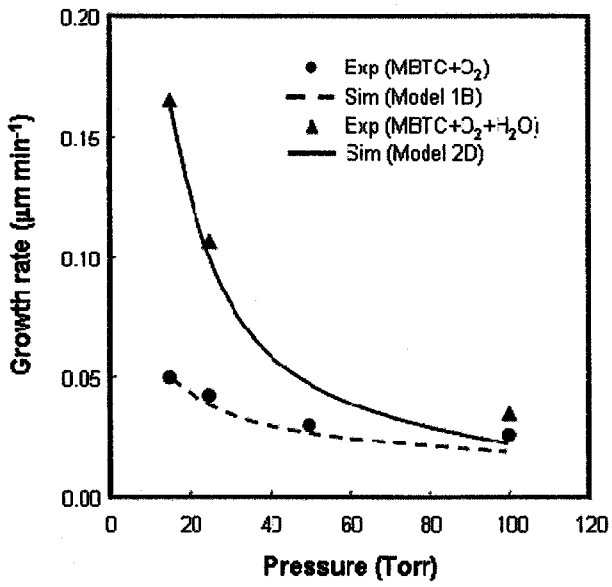

Figure 5-11. Comparison of the experimental growth rate with the growth rate predicted by model 1B and 2D as a function of total pressure. Partial pressures of MBTC, O_2, and H_2O were fixed at 0.025, 10, and 0 or 0.1 Torr, respectively. The substrate temperature was 773 K.

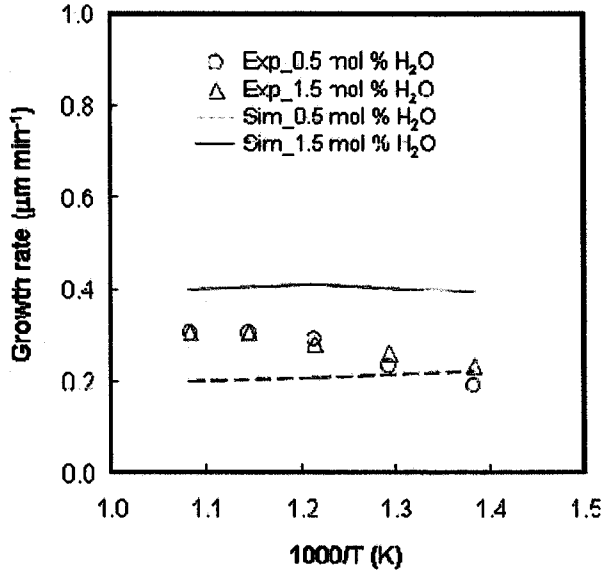

Figure 5-12. Comparison of simulated growth rates and experiments published by Lee et al. [2] for 1.0 mol % MBTC + 20 mol % O_2 + 0.5 – 1.5 mol % H_2O mixtures. The total pressure is 1 atm. Growth rates are simulated using model 2D.

5.4 Conclusions

The results described here provide for the first time robust kinetic models capable of predicting SnO_2 growth rates over a wide range of deposition conditions. Model development is based on data described in Chapter 4 that allow model validation for the effects of substrate temperature, total pressure, inlet O_2 concentration, inlet flow velocity, and MBTC, O_2, and H_2O concentrations. Tin oxide deposition from MBTC + O_2 mixtures is best described by model 1B in which MBTC reacts with adsorbed oxygen, while growth from MBTC + O_2 + H_2O mixtures is most accurately captured by model 2D, in which an MBTC–H_2O complex formed in the gas phase transports tin to the surface. The effect of varying deposition parameters on the growth rate is, in general, captured by the models, with both the qualitative trends and the quantitative values in reasonable agreement with experimental data (within a factor of two or better). The robustness of these models can be attributed to two factors. First, growth rates were obtained in a SFR whose geometry provides a well-behaved, one-dimensional flow environment that is well suited to modeling. Second, gas-phase pyrolysis and oxidation of MBTC is either nonexistent or minimal due to short gas-phase residence times and low pressures used in the experiments. This allows growth to be modeled using a straightforward adsorption step followed by a global expression describing the surface chemistry, or a fast, irreversible gas-phase reaction forming an MBTC–H_2O complex followed by adsorption and heterogeneous conversion to SnO_2.

The growth rates predicted by model 2D at higher pressures (up to 1 atm) and higher MBTC concentrations (up to 0.96 mol% at 65 Torr) are in good agreement with the experimental data, showing that this model can be extended to conditions other than those used to develop and validate it. Especially convincing in this regard is the relatively good agreement between the predictions and Lee et al's data [2] at 1 atm, which were obtained in a reactor with a completely different geometry from the one used to validate the models presented here.

Although the models described here provide a sound basis for simulating practical coating reactors, there remain a number of important aspects of the process that merit further experimentation. Of particular importance to large-scale coating of glass are the effects of coating additives and dopants, both of which are acknowledged to affect growth rates. Measurements of the gas-phase reaction kinetics, in particular rates of MBTC pyrolysis and oxidation, as well as the rate of the H_2O + MBTC reaction, are needed to more accurately assess the effects of temperature on growth rates. Although we conducted both experiments and modeling to assess the extent of MBTC gas-phase reaction in the SFR, it is clear that this chemistry is quite complex and requires a systematic approach before it can be incorporated in detail into process models. Finally, it is well known that the identity of the tin precursor has a substantial effect on film properties such as roughness, crystalline phase, and haze[23, 24]. A thorough investigation of this topic using the experimental approaches described here and in Chapter 4 would be a valuable contribution to the understanding of this important commercial CVD system.

5.5 References

1. Y Chae, W. G. Houf, A. H. McDaniel, J. Troup, M. D Allendorf, *J. Electrochem. Soc.* **151**, C527 (2004).
2. S.-M. Lee, D.-L. Kim, H.-J .Youn, K. S. Hong, *Jpn. J. Appl. Phys.* **39**, 407 (2000).
3. J. L. Buchanan, C. J. McKown, *Non-Cryst. Sol.* **218**, 179 (1997).
4. M. E. Coltrin, R. J. Kee, G. H Evans,. *J. Electrochem. Soc.* **136**, 819 (1989).

5. A. M. B. Van Mol, M. D. Allendorf, F. in Teyssandier, , Ed. *in 16th Int. Symp. Chem. Vapor Dep./EUROCVD-14*, The Electrochemical Society Proceedings Series, Pennington, NJ, PV 2003-08, 2003.

6. A. M. B. Van Mol, "Chemical Vapor Deposition Tin Oxide Thin Films", Ph.D. Thesis, Eindhoven University of Technology, 2003.

7. C. Houtman, D. B. Graves, K. F. Jensen, *J. Electrochem. Soc.* **133**, 961 (1986).

8. M. E. Coltrin, R. J. Kee, G. H. Evans, E. Meeks, F. M. Rupley, J. F. Grcar, "SPIN: A Fortran Program for Modeling One-Dimensional Rotating Disk/Stagnation-Flow Chemical Vapor Deposition Reactors," Sandia National Laboratories Report, SAND91-8003, 1991.

9. R. J. Kee, F. M. Rupley, J. A. Miller, M. E. Coltrin, J. F. Grcar, E. Meeks, H. K. Moffat, A. E. Lutz, G. Dixon-Lewis, M. D. Smooke, J. Warnatz, G. H. Evans, R. S. Larson, R. E. Mitchell, L. R. Petzold, W. C. Reynolds, M. Caracotsios, W. E. Stewart, P. Glarborg, C. Wang, O. Adignun, Chemkin Collection; Release 3.6 ed.; Reaction Design, Inc.: San Diego, CA, 2000.

10. R. J. Kee, G. Dixon-Lewis, J. Warnatz, M. E. Coltrin; J. A. Miller, "A Fortran Computer Code Package for the Evaluation of Gas-phase Multicomponent Transport Properties," Sandia National Laboratories Report1986.

11. M. D. Allendorf, C. F. Melius, *J. Phys. Chem. A* **109**, 4939 (2005).

12. R. J. Kee, F. M. Rupley, J. A. Miller, "The Chemkin Thermodynamic Database," Sandia National Laboratories Report, SAND87-8215, 1987.

13. M. D. Allendorf, A. M. B. Van Mol, in *Topics in Organometallic Chemistry*; R. A. Fischer, Ed.; Springer: Berlin, 2005; Vol. 9; pp 1.

14. A. M. B. Van Mol, Y. Chae, A. H. McDaniel, M. D. Allendorf, *Thin Sol. Films*, in press, 2005.

15. U. Pulkkinen, T. T. Rantala, T. S. Rantala, V. Lantto, *J. of Molecular Catalysis A: Chemical* **166**, 15 (2001).

16. R. N. Ghoshtagore, in *Proc. 6th Int. Symp. Chem. Vapor Dep.*; R. N. Tauber, Ed.; The Electrochemical Soc. Proc. Series: Pennington, 1977; Vol. PV77-5; pp 433.

17. R. N. Ghoshtagore, *J. Electrochem. Soc.* **125**, 110 (1978).

18. M. A. Henderson, W. S. Epling, C. L. Perkins, C. H. F. Peden, U. Diebold, *J. Phys. Chem. B* **103**, 5328 (1999).

19. W. Gopel, G. Rocker, R. Feierabend, *Phys, Rev. B.* **28**, 3427 (1983).

20. M. D. Allendorf, C. F. Melius, *Thermodynamics Resource*, www.ca.sandia.gov/HiTempThermo/index.html.

21. R. J. McCurdy, *Thin Sol. Films* **351**, 66 (1999).

22. M. E. Coltrin, H. K. Moffat, R. J. Kee, F. M. Rupley, "CRESLAF(Version 4): A Fortran Program for Modeling Laminar, Chemically Reacting, Boundary-Layer Flow in Cylindrical or Planar Channels," Sandia National Laboratories Report,SAND93-0478, 1993.

23. A. M. B. Van Mol, G. R. Alcott, M. D. Allendorf, *Ceram. Bull.* **84**, 37 (2005).

24. A. M. B. Van Mol, F. Grob,; K. Spee, K. Van Der Werf, R. Schropp, F. Teyssandier, , Ed. *16th Int. Symp. Chem. Vapor Dep.*, The Electrochemical Society Proceedings Series, PV2003-08, 2003.

Chapter 6 Global Deposition Kinetics from Pilot-Scale Reactor Data

6.1 Modeling of Glass Coater

6.1.1 Model Description

A schematic of an on-line float glass coater is shown in Figure 6-1. As mentioned in Chapter 1, in the on-line glass coating process, SnO_2 is deposited on the moving glass surface by atmospheric pressure chemical vapor deposition (APCVD) from an impinging flow of monobutlyltin trichloride (MBTC) gas. A reacting flow model of the PPG pilot coater was developed to provide understanding of the coater and coating process and to identify ways to improve efficiency and reduce waste. At the same time, staff at PPG performed a large range of experiments in the pilot coater to study the coating process experimentally and to provide data for model validation and chemical mechanism development. As a part of this effort, the model was also used test and refine chemical mechanisms for the deposition of SnO_2 from MBTC by comparison with the PPG pilot coater data.

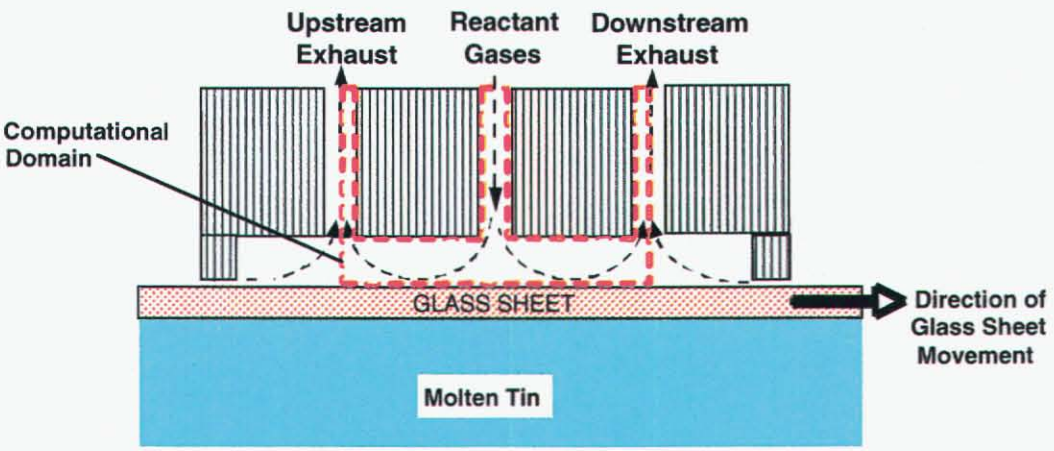

Figure 6-1. Schematic of on-line atmospheric pressure chemical vapor deposition (APCVD) float glass coater (computational domain shown as dashed red line).

A two-dimensional reacting flow model of the PPG pilot coater was developed using the Sandia-developed CURRENT [1] code. The model solves the two-dimensional Navier Stokes, energy, and species transport equations over the computational domain bounded by the dashed lines shown in Figure 6-1. The model includes a rigorous description of multicomponent diffusion, gas-phase chemistry, surface chemistry, and convective heat transfer. General sets of gas-phase and surface reactions can be specified for the model through the Sandia-developed CHEMKIN [2, 3] software linked to CURRENT.

Boundary conditions for the coater computational domain shown in Figure 6-1 included uniform reactant gas velocity, temperature, and concentration profiles at the inlet, where the gas velocity, temperature and species composition were specified based on data provided by PPG from the pilot coater experiments. At the glass surface, the glass temperature was either specified to be uniform based on average temperature measurements, or, in the later stages of the program, detailed temperature profiles measured in the experiments were input along the glass surface. The velocity of the moving glass sheet was also specified

based on data provided from PPG. The walls at the top surface of the coater were assumed to be maintained at a constant temperature based on measurements from each of the pilot coater experiments. As a first approximation, symmetry boundary conditions were assumed along the vertical boundaries of the computational domain formed from the centerlines of the upstream and downstream exhausts. Gas-phase chemistry, species, and heat transport were modeled throughout the computational domain with surface chemistry and deposition occurring on the moving glass surface.

6.1.2 Coater Simulations for MBTC without the Presence of Water

Initial simulations of the SnO_2 deposition in the PPG pilot coater were made for experiments where the reactant gases were MBTC and air without the presence of water. Based on the research from the early work of van Mol [4], a two-step global chemical reaction mechanism was proposed, consisting of a one gas-phase reaction and one surface reaction as shown in Table 6-1. In the gas-phase reaction, MBTC reacts with oxygen to form a gas-phase precursor referred to as $SnO_2(g)$. This highly reactive gas-phase species then reacts on the glass surface with a sticking coefficient of 1.0 to form deposited tin oxide ($SnO_2(D)$). A rate expression of the form shown in Table 6-1 was used for the gas-phase chemistry reaction. The pre-exponentional (A_o), activation energy (E), and MBTC reaction order (n) for this gas-phase reaction were determined by performing many 2-D simulations with the pilot coater reactor model, comparing the predicted SnO_2 mean deposition rates (averaged over the length of the glass plate) with pilot coater deposition data provided by PPG, and then adjusting A_o, E, and n until good agreement was reached between the predictions and data over the full range of the experiments. It is interesting to note that the reaction order dependence determined from this procedure (0.6 in MBTC) is in good agreement with the value of 0.59 obtained independently by PPG from analysis of the experimental data [5].

Figure 6-2 shows a typical result from the pilot coater simulation model where color-filled contours of the flow streamlines are shown over the reactor computational domain. The streamline plots show the formation of large vortices on the upstream and downstream sides of the impinging inlet reactant flow. This affects the growth of the boundary layer along the moving glass substrate and the SnO_2 deposition rate, as shown in Figure 6-3.

Table 6-1. Global reaction mechanism for SnO_2 deposition from MBTC and air used in simulations of the pilot coater for MBTC and air (no water).

Gas phase reaction:	$2\ C_4H_9SnCl_3 + 9\ O_2 \rightarrow 2\ SnO_2(g) + 6\ HCL + 8\ CO + 6\ H_2O$
	Rate (mol/cm^{3}s) = $A_o e^{-(E/RT)}[MBTC]^n$
	$A_o = 350$, $E = 16{,}534$ cal/mol, n = reaction order = 0.6
Surface reaction:	$SnO_2(g) \rightarrow SnO_2(D)$
	Sticking Coef. = 1

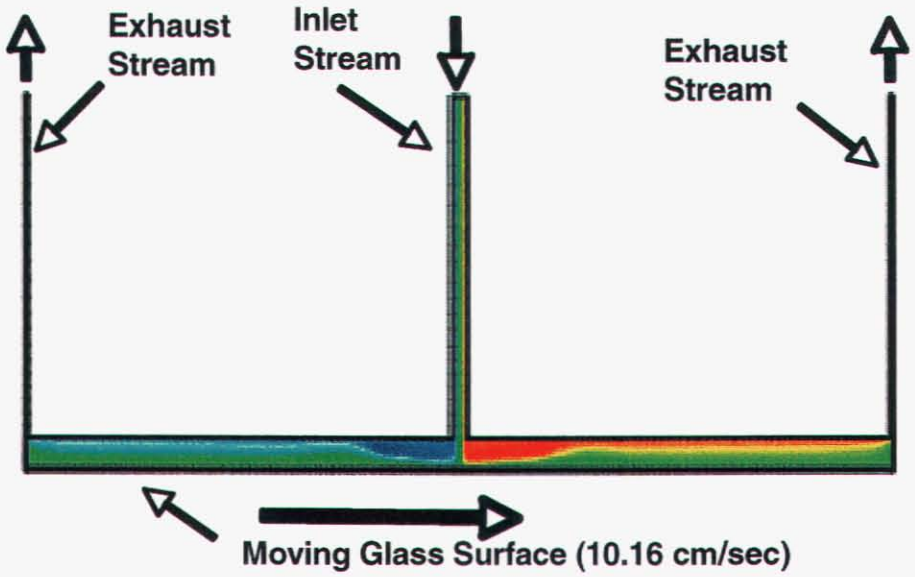

Figure 6-2. Color-filled contours of streamlines from the pilot coater simulation. Inlet flow rate of 85 slpm, inlet gas temperature of 450 K, inlet gas mole fractions of 0.5% MBTC, 16% oxygen, and 83.5% nitrogen, glass substrate temperature of 914 K.

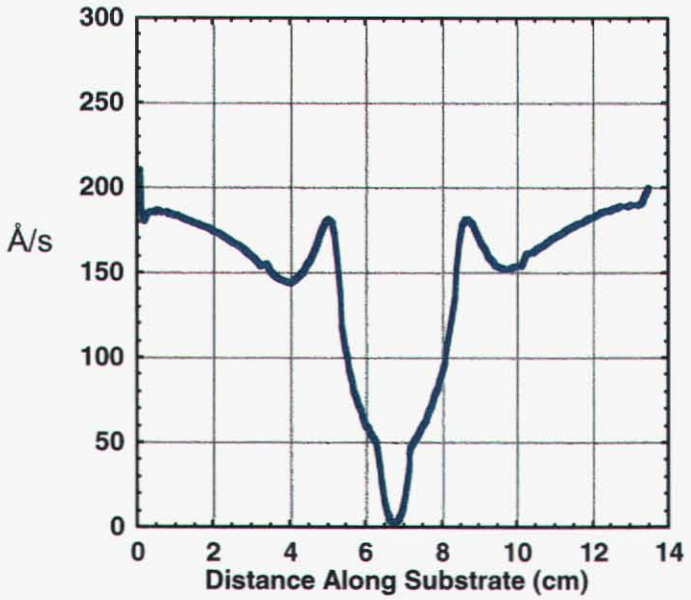

Figure 6-3. Computed SnO_2 deposition rate along the glass surface for the reaction mechanism given in Table 6-1 and the reactor operating conditions shown in Figure 6-2.

Figure 6-4 shows a comparison of mean SnO_2 deposition rates with the pilot coater data of PPG [5] for the case when MBTC and air (without water) are used as the reactant gases. Good agreement between the data and simulations are obtained for inlet MBTC mole fractions of 0.5, 1.0, and 2.0%, and glass substrate temperatures between 870 and 914 K. The chemical mechanism shown in Table 6-1 was used for the calculations.

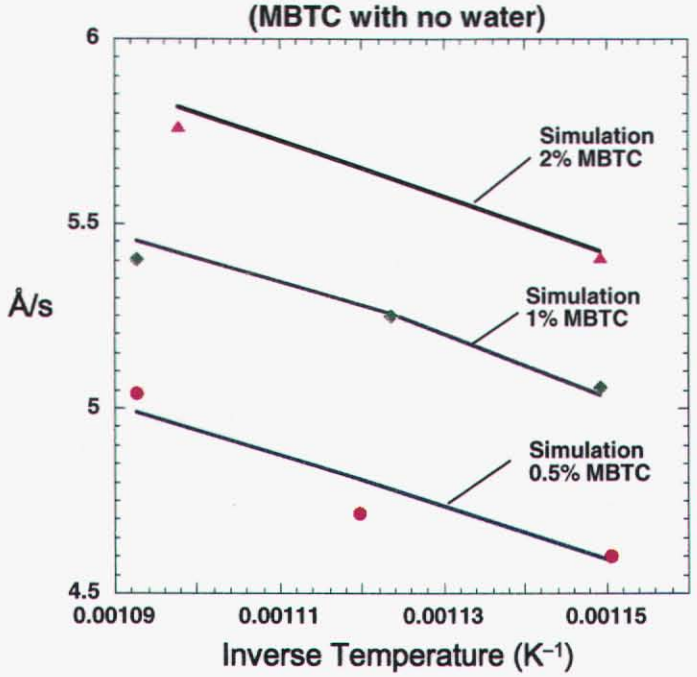

Figure 6-4. Comparison of predicted mean SnO_2 deposition rates (averaged over the length of the plate) from pilot coater simulations using the chemical mechanism given in Table 6-1 with deposition data supplied by PPG. Inlet flow rate was 85 slpm, and inlet gas temperature was 450 K.

6.1.3 Coater Simulations for MBTC and Water

Reacting flow simulations were performed with the coater model for the case where SnO_2 was deposited from MBTC and water in the presence of air. In this case, the water vapor serves as an accelerant for the reaction of MBTC with the oxygen in the air and produces a SnO_2 deposition rate on the glass surface approximately 100 times greater than when MBTC is used without water. To model the deposition process, the MBTC and water chemistry was approximated by a two-step global chemical reaction mechanism consisting of a one gas-phase reaction and one surface reaction as shown in Table 6-2. For the gas-phase reaction, MBTC reacts with oxygen in the air to form a gas-phase precursor referred to as $SnO_2(g)$. This reaction is similar to the gas-phase reaction used to model MBTC and oxygen without the presence of water vapor (Table 6-1), but the accelerant nature of water is now included by treating water as a third-body in the reaction. The highly reactive gas-phase species, $SnO_2(g)$, formed from this reaction then reacts on the glass surface with a sticking coefficient of 1.0 to form deposited tin oxide ($SnO_2(D)$), as in the previous MBTC with no water mechanism (Table 6-1).

A rate expression of the form shown in Table 6-2 was used for the gas-phase chemistry reaction. The pre-exponentional (A_o), activation energy (E), reaction order (n), and ratio A_o/A_∞ for this gas-phase reaction were determined by performing many 2-D simulations with the pilot coater reactor model, comparing the predicted SnO_2 mean deposition rates (averaged over the length of the glass plate) with pilot coater deposition data provided by PPG, and then adjusting A_o, E, n, and A_o/A_∞ until good agreement was reached between the predictions and data. Experiments were run for different inlet mole fractions of water vapor, different inlet mole fractions of MBTC, and different glass surface temperatures. Two sets of kinetic parameters were found to provide the best fit to this full range of data. These kinetic parameters sets are listed as "fit 1" and "fit 2" in Table 6-2.

Figure 6-5 shows a comparison of calculated deposition rates from the model with PPG pilot coater data for the case where the inlet mole fraction of water was varied while holding the inlet mole fraction of MBTC constant at 0.8% and the glass plate temperature constant at 912 K. Predicted deposition rate curves are shown for both sets of kinetic parameters for the MBTC–water mechanism in Table 6-2. Figure 6- 6 shows a similar comparison of measured and predicted mean SnO_2 deposition rates for the pilot coater where the inlet water vapor mole fraction was held constant at 2.0%, while the MBTC mole fraction was varied between 0.4 and 1.0% while holding the glass temperature constant at 912 K. Figure 6-7 shows the comparison of measured and predicted deposition rates for the pilot coater where the inlet MBTC and water vapor mole fractions were held constant at 1.0 and 1.9%, respectively, while the glass temperature was varied between 870 and 933 K. In general, the fit 1 kinetic parameters provided the best agreement with the deposition data when the inlet water vapor mole fraction was varied (Figure 6-5), while the fit 2 kinetic parameters provided the best agreement when the glass temperature was varied (Figure 6-7). Both the fit 1 and fit 2 kinetic parameters provide reasonable agreement with the deposition data for the cases where the inlet mole fraction was varied (Figure 6-6).

Table 6-2. Global reaction mechanism for SnO_2 deposition from MBTC, water, and air used in simulations of the pilot coater.

Gas phase reaction:	$2\ C_4H_9SnCl_3 + 9\ O_2\ (+\ H_2O) \rightarrow 2\ SnO_2(g) + 6\ HCL + 8\ CO + 6\ H_2O\ (+\ H_2O)$
	Rate $(mol/cm^3s) = A_o e^{-(E/RT)}[MBTC]^n[H_2O] / (1 + A_o/A_\infty [H_2O])$
	Fit 1: $A_o/A_\infty = 0.5 \times 10^6$, $A_\infty = 1300$, $E = 8600$ cal/mol, n = reaction order = 0.75
	Fit 2: $A_o/A_\infty = 0.5 \times 10^6$, $A_\infty = 2.5 \times 10^7$, $E = 25{,}000$ cal/mol, n = reaction order = 0.75
Surface reaction:	$SnO_2(g) \rightarrow SnO_2(D)$ Sticking Coef. = 1

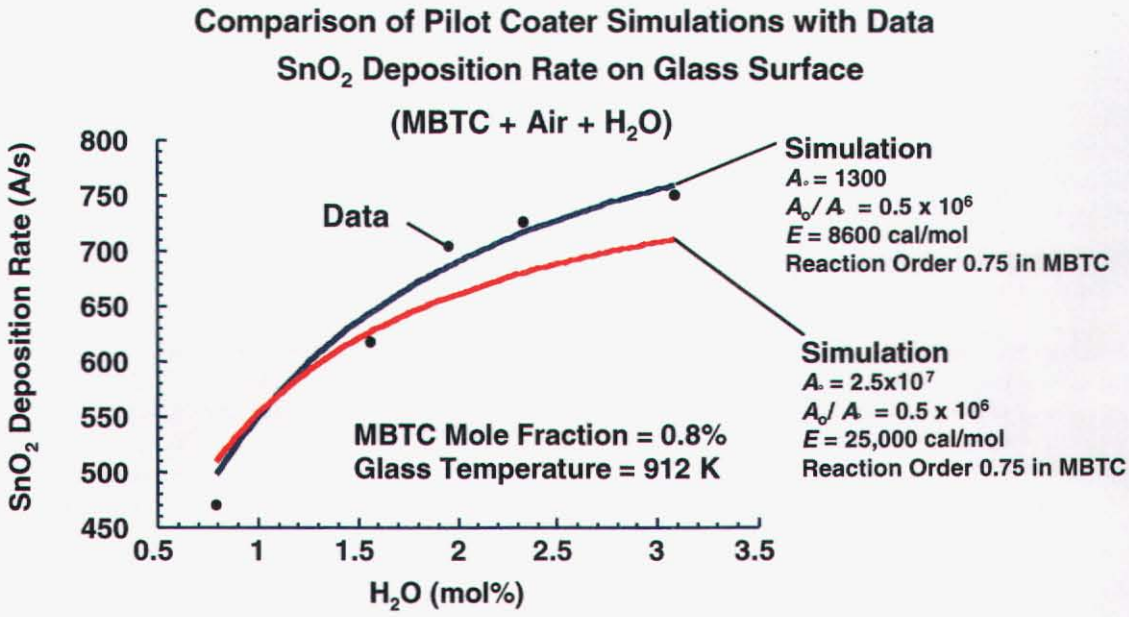

Figure 6-5. Comparison of measured and predicted mean SnO_2 deposition rates for the PPG pilot coater using the MBTC–water chemical mechanism given in Table 6-2. Inlet MBTC mole fraction was held constant at 0.8% while inlet water vapor mole fraction was varied. Inlet flow rate was 85 slpm; inlet gas temperature was 450 K; glass temperature was 912 K.

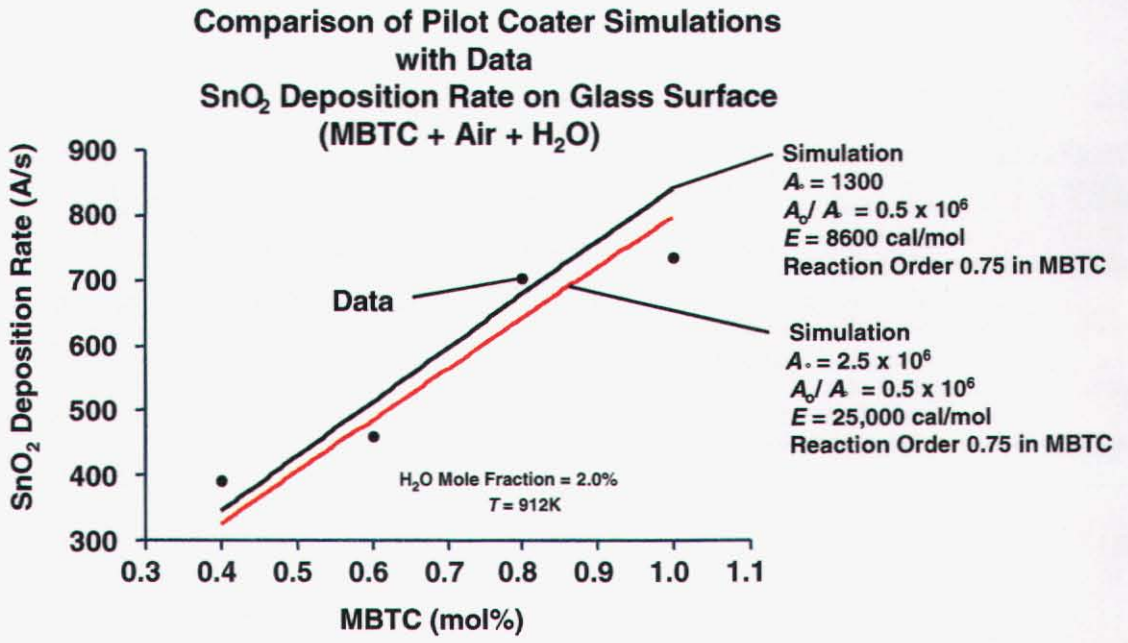

Figure 6-6. Comparison of measured and predicted mean SnO_2 deposition rates for the PPG pilot coater using the MBTC–water chemical mechanism given in Table 6-2. Inlet MBTC mole fraction was varied while inlet water vapor mole fraction was held constant at 2.0%. Inlet flow rate was 85 slpm; inlet gas temperature was 450 K; glass temperature was 912 K.

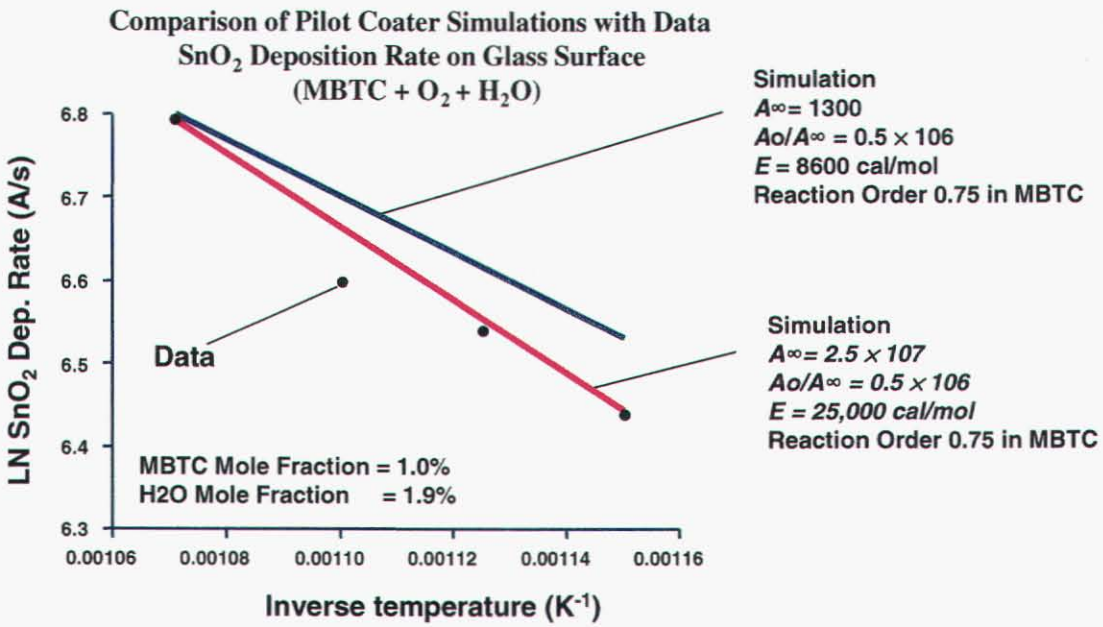

Figure 6-7. Comparison of measured and predicted mean SnO_2 deposition rates for the PPG pilot coater using the MBTC–water chemical mechanism given in Table 6-2. Glass temperature varied from 870 K to 933 K while inlet MBTC and water vapor mole fractions held constant at 1.0 and 1.9%, respectively. Inlet flow rate was 85 slpm, and inlet gas temperature was 450 K.

6.1.4 Glass Coater Parameter Studies

A parameter study was performed using the two-dimensional glass coater model described in Section 1.1 to evaluate the effects of changing important coater operating conditions on reactor performance and reactant utilization. The goal of this effort was to try to determine how coater operating conditions and/or coater geometry could be modified to increase efficient use of reactant inlet gas (MBTC) and thereby reduce waste. Because water is used as accelerant in plant-scale SnO_2 glass coaters, the MBTC–water chemical mechanism in Table 6-2 with the fit 2 kinetic parameters was used in the studies. Reactant utilization for the coater was defined as the ratio of the moles of Sn deposited on the glass surface to the moles of Sn flowing through the coater inlet. This ratio gives a measure of what percentage of the Sn in the inlet stream is deposited on the glass surface under the coater. Both the reactant utilization and average coater deposition rate over the glass surface were recorded for each set of operating conditions.

$$\text{Reactant Utilization} = \frac{\text{Moles of Sn Deposited}}{\text{Moles of Sn Flowing In}} \cdot 100\,\%$$

In the first parameter study, the glass temperature was varied between 860 and 940 K while the inlet MBTC and water vapor mole fractions were held constant at 1.0 and 1.9%, respectively. The inlet reactant gas flow rate was held constant at 85 slpm, and the inlet gas temperature was set equal to 450 K. A speed of 23.71 cm/s was used for the speed of the moving glass sheet, and the glass temperature was assumed to be uniform.

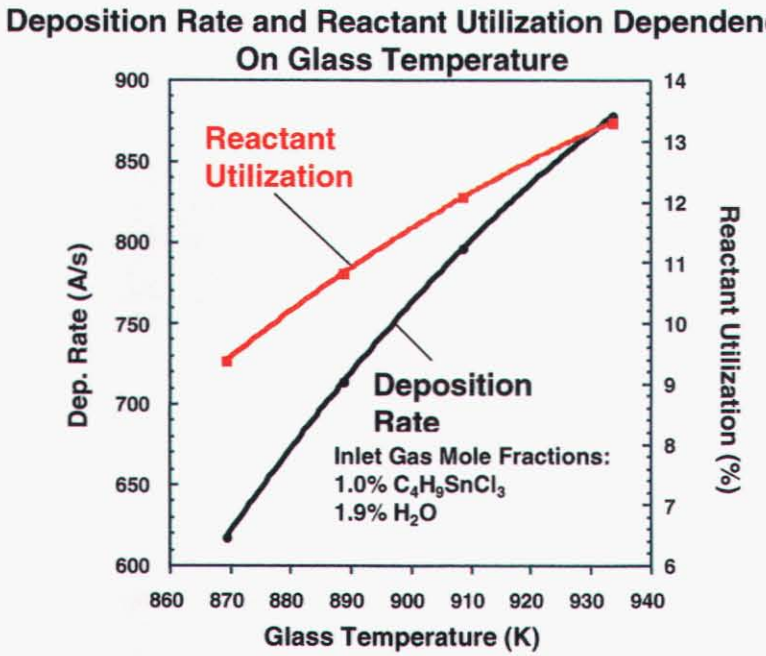

Figure 6-8. Effect of glass temperature on SnO_2 deposition rate and MBTC reactant utilization.

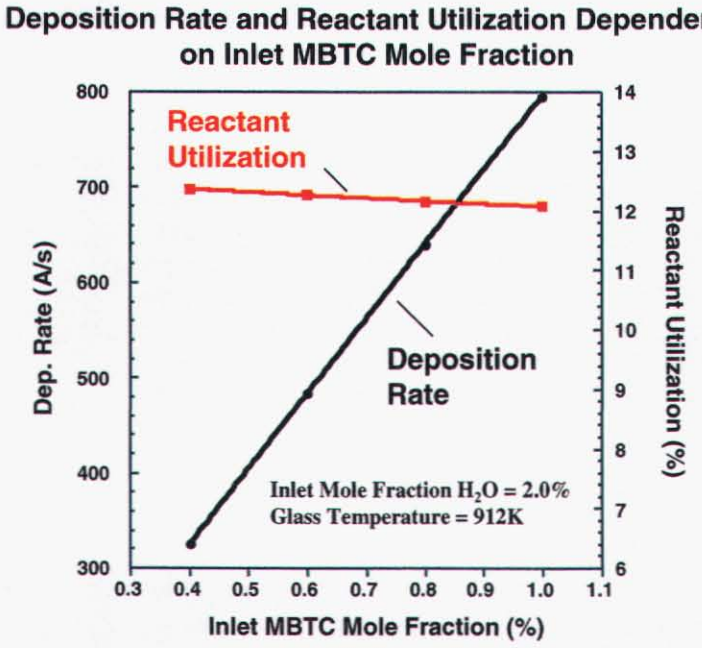

Figure 6-9. Effect of MBTC inlet concentration on SnO_2 deposition rate and MBTC reactant utilization.

Figure 6-8 shows the effect of altering the glass temperature on the average deposition rate across the glass surface and the reactant utilization. Reactant utilization is in the range of about 10% and is consistent with values reported from PPG. The results indicate that both reactant utilization and average deposition rate increase with increasing glass temperature. Figure 6-9 shows the results of a similar parameter study where the inlet mole fraction of MBTC was varied between 0.4 and 1.0% while the inlet mole fraction of water vapor was held constant at 2.0% and the glass temperature held constant at 912 K. The results indicate that SnO2 deposition rate increases with increasing MBTC inlet concentration while the reactant utilization remains nearly constant.

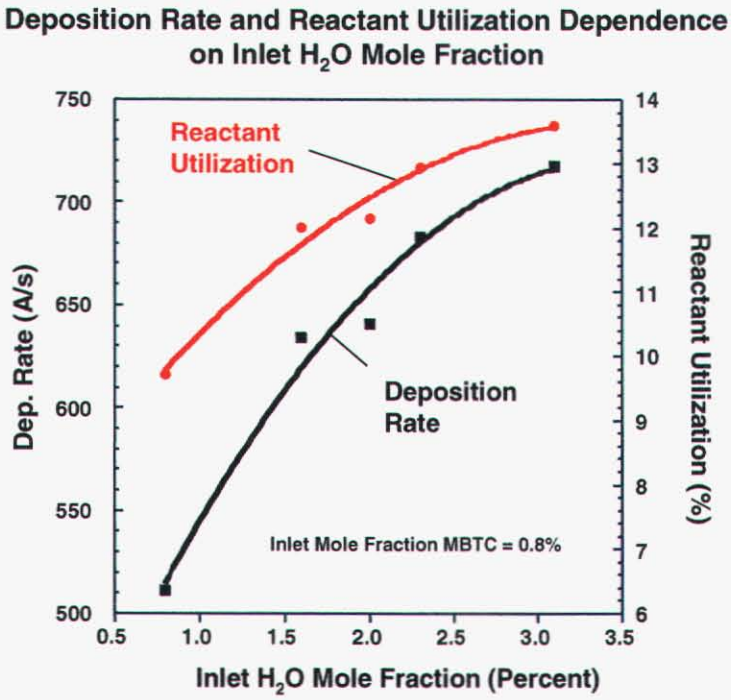

Figure 6-10. Effect of water vapor inlet concentration on SnO_2 deposition rate and MBTC reactant utilization.

Figure 6-10 shows the effect of varying the inlet water vapor mole fraction between approximately 0.8 and 3.2% while maintaining the inlet MBTC mole fraction at 0.8% and the glass temperature at 912 K. Results indicate that reactant utilization and SnO_2 deposition rate increase significantly as the inlet mole fraction of water is increased.

Figure 6-11 shows the effect of varying the inlet reactant temperature on coater performance, and Figure 6-12 shows how varying the inlet reactant flow rate affects performance. Both studies were performed for a constant uniform glass temperature of 909 K with the inlet mole fractions of MBTC and water vapor held constant at values of 1.0 and 1.9%, respectively. For both cases, a slight improvement in the SnO_2 deposition rate and reactant utilization was obtained by increasing either the inlet temperature or the inlet flow rate.

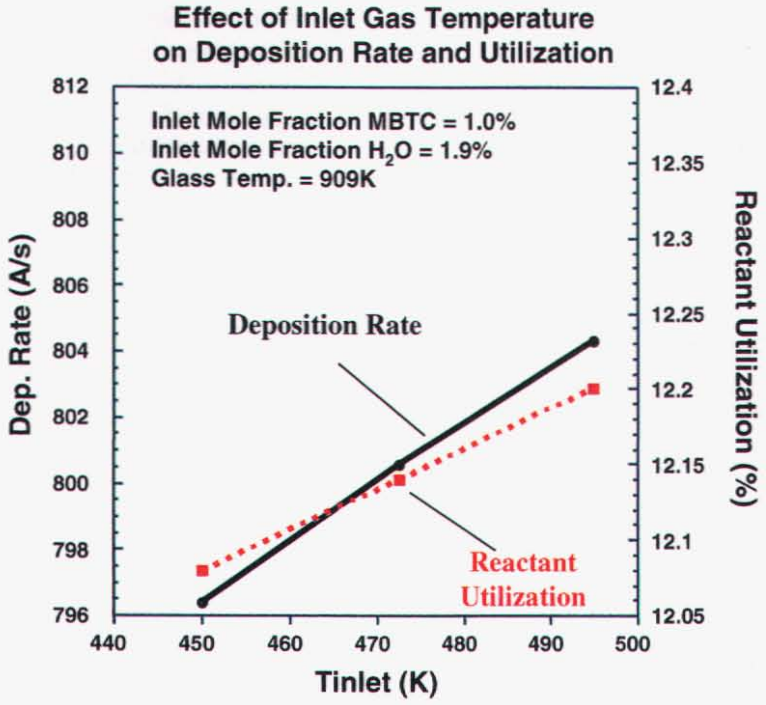

Figure 6-11. Effect of inlet reactant gas temperature on SnO_2 deposition rate and MBTC reactant utilization.

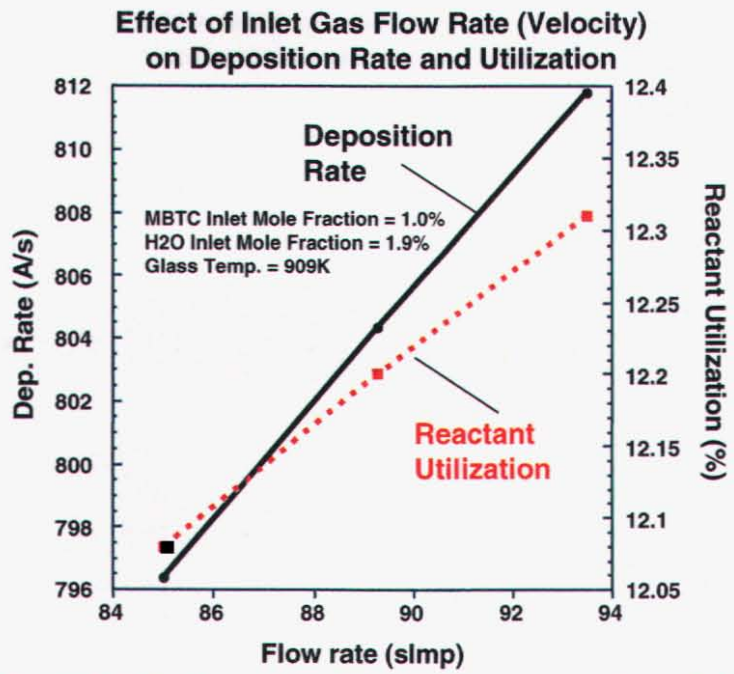

Figure 6-12. Effect of inlet reactant gas flow rate on SnO_2 deposition rate and MBTC reactant utilization.

The effect of varying the coater top wall temperature is shown in Figure 6-13. The coater top wall temperature was varied between its nominal value of 550 K and a value of 605 K while holding the other coater operating conditions constant. Figure 6-13 indicates that changing the coater top wall temperature has only a small effect on coater performance.

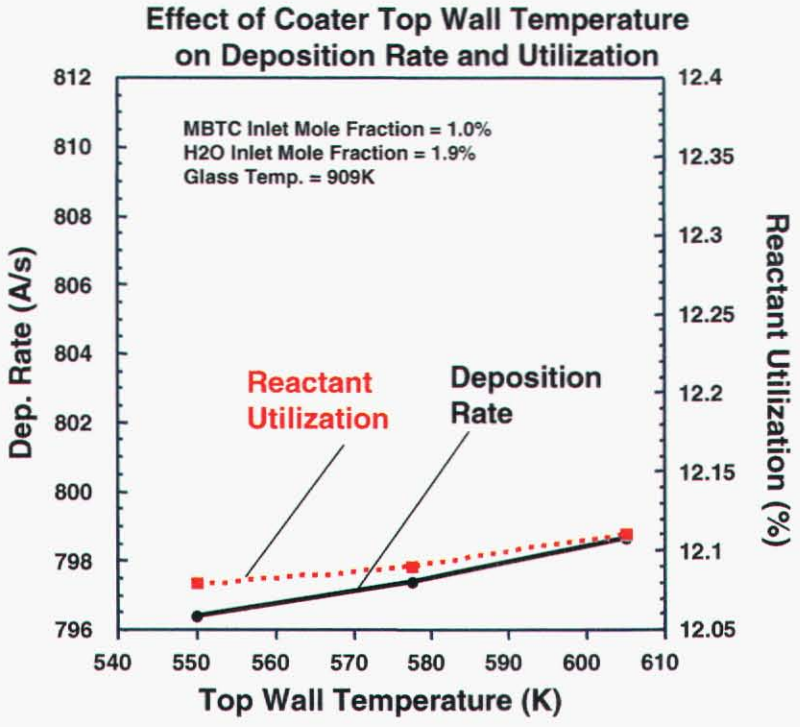

Figure 6-13. Effect of coater top wall temperature on SnO_2 deposition rate and MBTC reactant utilization.

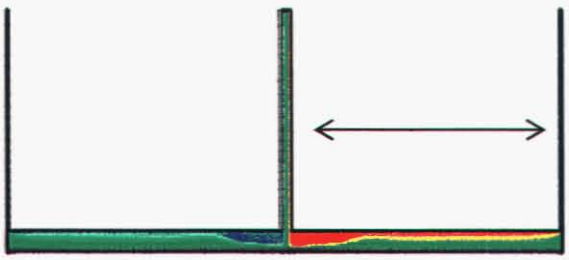

Figure 6-14. Sketch coater geometry showing how the position between the gas inlet and outlet sections was altered.

Finally, the effect of altering the coater geometry was assessed by changing the distance between the inlet and outlet sections, L1, as shown in the coater sketch in Figure 6-14. The distance was increased from its nominal value of 6.64 cm by 50% to a value of 9.96 cm and then increased again by 100% to a value of 13.28 cm. Figure 6-15 shows that increasing the spacing between the coater inlet and outlet from 6.64 to 13.28 cm dramatically increased reactant utilization from approximately 12 to 22% while coater deposition rate decreased only slightly from 797 to 727 Å/s.

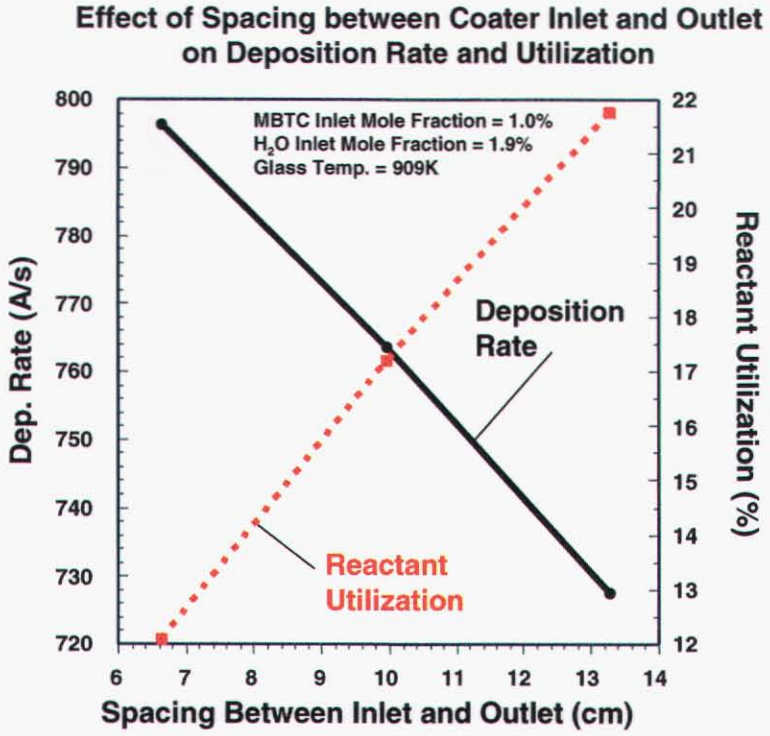

Figure 6-15. Effect of changing spacing between coater inlet and outlet on deposition rate and reactant utilization.

6.2 Summary and Conclusions

A chemically reacting flow model of the PPG glass coater was developed using a global chemical reaction mechanism for the deposition of SnO_2 based on a gas-phase precursor and sticking coefficient surface reaction mechanism. Predictions from the model are in good agreement with deposition data from the PPG pilot coater (averaged over the length of the glass plate) for the deposition of SnO_2 from MBTC and air and also in the case where water vapor (MBTC + air + water) is added to the inlet reactant gas stream to increase the SnO_2 deposition rate.

A parameter study was performed with the validated model to identify ways of improving the performance of the coater. Based on the results of the modeling studies, higher glass temperatures were found to produce higher reactant utilization. Increasing the glass temperature from 870 to 933 K increased reactant utilization from 9.3 to 13.3%, or a factor of approximately 1.43.

Increasing water vapor concentration in the reactant gas inlet stream from 0.7 to 3.0% mole fraction was found to increase reactant utilization from approximately 6.0 to 13% while increasing deposition rate from 500 Å/s to approximately 720 Å/s. Increasing the inlet water vapor mole fraction beyond 3.0% made only a small improvement in reactant utilization and deposition rate. Increasing inlet MBTC mole fraction from 0.4 to 1.0% had only a small effect on reactant utilization but was found to increase deposition rate from approximately 320 to 800 Å/s.

Finally, increasing the spacing between the coater inlet and outlet from a value of 6.64 to 13.28 cm increased reactant utilization from approximately 12 to 22%, or a factor of approximately 1.83.

6.3 References

1. W.S. Winters, G.H. Evans, and C.D. Moen, "CURRENT—A Computer Code for Modeling Two-Dimensional, Chemically Reacting, Low Mach Number Flows," Sandia Report SAND97-8282, Sandia National Laboratories, Livermore, CA, October, 1996.
2. R.J. Kee, F.M. Rubley, E. Meeks, and J.A. Miller, "Chemkin-III: A Fortran Chemical Kinetics Package for the Analysis of Gas Phase Chemical and Plasma Kinetics," Sandia Report SAND96-8216, Sandia National Laboratories, Livermore, CA, May 1996.
3. M.E. Coltrin, R.J. Kee, F.M. Rupley, and Ellen Meeks, "Surface Chemkin-III: A Fortran Package for Analyzing Heterogeneous Chemical Kinetics at a Solid-Surface-Gas-Phase Interface," Sandia Report SAND96-8217, Sandia National Laboratories, Livermore, CA, May 1996.
4. A.M.B. Van Mol, "Chemical Vapour Deposition of Tin Oxide Thin Films," PhD Thesis, TNO, The Netherlands, 2003.
5. J.F. Sopko and J.M. Aaron, "Pilot Coater Data received from John Sopko, PPG Industries," 2002.

Chapter 7 Computational Fluid Dynamics Modeling*

7.1 Introduction

As discussed in Chapter 1, while APCVD is a cost-effective method for on-line coating on glass [1], improvements in process efficiency are expected to result in reduced solid waste generation and disposal, lower raw materials usage, and a reduction in energy consumption. Therefore, significant drivers exist for developing the fundamental understanding of the APCVD process that will lead to an increase in the process efficiency [2].

Generally speaking, the rate and efficiency of APCVD are dependent on reaction kinetics, fluid flow, heat transport, and mass transport in the coating zone. An in-depth understanding of such a reaction-transport process requires high-fidelity computational fluid dynamics (CFD) models that are able to precisely capture the flow, thermal and kinetic phenomena. Representative examples in this area include simulation of SnO_2 deposition from $SnCl_4$ in a horizontal cold wall APCVD reactor [3], computational modeling of silicon deposition from SiH_4 in a stagnation rotating disk APCVD reactor [4], and numerical analysis of TiO_2 deposition from titanium tetra-iso-propoxide in a cold wall impinging APCVD reactor [5].The numerical simulation based on CFD is able to provide quantitative information of flow behavior and species transport, but typically relies to a large extent on the thermodynamic data, reaction mechanism, and transport properties.

Monobutyltin trichloride (or MBTC) used for SnO_2 deposition in the glass industry, which is of interest in the current work, has very limited data reported in the literature [6, 7, 8, 9, 10, 11]. While it is experimentally shown that the reaction of MBTC with oxygen is accelerated in the presence of water, the function of water in the decomposition and/or oxidation of MBTC is not fully understood.

To study this deposition process using CFD, it is very important to note that the deposition rate in the on-line APCVD coating on glass should exceed 20 nm/sec in order to meet the thickness requirement of the coated material on the high line speed glass ribbon [12]. Such a high deposition rate as well as the experimental observation of the wave shape deposition profile (per Section 7.4.2) implies that the deposition process of SnO_2 from MBTC might be mainly limited by the flow behavior as well as mass transport in the coating zone and that the effect of reaction kinetics is less important. This assumption is further substantiated by the experimental measurement of tin oxide deposition rate at different temperatures [7,8]. As a result, the CFD modeling of online APCVD coating on glass can be done with reasonable accuracy without a highly developed reaction mechanism and kinetic data.

The objective of this chapter is to provide a computational framework for SnO_2 deposition from MBTC. The current model is developed using CFD with an impinging flow geometry, and explicitly accounts for homogenous reaction in the gas phase, heterogeneous reaction on the glass surface, thermal effect of the impinging jet on the glass, and impinging flow characteristics in the confined coating zone. The reaction kinetics are based on modeling of deposition rates measured in a stagnation-flow reactor [7,13]; certain kinetic parameters were modified to fit the experimental data. A comparison of CFD model predictions with experimental measurements shows that the experimentally observed spatial distribution in the deposition rate profile is successfully captured by the model. Especially, the observed wave shape in the deposition profile can be explained with boundary layer separation. Based on this model, parametric

* The text in this chapter was originally published in the paper, M. Li, J. F. Sopko, and J. W. McCamy, "Computational fluid dynamics modeling of tin oxide deposition in an impinging chemical vapor deposition reactor", *Thin Solid Films*, in press, 2006.

analysis is performed to study the effect of reactor-substrate spacing and glass line speed on the deposition profile.

7.2 Experimental Details

The experiments of tin oxide deposition from MBTC are conducted in a pilot-scale APCVD reactor with impinging geometry. Figure 7-1 shows a schematic view of the reactor. The MBTC is delivered from a vaporizer with nitrogen as the carrier gas. The water, which is the accelerant for the reaction of MBTC and oxygen, is vaporized using air as the carrier gas. After being mixed with the diluent nitrogen right before APCVD reactor, the MBTC with nitrogen and water with air are sent to the plenum, and then the V shape zone. After passing the coating zone, where SnO_2 is produced and deposited on the surface of the substrate, the remnant reactants and by-products exit the exhausts to be disposed. Two nitrogen curtains are used on each side of the reactor to avoid the reactants and products escaping from the coating zone to the atmosphere. All the inlet and exhaust gas flow rates and temperatures are regulated by Labview process control software. Each inlet or outlet consists of a plenum and a V shaped zone for boundary layer development with distribution holes in between. Different from the industrial manufacturing process, the glass substrate is stagnant in this pilot reactor. The baseline parameters used in the experiment are given in Table 7-1. Under the these operating conditions, the Reynolds number is about 600 in the slot (based on the hydraulic diameter of the slot) and 140 in the coating zone (based on the hydraulic diameter of the coating zone), suggesting laminar flow conditions.

Table 7-1. Reference operating conditions for tin oxide deposition.

N_2 carrier flow rate (slm)	20
N_2 dilute flow rate (slm)	45
N_2 curtain flow rate (slm)	45
Air flow rate (slm)	20
Exhaust flow rate (slm)	95
MBTC concentration (mol%)	0.4
H_2O concentration (mol%)	3
Inlet gas temperature (K)	436
Substrate temperature at the bottom (K)	922
Inlet-exhaust distance (L/B)	25
Reactor-substrate spacing (x/B)	2.5

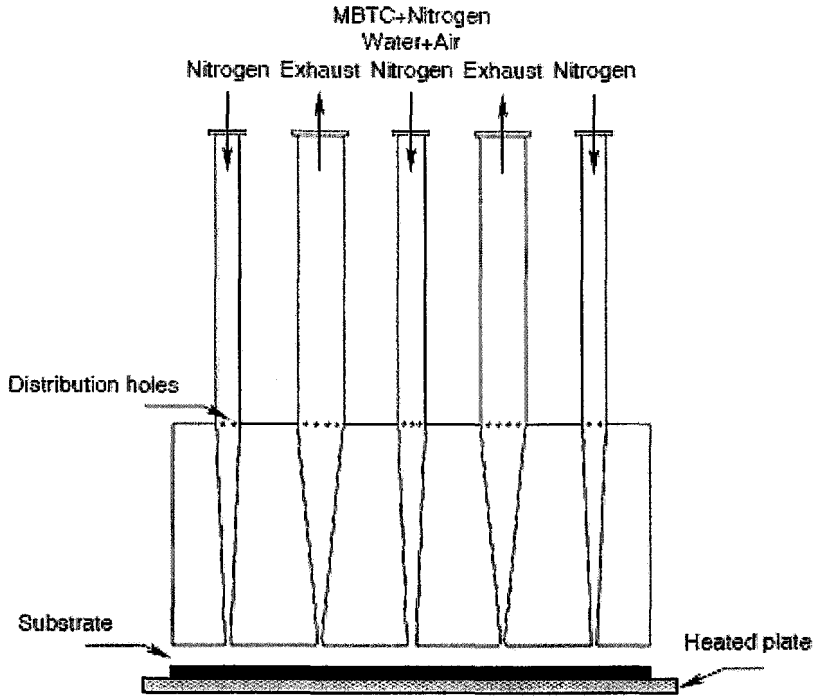

Figure 7-1. Schematic of the pilot-scale APCVD reactor (not to scale).

7.3 CFD Model for Tin Oxide Deposition

The computational domain consists of the V-shaped zone, the coating zone and the substrate (see Figures 7-1 through 7-3). The plenum is not included because its inclusion will not significantly change the profile of the deposition rate. Because the depth of the CVD reactor is several times longer than the inlet-exhaust distance, a two dimensional CFD model is used. The governing equations used to describe the flow dynamics and thermal behavior in the coating zone include continuity, momentum balance, energy balance, species transport, ideal gas law, deposition rate, and coupled heat transfer (listed in Table 7-2). While a simplification of constant surface temperature is commonly used in the numerical simulation of CVD process (e.g., [4,14,15,16]), a conjugate heat transfer between the heating plate below the substrate and the fluid above the substrate will more closely match the experimental arrangement. In the current model, this condition is achieved through coupling of the glass top surface temperature by the convective heat transfer of the impinging jet and the conductive heat transfer within the glass with a fixed temperature at the bottom of the glass. The heat transfer due to radiation is not accounted for in the current model and might be considered in future work. The temperature and concentration distributions are uniform at all inlets (distribution slots). The zero gradient in concentration normal to the surface is specified for all the surfaces except the glass top surface. The pressure outlet boundary conditions are specified at the two exhausts and the two side flows. The pressure in the exhausts is varied slightly such that the calculated flow rates in the exhaust match the experimental conditions. The wall of the reactor is assumed to maintain a constant temperature of 436 K.

Table 7-2. Governing equations in tin oxide deposition.

Continuity:	$\nabla \cdot (\rho \vec{u}) = 0$
Momentum balance:	$\nabla \cdot (\rho \vec{u}\vec{u}) = -\nabla p + \nabla \cdot \left\{ \mu \left[\nabla \vec{u} + (\nabla \vec{u})^T - \frac{2}{3}(\nabla \cdot \vec{u})\mathbf{I} \right] \right\} + \rho \vec{g}$
Energy balance:	$\nabla \cdot (\vec{u}\rho c_p T) = \nabla \cdot (k \nabla T) - \sum_{i=1}^{N} \vec{J}_i \cdot \frac{\nabla H_i}{M_i} - \sum_{i=1}^{N}\sum_{j=1}^{J} H_i \alpha_{ij} R_j^g$
	$\nabla \cdot (k_{glass} \nabla T_{glass}) = 0$
Species transport:	$\nabla \cdot (\rho \vec{u} Y_i) = -\nabla \cdot \vec{J}_i + M_i \sum_j \alpha_{ij}^g R_j^g, i = 1, ..., N$
Ideal gas law:	$\rho = pM_w / RT$
Deposition rate:	$J_i = -D_i \nabla(\rho Y_i) - D_i^T \nabla(\ln T) = R_i^s$
Coupled heat transfer:	$-k \nabla T = -k_{glass} \nabla T_{glass}$

The reaction mechanism is based on modeling of deposition rates measured in a low pressure stagnation-flow reactor [7,13], but we have slightly modified the reaction constant in the surface reaction to fit the experimental data (see Table 7-3). It has been found that the deposition rate predicted by the CFD model with the original mechanism matches well with the experimental measurement far away from the inlet slot but about four times higher underneath the inlet slot (see Figure 7-2). Since the original mechanism is in good agreement with experimental data obtained under low pressure, we postulate that this discrepancy might be due to the significant difference in pressure or other unknown reasons. In this reaction mechanism, the MBTC–H_2O complex is formed rapidly as the two species are mixed together, and the MBTC–H_2O complex reacts with oxygen to form SnO_2 on the high temperature glass surface.

Table 7-3. Reaction mechanism of tin oxide deposition from MBTC [13].

gas phase:	$C_4H_9SnCl_3 + H_2O \rightarrow C_4H_9SnCl_3(H_2O)$, $C_4H_9SnCl_3]^{0.72}$
	$k_0 = 10^8$ (based on *mol-m-sec*), $Ea = 4.18 \times 10^4$ *J/mol*
surface:	$C_4H_9SnCl_3(H_2O) + OS\ (s) \rightarrow C_4H_9SnCl_3(H_2O)(s)$, Sticking coefficient =1
	$C_4H_9SnCl_3(H_2O)(s) + 0.5O_2 \rightarrow SnO_2(B) + 2C_2H_4 + 3HCl + OS(s)$, $[O_2]^{0.76}$
	$k_0 = 1.6 \times 10^4$ (based on *mol-m-sec*) *, $Ea = 5.73 \times 10^4$J/mol

* modified pre-exponential factor.

The thermodynamic data of MBTC and MBTC–H_2O complex are taken from Sandia National Laboratories (see www.ca.sandia.gov/HiTempThermo) [17]. The calculation of heat capacity, viscosity, and thermal conductivity of the mixture is based on the property of pure nitrogen. This is because the nitrogen gas is in excess of 90% in this particular case and the estimation of these properties of MBTC and MBTC–H_2O complex is avoided. The same approach was employed to model the tin oxide CVD from dimethyltin dichloride [9]. The mass diffusivity of each species is estimated based on kinetic theory, and the Lennard–Jones parameters of each species are given in Table 7-4.

The process model is implemented into Fluent, a commercial CFD computer program, and is solved by the finite volume method. The governing mass, momentum, and energy balance equations together with the species transport equations are solved first using the first-order upwind scheme to obtain a convergent solution and then the second-order upwind scheme to precisely capture the flow characteristics. Generally it requires about 300 iterative steps to reduce the residuals of all the variables to 10^{-5} for the first-order upwind scheme and additional hundreds of steps for the second-order upwind scheme in each simulation run.

Table 7-4. Lennard-Jones parameters of the chemical species.

Chemical species	σ (Å)	ε/k (K)	Reference
C_2H_4	3.971	280.8	
$C_4H_9SnCl_3$	5.5	528.069	[17]
$C_4H_{11}SnCl_3O$	4.5525	549.78	[17]
H_2O	2.605	572.4	
N_2	3.621	97.53	
O_2	3.458	107.4	
SnO_2	4.534	586.983	

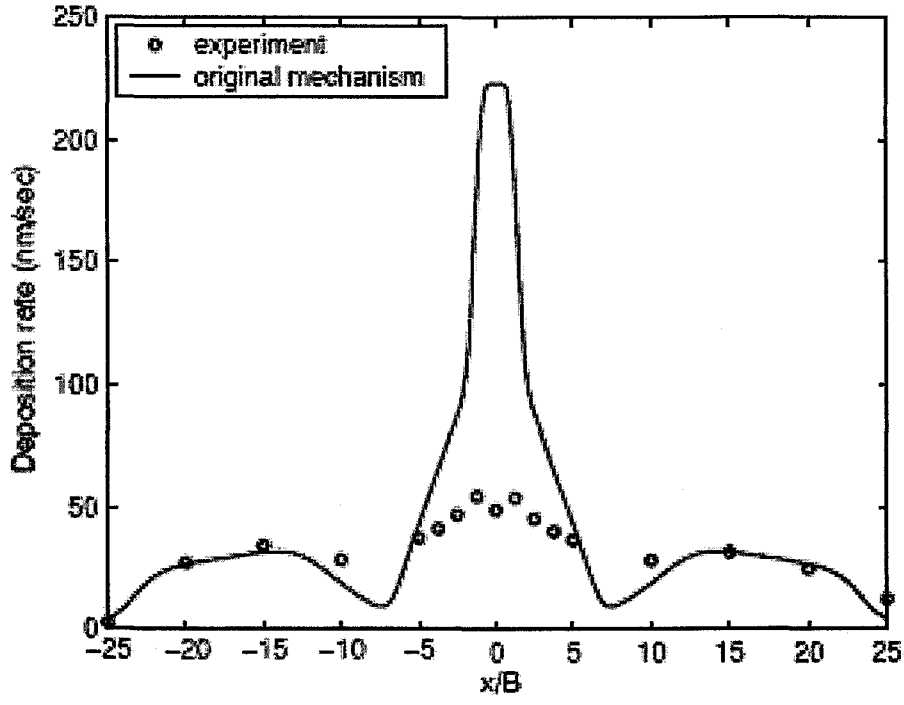

Figure 7-2. Deposition profile obtained using the original mechanism.

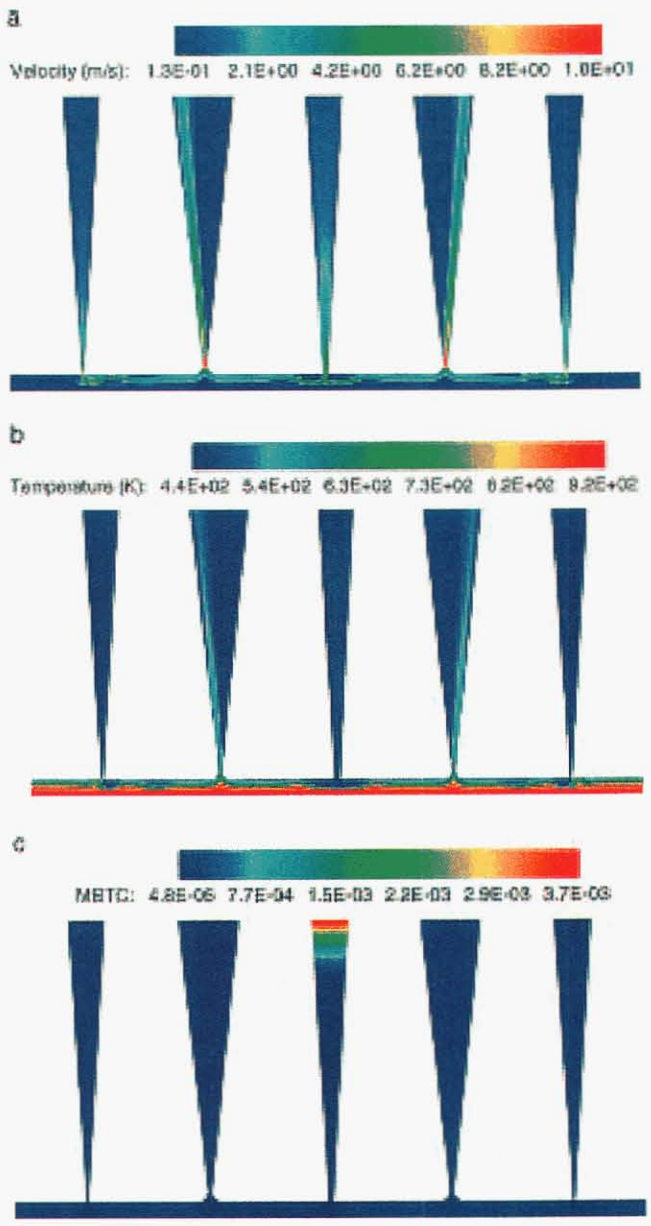

(Figure continued on next page)

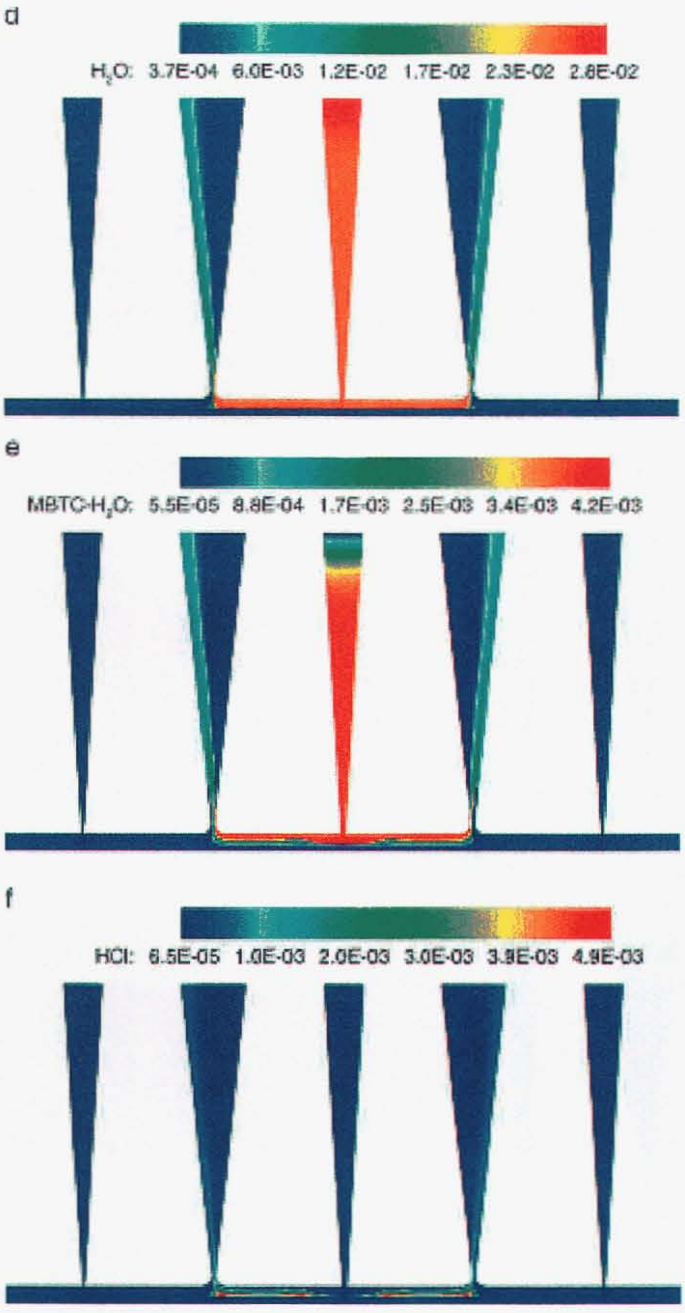

Figure 7-3. Contours of velocity, temperature, MBTC, H_2O, MBTC-H_2O complex and HCl under reference operating conditions, solved using the second order upwind scheme.

7.4 Results and Discussions

7.4.1 Modeling Results under Baseline Operating Conditions

The simulated contours of velocity, temperature and mole fractions of MBTC, H_2O, MBTC-H_2O complex and HCl in the whole field using the second order upwind scheme under the baseline conditions are shown in Figure 7-3. The flow in the exhaust is not stable due to pressure outlet boundary conditions, as one can see from Figure 7-3 that the exhaust flow is pulling on the wall and it is not symmetric with

respect to the centerline. Better results of the flow in the exhausts are expected when the computational domain is extended to match the experimental conditions. However, the simplification made here will not affect the flow in the coating zone and the deposition rate on the surface, which is of interest in this work. It is shown by the CFD simulation that with the nitrogen curtain flow, all chemicals are well confined in the reactor and escaping from the coating zone to the surrounding atmosphere is avoided. As the vertical velocity is converted to horizontal velocity, there are two recirculation zones formed in the confined coating zone. One is at the corner of the inlet slot and the other is 5–9 slot widths away from the inlet slot. Based on the kinetics of the mechanism used here, the reaction of water with MBTC is so fast that almost all the MBTC is converted to MBTC–H_2O complex immediately as it enters the reactor. On the glass surface, the MBTC–H_2O complex reacts with oxygen to generate SnO_2, which forms the coating layer. The byproduct, HCl, diffuses from the substrate to the gas phase.

The simulated deposition profile of SnO_2 under the baseline operating conditions is shown in Figure 7-4. The CFD simulation successfully captures the wave shape of the deposition profile, and the deviation of average magnitude of the deposition rate is less than 10% of the corresponding experimental value, indicating that the CFD model with modified kinetic parameters reasonably predicts the deposition rate.

Both experiment and simulation confirm that there is a dip in the center of the deposition rate profile (directly underneath the inlet slot). To explain this phenomenon, we first note that under steady state, the surface reaction rate equals the diffusion flux from the gas to the surface, or

$$J = k_s c_s = D\frac{\partial c}{\partial y}|_{y=0} \tag{7-1}$$

where J is the deposition rate, k_s is the surface reaction constant (assuming first order reaction), c_s is the surface concentration, and D is the diffusion coefficient. Note that $J = D\frac{\partial c}{\partial y}|_{y=0}$ instead of $J = -D\frac{\partial c}{\partial y}|_{y=0}$ is used in Eq. 7-1 because the diffusion flux is in the opposite direction of the y coordinate. The diffusion flux can also be expressed as the product of the mass transfer coefficient and the difference in the concentration, or

$$J = D\frac{\partial c}{\partial y}|_{y=0} = h_c(c_0 - c_s) \tag{7-2}$$

where h_c is the mass transfer coefficient, and k_s is the bulk concentration. A combination of Eqs. 7-1 and 7-2 yields

$$J = \frac{c_0}{1/k_s + 1/h_c} \tag{7-3}$$

Depending upon the relative magnitude of k_s and h_c, the process can be either reaction controlled ($k_s \ll h_c$) or diffusion controlled ($k_s \ll h_c$).

It is possible to obtain the surface concentration data from the Fluent code output, then the limited deposition mechanism can be justified by the following equation:

$$\frac{k_s}{h_c} = \frac{c_0}{c_s} - 1 \tag{7-4}$$

The profile of k_s/h_c in the baseline case is shown in Figure 7-5. It is seen that directly underneath the inlet slot, the deposition rate is limited by both surface kinetics and diffusion. Far away from the inlet slot, the deposition is solely diffusion controlled. This explains why the CFD simulation with the original reaction mechanism yields very similar results to the one with the modified reaction mechanism (see Figures 7-2 and 7-4) in the region far away from the inlet slot, where the reaction kinetics is of minimal importance.

The dip in the center of the deposition profile can be readily explained by Eq. 7-1. To explain from $J = D\frac{\partial c}{\partial y}|_{y=0}$, we note that the thermal interaction between the impinging jet and the glass is the largest in the center and the temperature is the lowest underneath the inlet slot on the glass surface. According to kinetic theory, the diffusion coefficient (D) is the lowest in the center. As will be shown later, the temperature variation is about 2.5%, or there is only a slight change in the diffusion coefficient. However, due to the stagnation of the impinging jet directly underneath the inlet, the concentration gradient in the center, is significantly lower than its neighborhood. This can be verified by taking concentration data from the Fluent output and calculating the concentration gradient near the substrate surface. The concentration gradient shown in Figure 7-6 is approximated by the difference of concentration at two adjacent grid points close to the wall divided by the grid size, or $\frac{\partial c}{\partial y}|_{y=0} = \frac{\Delta c}{\Delta y}$. It clearly shows the concentration gradient is lower in the center than its neighborhood. Therefore, $D\frac{\partial c}{\partial y}|_{y=0}$ in smaller in the center, which leads to the dip in the deposition profile. On the other hand, we note that k_s is the smallest in the center due to the lowest surface temperature. However, the surface concentration is the highest in the center and decays in the lateral direction due to the boundary layer development, as shown in Figure 7-7. As a result, there is a dip in the center of the deposition profile ($J = k_s c_s$) if k_s changes sharply around the stagnation point due to temperature variation.

A comparison of the CFD simulation with the first order and second order upwind schemes shows that although the secondary shapes are not captured by the former scheme, the relative difference in the average deposition rate is less than 4% with these two numerical schemes (see Figure 7-8). This implies that the first order upwind scheme is able to provide a very good estimate of the average deposition rate. A plot of the local deposition rate obtained by the first order upwind scheme as a function of the lateral position shown in Figure 7-9 indicates that in the region of $2 \le x/B \le 22$ (the inlet exhaust length is 25B), the local deposition rate is proportional to $x^{-0.46}$, which is very close to the theoretical relationship $x^{-0.5}$ predicted by the parallel plate mass transfer boundary theory [18]. This fact further substantiates the conclusion that this deposition process is mainly diffusion controlled.

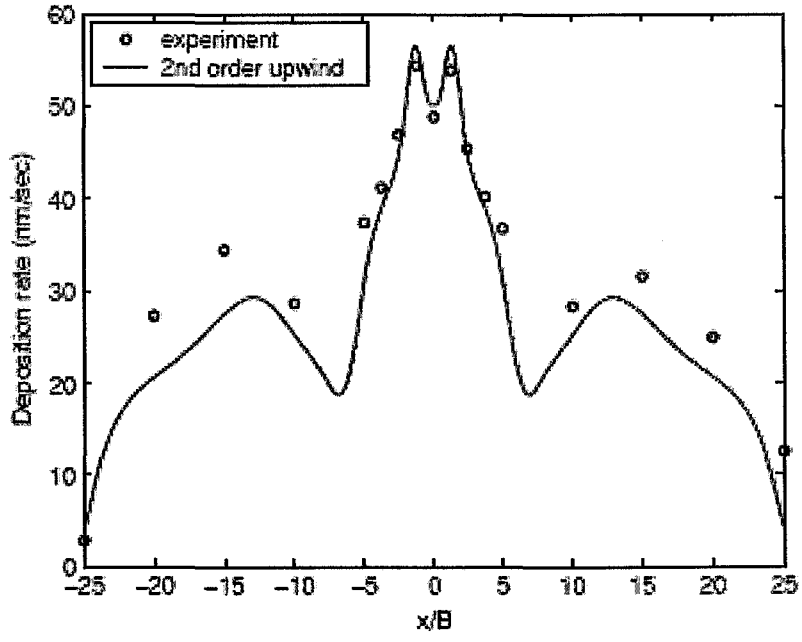

Figure 7-4. Comparison of deposition rate profile simulated using the second-order upwind scheme with experimental data measured at the reference operating conditions.

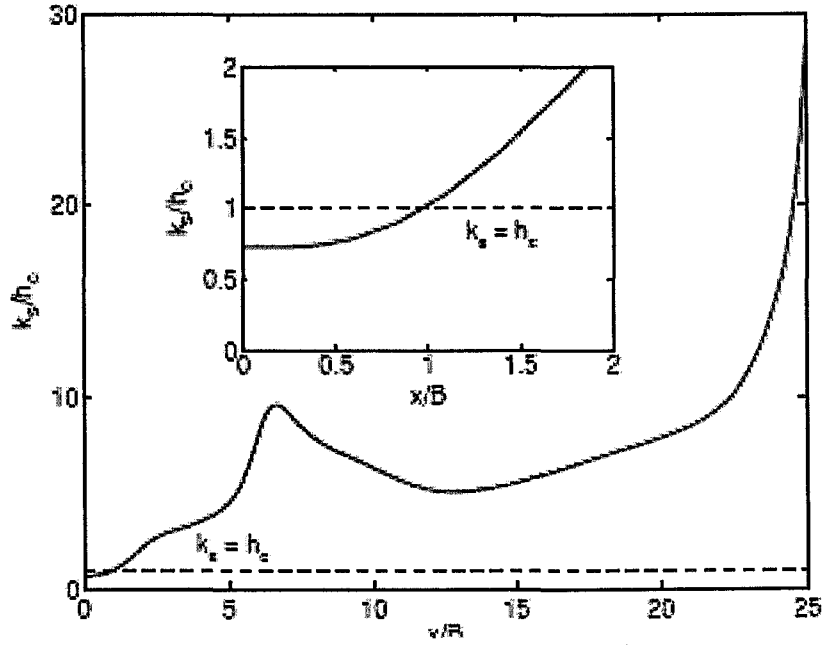

Figure 7-5. Ratio of reaction constant to mass transfer coefficient.

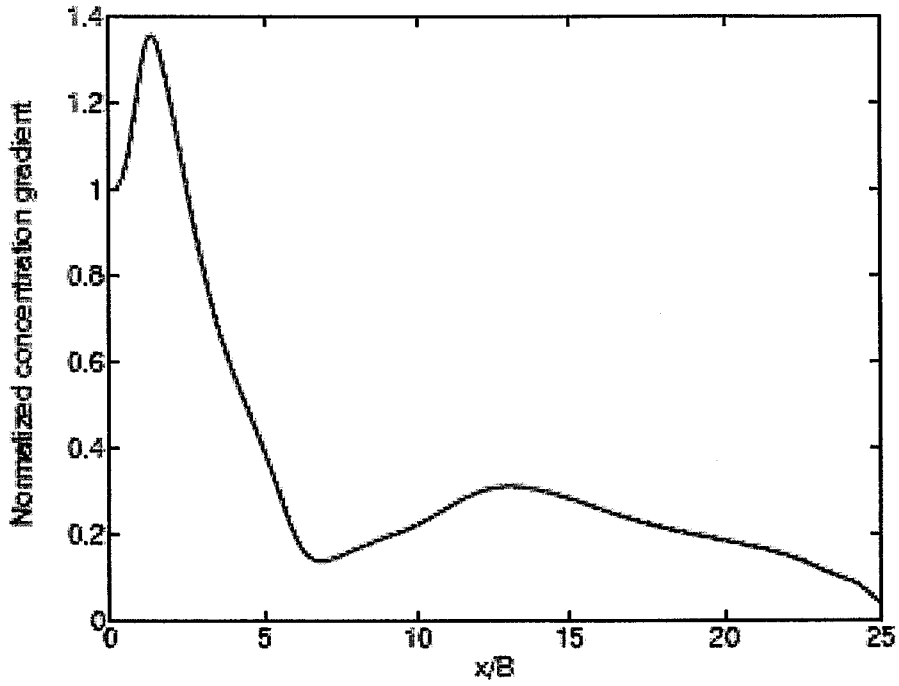

Figure 7-6. Normalized concentration gradient of MBTC-H_2O complex on the surface.

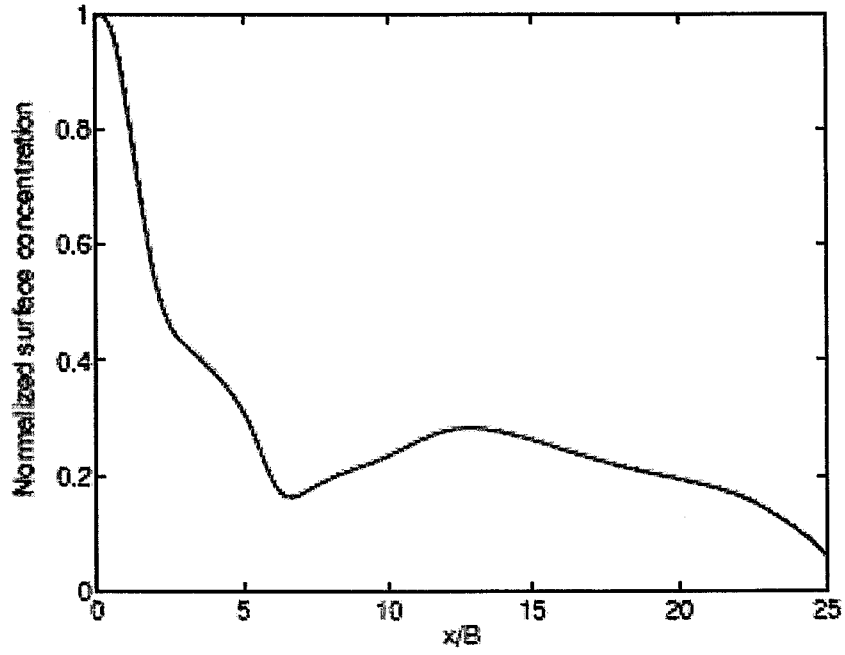

Figure 7-7. Normalized concentration of MBTC-H_2O complex on the surface.

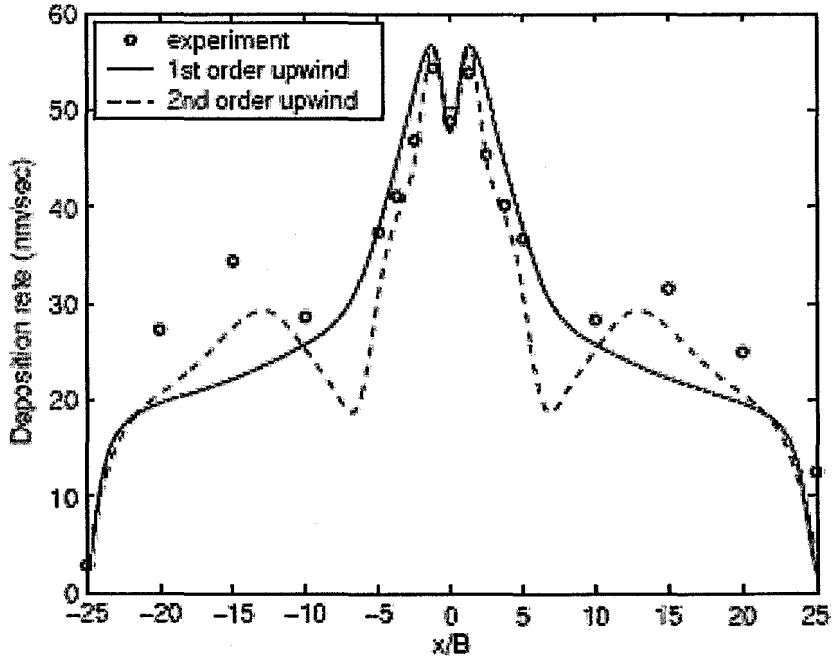

Figure 7-8. Comparison of deposition rate profile simulated using different numerical schemes.

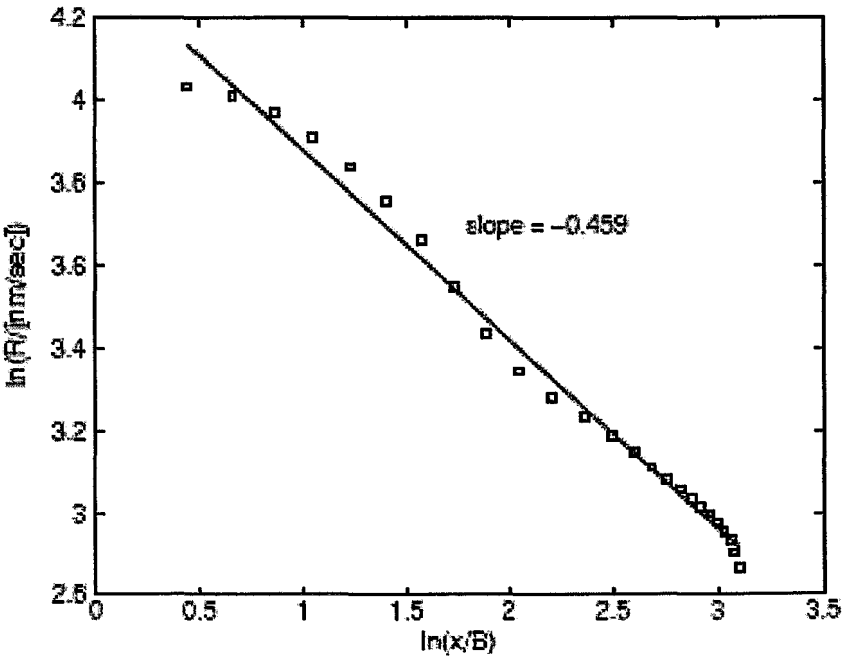

Figure 7-9. Deposition rate profile obtained using CFD simulation with first-order upwind scheme.

7.4.2 Influence of Reactor-Substrate Spacing on the Deposition Rate Profile

The deposition profile under reduced reactor-substrate spacing (slot to glass distance) is shown in Figure 7-10. The CFD simulation successfully captures the deposition rate at each of the measurement points, except for the one in the center. Note that there is also a dip in the deposition profile obtained from the CFD simulation, although it is hard to tell from Figure 7-10. The average deviation of model prediction at each measurement point from the experimental measurement is only 9.8%, and the error of the cumulative deposition rate from modeling accounts for less than 6% of the corresponding experimental value, indicating that the CFD model with modified kinetic parameters reasonably predicts the deposition rate.

The deposition profile is dependent on the reactor-substrate spacing, similar to what is observed in heat transfer in the impinging flow geometry [19,20]. The difference in the deposition profile occurs in several regions (see Figure 7-11). One is directly underneath the inlet slot. This might be caused by a smaller recirculation region in the vicinity of the inlet slot when the reactor–substrate spacing is reduced. Another region is located at 5–9 slot widths away from the inlet (see Figure 7-12), which can be readily explained by boundary layer separation [21]. The boundary layer tends to separate from the surface of the substrate under sufficient increasing fluid pressure downstream of the flow, known as adverse pressure gradient. When the pressure gradient is large enough such that the shear stress reduces to zero, the separation occurs and the fluid is no longer pulling on the wall, and opposite flow develops to push the boundary layer off of the solid surface. The boundary layer separation is alleviated as the flow area decreases. Another region is close to the exhaust, when the flow is well developed. Since the velocity parallel to the glass increases as a result of decreased flow area, the boundary layer for mass transfer ($\delta_c \propto x/\sqrt{\mathrm{Re}_x} \propto \sqrt{\nu x/u}$) decreases and the deposition is enhanced [18].

It is worth pointing out that the wavy flow pattern due to buoyancy induced convection in CVD processes has also been reported in the literature (e.g., [15, 22, 23]). In the current work, the Rayleigh number is around 300, and the mixed convection parameter Ra/Re^2Pr in the coating zone is on the order of 10^{-2}, implying that the buoyancy induced convection is minimal. A comparison of CFD modeling with and without natural convection shows that the influence of buoyancy has no differentiable effect on the flow pattern or the deposition profile. Moreover, similar dips and humps were also observed in the heat transfer coefficient of turbulent impinging jet by Gardon and Akfirat [19, 20]. However, these secondary shapes were explained with a transition of laminar to turbulent boundary layer in the vicinity of $x/B \approx 7$.

The surface temperature under different reactor–substrate spacing is shown in Figure 7-13. In either case, the temperature is the lowest in the center, which indicates that the thermal interaction between the impinging jet and the glass is the largest. Far away from the inlet, conduction from the depth of the glass allows the surface temperature to recover to a higher temperature at the gas glass interface. This phenomenon partially explains the dip in the deposition profile. Note that the heat transfer due to radiation is not accounted for in the current work; the substrate temperature might be overestimated. Based on the convective heat transfer coefficient from the Fluent output, it is possible to estimate the relative importance of the convective heat transfer Jcov/A and radiative heat transfer Jra_d/A, which is not accounted for in the current work; it is shown that the radiative heat transfer is dominant $1.5 \le x/B \le 25$ from the inlet slot, while the convective heat transfer is dominant directly underneath the inlet slot ($x/B < 1.5$). Therefore, even though the surface temperature is overestimated far away from the inlet slot, the surface temperature directly underneath the inlet slot (where the dip occurs) is reasonably described by coupling of the convective heat transfer of the impinging jet and the conductive heat transfer within the glass.

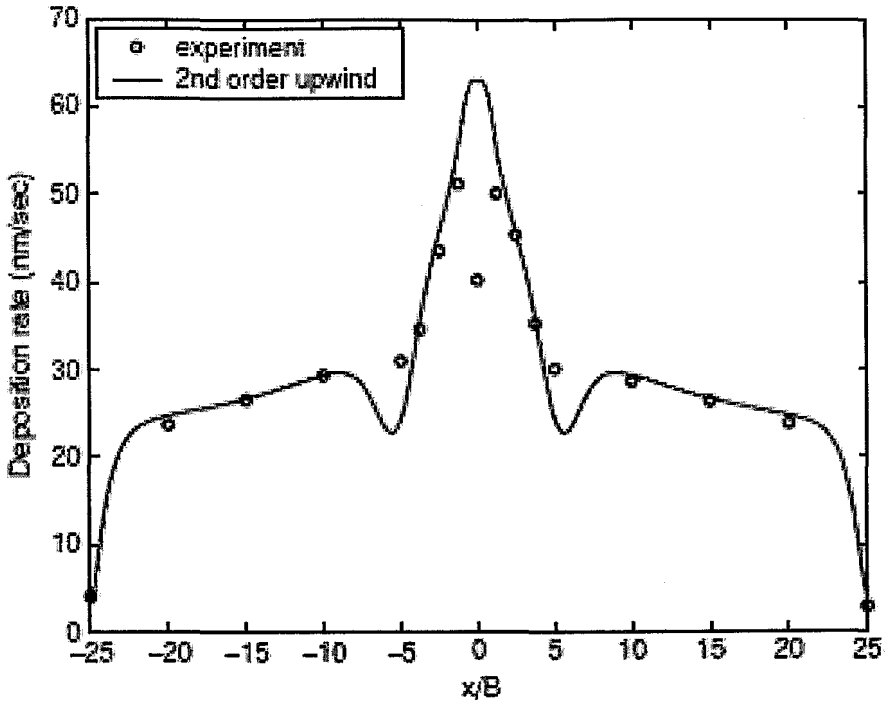

Figure 7-10. Comparison of deposition rate profile simulated using the second-order upwind scheme with experimental data measured at reduced reactor-substrate spacing (H/B=1.5).

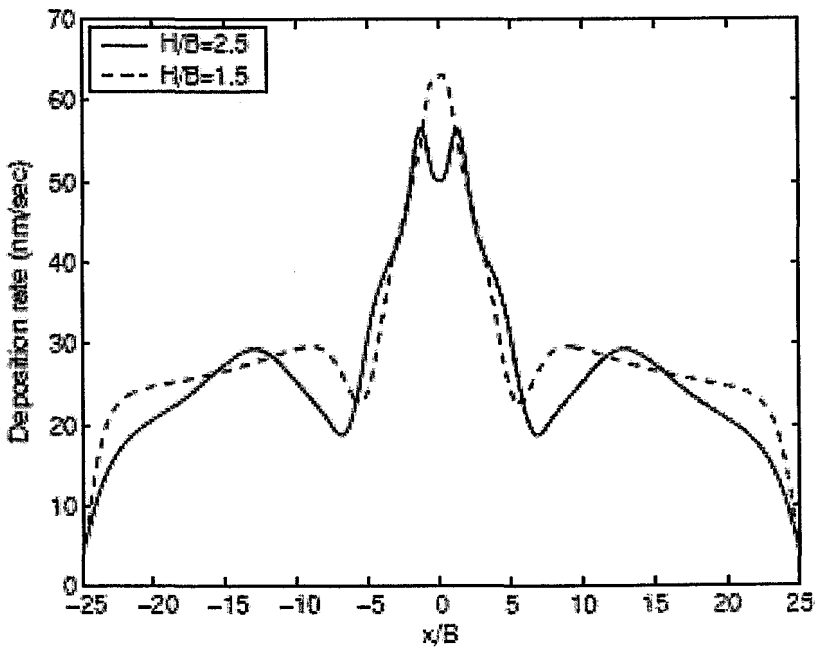

Figure 7-11. Influence of reactor-substrate spacing on the deposition rate profile.

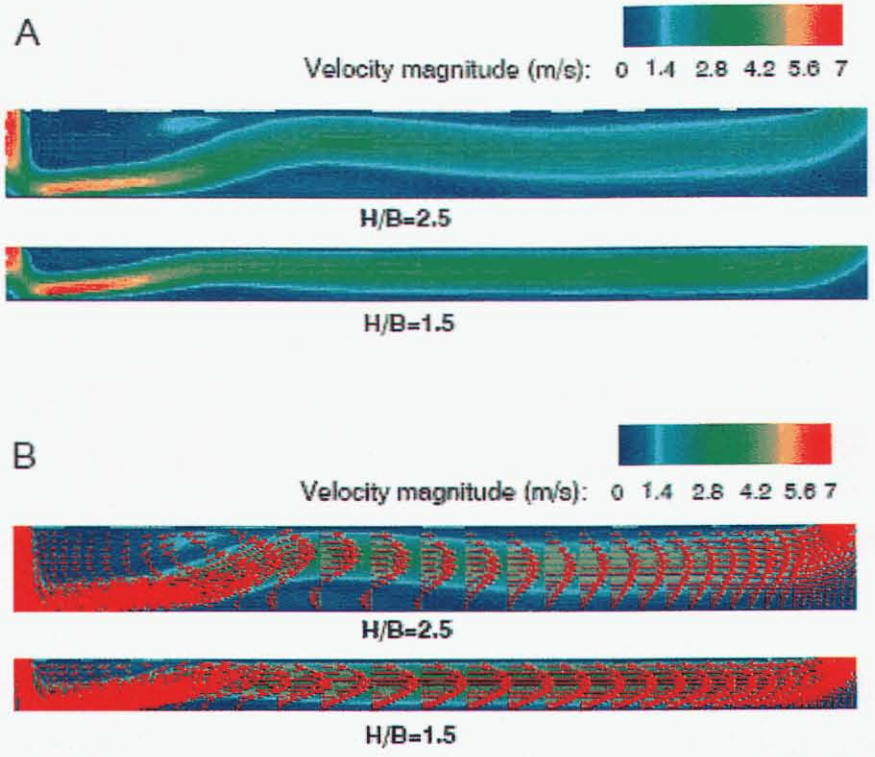

Figure 7-12. Influence of reactor-substrate spacing on the velocity flow field.

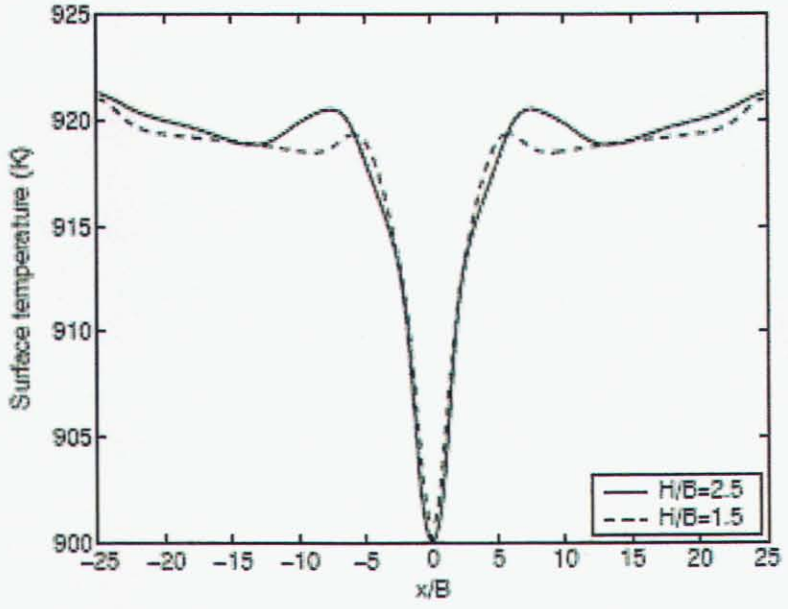

Figure 7-13. Influence of reactor-substrate spacing on the substrate surface temperature.

7.4.3 Influence of Line Speed on the Deposition Rate Profile

All the previous simulations are based on the stagnation geometry. However, in the manufacturing process, the glass is moving with a line speed of around 0.1–0.2 m/s, which implies that the moving boundary conditions may need to be applied on the glass surface. At high line speeds, when moving boundary condition is applied, it is found that the velocity field is no longer symmetric. Instead, the flow is more towards downstream of the inlet slot than upstream, as shown in Figure 7-14. As a result of the asymmetric flow, the deposition rate is higher downstream of the inlet slot than upstream, as shown in Figure 7-15. The effect of the moving glass on the deposition rate profile is more apparent as the line speed becomes very fast. Under typical line speeds, however, this drag experienced by the flow is generally negligible.

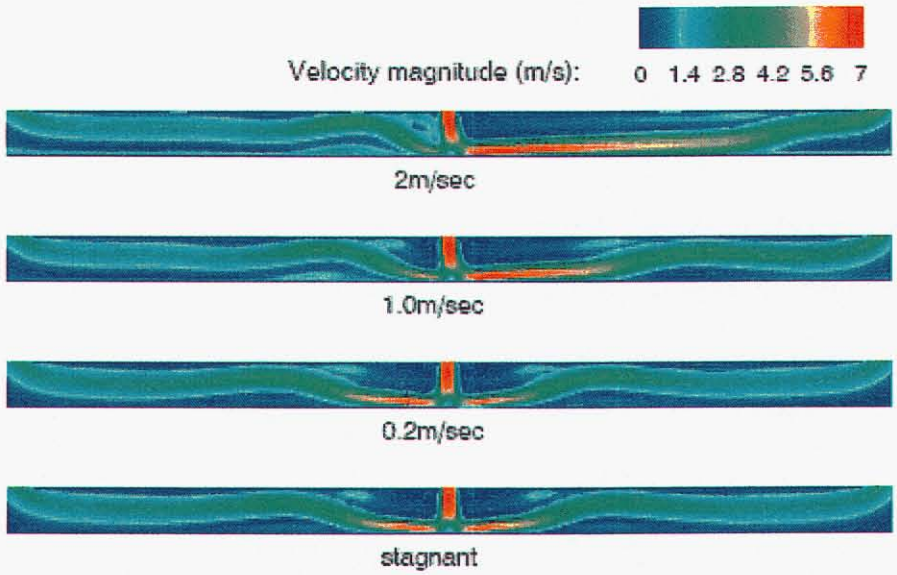

Figure 7-14. Influence of glass line speed on the velocity flow field.

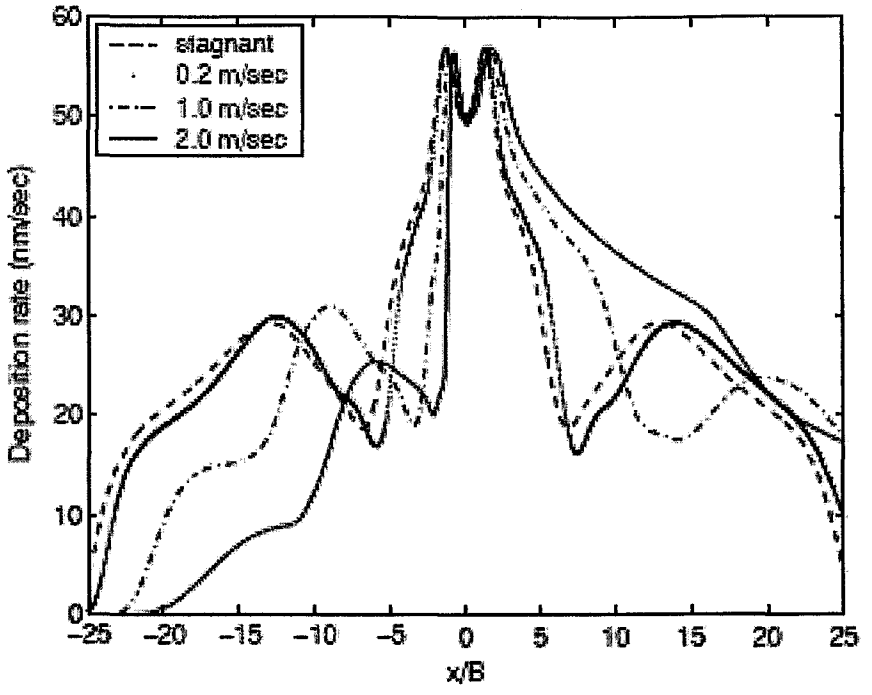

Figure 7-15. Influence of glass moving speed on the deposition rate profile.

7.4.4 Discussions on the Current Reaction Mechanism

It is worth pointing out that when the oxygen is in excess, ethylene might be oxidized to carbon monoxide and carbon dioxide. However, no difference is found in the deposition rate profile after this modification is made. Therefore, from a viewpoint of deposition rate, either mechanism is acceptable. However, the tin oxide deposition is shown to shift from a reaction controlled deposition mechanism to a diffusion controlled deposition mechanism in the presence of adequate amount of water, which implies that a further increase in the surface reaction by increasing water concentration will not result in an increase in the deposition rate if it is diffusion controlled. A tentative explanation for this phenomenon is that the water vapor might not only reduce the activation energy for the surface reaction, but also break the Sn–Cl bonds in MBTC to form products with smaller molecular weight and molecular size (similar to the water–$SnCl_4$ system). See Sections 2.5 and 3.3.2. The higher the water/MBTC ratio, the smaller the product molecule and the larger the diffusion flux to the substrate. This mechanism might partially explain the function of water in the tin oxide deposition and might be tested in future work.

7.5 Conclusions

This chapter provides a computational framework for the APCVD of SnO_2 with MBTC as the precursor. It is shown that the deposition process is mainly diffusion controlled and the effect of reaction kinetics is less important. The wave shape in the deposition profile is due to the several stagnation/recirculation regions in the coating zone.

7.6 References

1. R. Gordon, *J. Non-Cryst. Solids.* 218 (1997) 81.
2. M.D. Allendorf, *Thin Solid Films.* 392 (2001) 155.
3. T.C. Xenidou, A.G. Boudouvis, D.M. Tsamakis, N.C. Markatos, *J. Electrochem. Soc.* 151 (2004) C757.
4. C.R. Kleijn, *Thin Solid Films.* 365 (2000) 294.
5. S.A. Gokoglu, G.D. Stewart, J. Collins, and D.E. Rosner, in: S.B. Desu, D.B. Beach, B.W. Wessels, S. Gokoglu (Ed.), *Material Research Society Symposium Proceedings.* 335 (1994) 171.
6. J.L. Buchanan, C. McKown, *J. Non-Cryst. Solids.* 218 (1997) 179.
7. Y. Chae, W.G. Houf, A.H. McDaniel, J. Troup, M.D. Allendorf, *J. Electrochem. Soc.* 151 (2004) C527.
8. S.M. Lee, D.L. Kim, H.J. Youn, K.S. Hong, *Jpn. J. Appl. Phys.* 39 (2000) 407.
9. A.M.B. Van Mol, PhD, *Eindhoven University of Technology*, The Netherlands, 2003.
10. A.M.B. van Mol; Y. Chae; A.H. McDaniel; M.D. Allendorf, "Chemical vapor deposition of tin oxide: Fundamentals and applications," *Thin Solid Films*, 502 (2006), 72.
11. M.D. Allendorf, A.M.B. Van Mol, *Top. Organomet. Chem.* 9 (2005) 1.
12. R.J. McCurdy, *Thin Solid Films.* 351 (1999) 66.
13. Y. Chae, W. G. Houf, A. H. McDaniel, M. D. Allendorf, "Mechanisms for the Chemical Vapor Deposition of Tin Oxide from Monobutyltintrichloride," *J. Electrochem. Soc.*, 153 (2006), C309.
14. A. Ern, V. Giovangigli, M. D. Smooke, *J. Cryst. Growth.* 180 (1997) 670.
15. G. Luo, S.P. Vanka, N. Glumac, *Int. J. Heat Mass Transf.* 47 (2004) 4979.
16. Z. Yuan, S. Mokhtari, A. Ferdinand, J. Eakin, L. Bartholomew, *Thin Solid Films.* 290/291 (1996) 422.
17. M.D. Allendorf, C.F. Melius, *J Phys Chem A.* 109 (2005), 4939
18. R.B. Bird, W.E. Stewart, E.N. Lightfoot, *Transport Phenomena*, John Wiley & Sons, New York, 1960.
19. R. Gardon, J.C. Akfirat, *Int. J. Heat Mass Transf.* 8 (1965) 1261.
20. R. Gardon, J.C. Akfirat, *J. Heat Transf.* 88 (1966) 101.
21. H. Schlichting, K. Gersten, *Boundary Layer Theory.* Springer, Berlin, Germany, 2000.
22. H. Van Santen, C.R. Kleijn, H. E .A. Van Den Akker, *Int. J. Heat Mass Transf.* 43 (2000) 1523.
23. H. Van Santen, C.R. Kleijn, H. E. A. Van Den Akker, *Int. J. Heat Mass Transf.* 43 (2000) 1537.

Chapter 8 Chemical Additives[†]

8.1 Introduction

One strategy for increasing deposition rates in APCVD is to identify additives that can speed up the chemistry, either by initiating gas-phase reactions to accelerate precursor decomposition and form more reactive species, or by accelerating (perhaps catalytically) surface processes.

In the case of tin oxide, the scientific literature does not contain much information regarding the effect of chemical additives other than water vapor, which is well known to increase growth rates from several precursors [1,2]. However, there are several patents claiming the use of a broad range of "accelerants," including Lewis acids and bases, water, a broad range of Group V compounds, and ozone(O_3) [3,4]. The last molecule would appear to be a promising additive, since it has been shown to accelerate the growth of silicon dioxide films from tetraethoxyorthosilane (TEOS) [5,6]. In that case, O3 dissociates to form oxygen atoms in the gas phase at CVD temperatures. Subsequent reactions with the precursor and other hydrogen sources lead to additional radicals such H and OH:

$$O_3 + M \leftrightarrow O_2 + O + M \qquad \Delta H°_R = 25.5 \text{ kcal/mol} \tag{8-1}$$

$$O + RH \leftrightarrow OH + R \tag{8-2}$$

$$O + H_2 \leftrightarrow OH + H \tag{8-3}$$

The radicals formed by these reactions can attack organic groups on the precursor and initiate decomposition at temperatures below those required for pyrolysis (i.e., unimolecular decomposition). In the case of TEOS, this leads to organosilicon species that are more reactive with the surface than the original precursor. C–H bond energies in main-group organometallic compounds are largely independent of the identity of the central metal atom, suggesting that exposing organotin compounds to O_3 prior to deposition will also increase the growth rate. However, no experiments have been reported to confirm this assumption.

One of the precursors most widely used to deposit tin oxide is monobutyltin-trichloride ($C_4H_9SnCl_3$; MBTC). The industrial importance of this compound makes it a good candidate for exploring the potential of additives to increase deposition rates. Additives could also improve the efficiency of reactant utilization, which can be as low as 10% in some cases. We recently reported experimental results [7] and models [2,8,9] showing that deposition from MBTC can be controlled by either surface kinetics or mass transport, depending on temperature and whether or not water is present as a reactant. Thus, compounds such as ozone provide a way to probe the deposition chemistry by initiating reactions that would not occur otherwise.

In this chapter, we describe the effect of ozone addition on SnO_2 growth rates from MBTC. Growth rates were obtained from a stagnation-flow reactor (SFR), which simplifies kinetic measurements by yielding uniform growth rates across the substrate. This geometry also allows detailed chemical mechanisms to be employed in simulating the growth process, since it can be modeled as a one-dimensional system under appropriate operating conditions. Growth rates were measured for conditions spanning several

[†] The text in this chapter was originally published in the paper, Y. Chae and M. D. Allendorf, "The Effect of Ozone on the Growth Rate of Tin Oxide from Monobutyltintrichloride," Proc. EUROCVD-15, The Electrochemical Society Proceedings Series, 2005, Vol. 2005-09, p. 57.

mechanistic regimes for tin oxide growth, including mass-transport and kinetically controlled growth. The results indicate that ozone increases tin oxide deposition rates only when the growth is controlled by surface kinetics. Deposition rates decrease when ozone is added under mass-transport-controlled conditions. Using chemical kinetic modeling, we examined some potential chemical mechanisms for these effects.

8.2 Experimental Methods

The configuration of the SFR and the associated experimental details were published previously [7]. Briefly, the reactor consists of a stainless steel deposition chamber, a silicon carbide (SiC) heater, a reactant mixing chamber and showerhead, and a butterfly valve downstream of the deposition chamber that maintains the reactor pressure. The substrate (5.0 cm diameter and 1.6-mm-thick fused quartz) is placed on the SiC heater, and the distance between the substrate surface and showerhead is 3.8 cm.

MBTC and H_2O are delivered to the reactor by bubbling N_2 carrier gas (99.999% pure) through the liquid. MBTC with a purity of 99.83% was obtained from Atofina. The concentrations of MBTC and H_2O were varied over the range of 0.025–0.05 Torr and 0–0.1 Torr, respectively. The total pressure was varied from 25 to 200 Torr, and the total flow rate was varied using N_2 from 2.5 to 10 slpm. O_3 was generated by flowing O_2 into ozone generator (OREC V5-0, Ozone Research & Equipment Corp.). The concentration of O_3 could be varied from 0–0.126 Torr when a total pressure of 25 Torr was used and from 0–1.488 Torr for experiments at a total pressure of 200 Torr.

An FTIR (Nicolet Instruments) was used to monitor the relative concentrations of MBTC, H_2O, and O_3. The FTIR sampled the gases in the vacuum line downstream of the reactor, approximately 2 m from main chamber. Absolute concentrations of ozone were measured using ultraviolet absorbance. Ultraviolet light (253.7 nm) was generated by a mercury lamp and transmitted through a flow-through quartz cell (6 cm pathlength), then detected using a photodiode (DET210, Thorlabs Inc.) equipped with a narrow bandpass filter. The ozone concentration was calculated using Beer's Law and the ideal gas law:

$$conc.(\%-by-volume)=\frac{100\%}{\alpha_o}\frac{T_a}{293}\frac{760}{P}\frac{Abs}{L} \tag{8-4}$$

where α_o is the absorptivity in $atm^{-1}cm^{-1}$ of ozone at the wavelength of 253.7 nm, T_a is the absolute temperature of the gas being measured, P is the pressure in Torr of the gas, and L is the cell path length in cm. At 253.7 nm, the absorptivity of ozone in the gas phase (at 760 Torr, 20 °C) is 134 $atm^{-1}cm^{-1}$. A narrow bandpass filter was used to remove interference from neighboring ozone absorption lines.

8.3 Results of Deposition Experiments

The experiments performed here demonstrate that addition of O_3 can increase tin oxide growth rates, but only within a limited range of deposition conditions. The effects observed are displayed in Figures 8-1 through 8-3. As seen in Figure 8-1, SnO_2 growth rates from MBTC + O_2 increase substantially at a reactor pressure of 25 Torr when O_3 is added to the reactants. Addition of only 0.50 mol% O_3 (0.125 Torr) to a mixture containing 0.20 mol% MBTC more than triples the growth rate at 500°C. The activation energy for growth also decreases (Figure 8-3) from 11.9 kcal/mol in the absence of O_3 to 3.6 kcal/mol, suggesting that growth is approaching the mass-transport limit. In contrast, addition of much higher O_3 concentrations (1.49 Torr) at a reactor pressure of 200 Torr actually *decreases* the growth rate by a factor of 2.

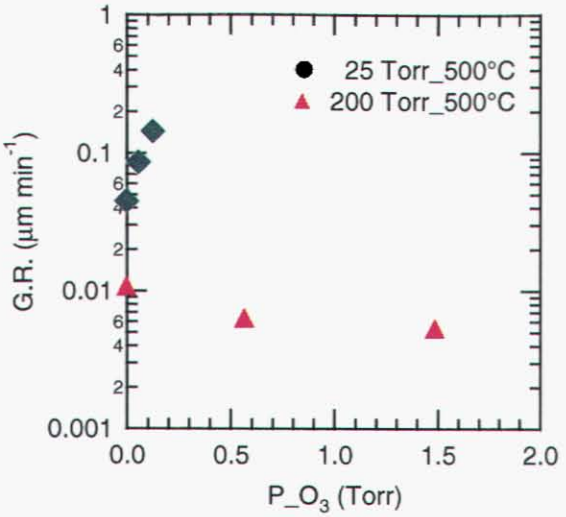

Figure 8-1. Tin oxide growth rates from MBTC + O_2 mixtures as a function of O_3 concentration. Inlet composition (mol%) at 25 Torr: MBTC/O_2 = 0.2/20; at 200 Torr: MBTC/O_2 = 0.0125/5.

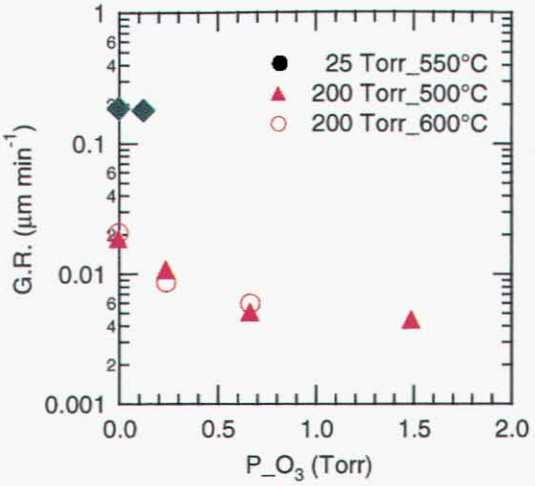

Figure 8-2. Tin oxide growth rates from MBTC + O_2 + H_2O mixtures as a function of O_3 concentration. Inlet composition (mol%) at 25 Torr: MBTC/O_2/H_2O = 0.2/20/0.4; at 200 Torr: MBTC/O_2/H_2O = 0.125/5/0.05.

Note that differing initial conditions for the experiments in Figures 8-1 and 8-2 prevent comparison of the absolute magnitudes of the growth rates.

When water vapor is added to the reactant mixture (Figure 8-2), O_3 addition again causes the growth rate to decrease. At 25 Torr, addition of 0.50 mol% O_3 causes a decrease of <4% in the growth rate (essentially unchanged within the uncertainties of the measurement), while at 200 Torr the effect is much greater: 0.33 mol% O_3 (0.67 Torr) decreases the growth rate by more than a factor of 3. The temperature dependence of the growth rate under these conditions (Figures 8-2 and 8-3) is essentially unaffected by O_3. With or without O_3, the activation energy is nearly zero, indicating that the reaction is at the mass transport limit.

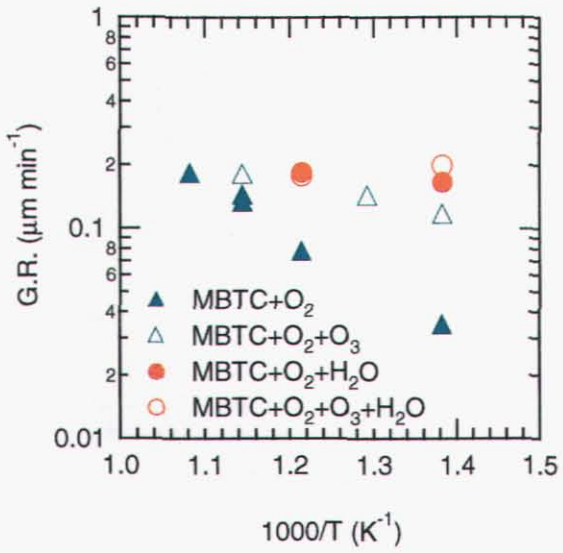

Figure 8-3. Arrhenius plot of the tin oxide growth rate showing the effect of O_3 addition at 25 Torr.

A key result apparent from Figure 8-3 is that O_3 addition does not lead to growth rates that exceed the fastest ones measured in the absence of O_3. In particular, the lower activation energy corresponding to O_3 addition to MBTC + O_2 causes the two ln(GR) vs $1/T$ curves to intersect at a deposition temperature ~675°C. This intersection is nearly the same as that between the (MBTC + O_2) and (MBTC + O_2 + H_2O) curves. Since tin oxide growth from MBTC + O_2 + H_2O is mass-transport limited under these conditions[7] the intersections suggest that the kinetics of the other two growth processes are also reaching the same mass transport limit at 675°C. Thus, even though the three systems probably involve different deposition chemistries, the transport rates are essentially the same, suggesting either a common precursor (presumably MBTC) or ones with similar diffusion constants. This has important implications for the mechanism, as will be seen below.

8.4 Kinetic Modeling and Discussion

In a previous report [7], we showed that tin oxide deposition from MBTC + O_2 mixtures exhibits growth regimes limited by both surface kinetics and mass transport. When MBTC and O_2 are the precursors, the kinetic regime spans a wide range of temperatures (300–650°C) at 25 Torr, but at pressures >100 Torr (the highest pressure at which we have the temperature dependence of the deposition rate) growth becomes limited by mass transport. Addition of H_2O accelerates the kinetics substantially, possibly due to the formation of an MBTC–H_2O complex in the gas phase, leading to mass-transport-limited growth at substrate temperatures above 400°C. Comparing these regimes with Figures 8-1 through 8-3, we see that O_3 increases the growth rate only under conditions in which growth is kinetically controlled, that is, from MBTC + O_2 mixtures at 25 Torr and without additional H_2O as a reactant (diamonds, Figure 8-1). Deposition under all other conditions examined here (including addition of H_2O and deposition at 200 Torr) is limited by mass transport. Under these circumstances, O_3 either does not affect the growth rate or decreases it.

These results suggest that one of the following two mechanisms is operative: (1) O_3 reacts with MBTC in the gas-phase to yield species that are more reactive with the surface than MBTC, or (2) it accelerates reactions already occurring on the surface or possibly opens new channels that lead to faster growth.

These possibilities can be tested by modeling the gas-phase chemistry. A complete discussion of this complex topic is outside the scope of this chapter. However, several key results, portions of which are described in a forthcoming paper describing kinetic modeling of tin oxide deposition from MBTC[8], are presented here.

First, we note that pyrolysis of MBTC does not occur under any of the deposition conditions adopted here because the residence times are too short. Thus, the pressure-dependent reaction [10] (heats of reaction below are from Ref. 13)

$$C_4H_9SnCl_3\ (+M) \leftrightarrow SnCl_3 + C_4H_9\ (+M) \qquad \Delta H°_R = 68.9\ \text{kcal/mol} \qquad (8\text{-}4)$$

is slow under these conditions, and MBTC reaches the surface intact (Figure 8-4a). Furthermore, this reaction cannot be the source in the growth-rate pressure dependence.

O_3 is thermally unstable, decomposing to form O_2 and reactive O atoms (R1) [11]. We modeled this decomposition reaction using the CHEMKIN SPIN code [12]. Rate constants for reactions between O, H, and OH and MBTC were assumed to be the same as for the reaction of these radicals with C_4H_{10}. As seen in Figure 8-4b, O_3 completely decomposes under deposition conditions, forming radicals that react with the C–H bonds in MBTC before it reaches the growth surface. The O atoms also form H and OH radicals (R2 and R3) through a series of other well-understood reactions, which can also attack MBTC in reactions analogous to R5 below. Heats of reaction obtained from thermodynamic data calculated by ab initio methods [13,14] suggest that once an H atom is abstracted from MBTC, the resulting organotin radical decomposes through two fast reactions to form stable products, as in R5–R7:

$$C_4H_9SnCl_3 + O \leftrightarrow CH_3CH_2CH_2CHSnCl_3 + OH \qquad \Delta H°_R = -2.7\ \text{kcal/mol} \qquad (8\text{-}5)$$

$$C_4H_8SnCl_3 \leftrightarrow (1\text{-}C_4H_8) + SnCl_3 \qquad \Delta H°_R = 1.3\ \text{kcal/mol} \qquad (8\text{-}6)$$

$$SnCl_3 \leftrightarrow SnCl_2 + Cl \qquad \Delta H°_R = 42.9\ \text{kcal/mol} \qquad (8\text{-}7)$$

Subsequent reaction between $SnCl_3$ and HCl (formed when Cl atoms attack MBTC) lead to $SnCl_4$ (Figure 8-4c), while $1\text{–}C_4H_8$ is partially oxidized to CO, CO_2, and H_2O (Figure 8-4d). The net effect of this chemistry is that essentially no MBTC reaches the surface (Figure 8-4a), a situation that prevails regardless of whether deposition is kinetically or mass-transport limited. Since previous experiments [7] and modeling [8,14] indicate that MBTC or an MBTC–H_2O complex reacts with the surface to form tin oxide, these results suggest that an alternative growth mechanism becomes active upon addition of O_3.

The growth data at 25 Torr are not sufficient to distinguish between the two possible mechanisms, but gas-phase species profiles predicted as a function of pressure suggest that both the formation of less reactive tin chlorides and the loss of gas-phase radicals near the surface play a role. As seen in Figure 8-5, the model predicts that O atom concentrations at the growth surface decrease with increasing pressure; the H and OH concentrations follow a similar trend. In contrast, the $SnCl_4$ and $SnCl_2$ concentrations increase. These results are consistent with a mechanism in which O, H, and/or OH radicals react on the surface with the tin precursor (which is something other than MBTC) to accelerate its oxidation, or act as an etching agent that removes inhibiting adsorbates such as hydrocarbons. As pressures increase, however, higher gas-phase radical recombination rates and increased formation of less reactive tin chlorides combine to cause the growth rate to decrease. When H_2O is also present in the reactant mixture, O, H, and OH may attack the MBTC–H_2O complex, causing a reduction in the precursor concentration and hence a decrease in the growth rate.

An important conclusion to be drawn from these results is that for H_2O to have an effect on growth rates, it must be mixed with the other reactants, not formed in the gas phase. Figure 8-4d shows that H_2O vapor is formed when MBTC reacts with O_2 in the gas phase and is present at the growth surface. Modeling indicates that its concentration increases with pressure. However, since the growth rate in the presence of O_3 *decreases* with pressure, H_2O formed at this point in the reactor either has no effect or reacts in some way to decrease the precursor concentration. Since H_2O in the reactant mixture is known to increase the growth rate even at atmospheric pressure [1], we conclude that it must react with MBTC in the gas phase prior to the high-temperature zone where water forms via reactions involving O atoms and other radicals (0–1.5 cm above the substrate). Ab initio calculations [14] and modeling [8] both support this concept, showing that such complexes can be thermodynamically stable and that a mechanism involving them is the most consistent with the complete set of experimental results (in particular the oxygen dependence).

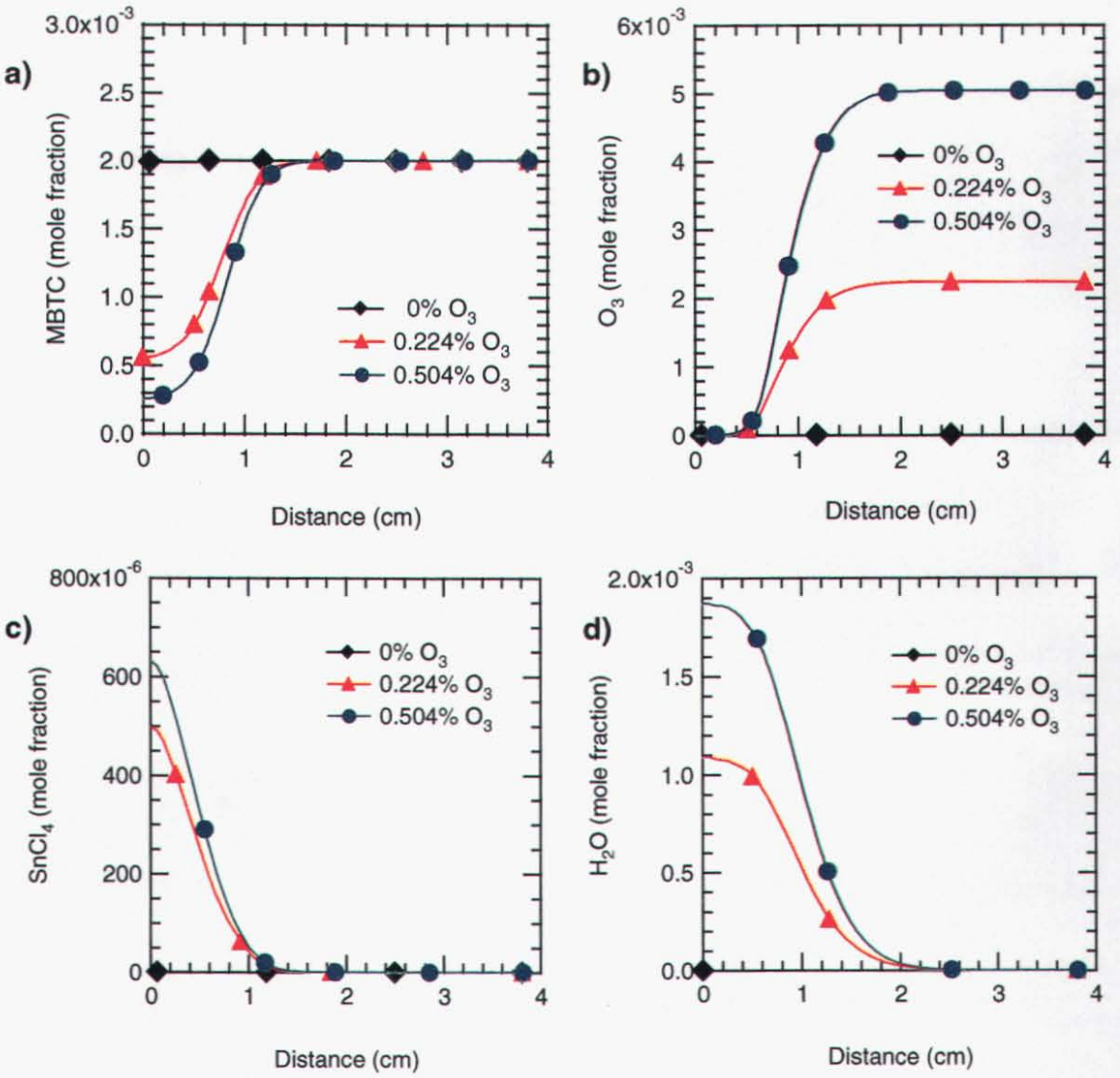

Figure 8-4. Simulated profiles of gas-phase species at 25 Torr. Initial conditions: 0.2% MBTC, 20% O_2, 0 or 0.504% O_3. 0 cm represents the substrate surface.

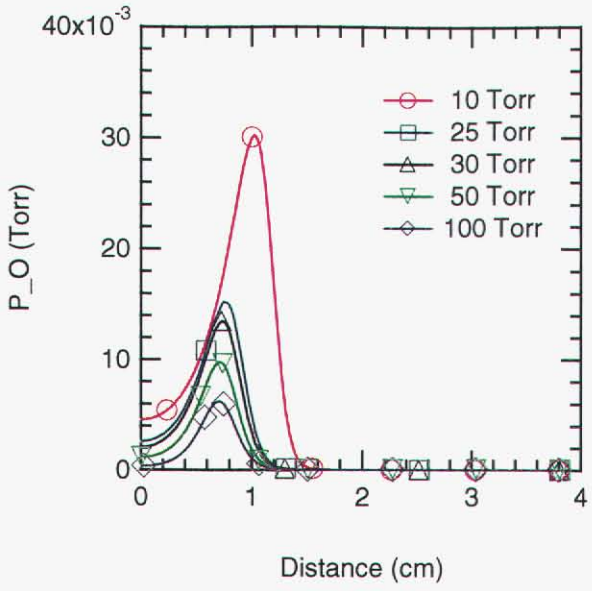

Figure 8-5. Simulated O atom profiles as a function of pressure. Initial conditions: 0.05 Torr MBTC + 5 Torr O_2 + 0.5 Torr O_3 at 500°C.

8.5 Conclusions

Addition of O_3 to MBTC + O_2 mixtures can increase tin oxide growth rates, but only under kinetically controlled conditions. The data and modeling presented here support a mechanism involving reaction of O, H, and OH radicals with the surface. Although the specifics of this interaction cannot be determined from the available data, two possibilities are that these radicals react with adsorbed MBTC or one its partially oxidized forms to accelerate its conversion to SnO_2. Alternatively, they may remove inhibiting adsorbates such as hydrocarbons that slow the deposition process. Higher pressures lead to mass-transport-limited growth. Under these conditions, O_3 addition actually decreases the growth rate.

From a practical point of view, these results suggest that successful additives for tin oxide growth from organometallic tin precursors cannot attack the tin precursor or rely on radicals formed in the gas phase to accelerate growth. Both of those routes become ineffective at higher pressures or under fast, mass-transport-controlled growth. Thus, precursors that are thermally stable but which can function as strong Lewis bases or oxidizers should be successful. A corollary is that radical-based chemistries that decompose halogenated organotin compounds lead to species (such as $SnCl_4$) that are less surface reactive than the intact precursor, in contrast with reactions such as O_3 with TEOS, in which O atom attack on the organometallic compound leads to very reactive organosilicon radicals.

Finally, it is important to note that new insight into the details of deposition chemistry can be obtained by perturbing the chemistry through the use of additives. This has not been a widely used approach in CVD mechanism studies. The results presented here suggest that it can be quite valuable, particularly when the gas-phase reactions are reasonably well characterized (e.g., O atom reactions with C–H bonds are well understood).

8.6 References

1. S.-M. Lee, D.-L. Kim, H.-J. Youn, K. S. Hong, *Jpn. J. Appl. Phys.* **39**, 407 (2000).
2. A. M. B. Van Mol, M. D. Allendorf, *16th Int. Symp. Chem. Vapor Dep./EUROCVD-14*; M. D. Allendorf, F. Maury, F. Teyssandier, Eds.; PV2003-08; p. 65, The Electrochemical Society Proceedings Series: Pennington (2003).
3. G. A. Neuman, P. R. Athey, R. L. Stewart-Davis, US Patent 5,599,387, 1997.
4. G. A. Neuman, J. F. Sopko, D. S. Dauson, US Patent 5,863,337, 1999.
5. O. Sanogo, M. R. Zachariah, *J. Electrochem. Soc.* **144**, 2919 (1997).
6. S. Romet, M. F. Couturier, T. K. Whidden, *J. Electrochem. Soc.* **148**, G82 (2001).
7. Y. Chae, W. G. Houf, A. H. McDaniel, M. D. Allendorf, *J. Electrochem. Soc.* **151**, C527 (2004).
8. Y. Chae, W. G. Houf, A. H. McDaniel, M. D. Allendorf, submitted to *J. Electrochem. Soc.*, 2005.
9. M. D. Allendorf, I. M. B. Nielsen, C. F. Melius, A. M. B. Van Mol, *16th Int. Symp. Chem. Vapor Dep./EUROCVD-14*; M. D. Allendorf, F. M., F. Teyssandier, Ed.; Vol. PV2003-8; pp 55, The Electrochemical Society Proceedings Series: Pennington (2003).
10. A. M. B. Van Mol, Y. Chae, A. H. McDaniel, M. D. Allendorf, accepted for publication in *Thin Sol. Films*, 2005.
11. J. M. Heimerl, T. P. Coffee, *Comb. Flame* **35**, 117 (1979).
12. R. J. Kee, F. M. Rupley, J. A. Miller, M. E. Coltrin, J. F. Grcar, E. Meeks, H. K. Moffat, A. E. Lutz, G. Dixon-Lewis, M. D. Smooke, J. Warnatz,; G. H. Evans, R. S. Larson, R. E. Mitchell, L. R Petzold, W. C. Reynolds, M. Caracotsios, W. E. Stewart, P. Glarborg, C. Wang, O. Adignun, *Chemkin Collection; Release 3.6 ed.*; Reaction Design, Inc.: San Diego, CA, 2000.
13. M. D. Allendorf, C. F. Melius, submitted to *J. Phys. Chem. A*, 2004.
14. M. D. Allendorf, A.M. B. Van Mol, *Topics Organomet. Chem.*, 2005, in press.

Distribution

1 ATTN: J. W. McCamy
Glass Technology Research Center
P. O. Box 11472
Pittsburgh, PA 15238

1 ATTN: J. F. Sopko
Glass Technology Research Center
P. O. Box 11472
Pittsburgh, PA 15238

1 ATTN: M. Li
Glass Technology Research Center
P. O. Box 11472
Pittsburgh, PA 15238

1 ATTN: Elliott P. Levine
Office of the Industrial Technology Program
EE-2F 1000 Independence Ave.
Washington, DC 20585

1 Michael Greenman
GMIC Executive Director
735 Ceramic Place, Suite 101
Westerville, OH 43081

1 MS9291 Mark Allendorf, 08324
1 MS9409 W. G. Houf, 08757
1 MS9052 A. H. McDaniel, 08367

2 MS9018 Central Technical Files, 8944

2 MS0899 Technical Library, 4536